AN INVESTIGATION OF POLAR LOWS

Thesis

Submitted by

CHARLES NEILL DUNCAN

for the degree of

DOCTOR OF PHILOSOPHY

University of Edinburgh
1975

I certify that this thesis and the research described herein is my own work.

Charles N. Duncan

ABSTRACT

A quasi-geostrophic, numerical model is used to investigate the most unstable modes of shallow, hydrodynamically unstable waves. The effects of horizontal wind shear and static stability variations with height are shown for idealised situations. Three polar low occasions are used to determine the characteristics of unstable waves under realistic conditions. Static stability is found to be very important, both in identifying the most unstable wavelength expected in a given situation, and in recognising the region in which polar low development is to be expected. It is suggested that polar air depressions are shallow baroclinic waves; that they develop in areas where a vertical wind shear exists; and that growing disturbances may be observed whether the wind speed increases or decreases with height.

CONTENTS

CHAPTER 1

INTRODUCTION

1.1 Some theories of polar low development

The acknowledged difficulty in forecasting the development of polar air depressions is related to their rarity compared with the occurrence of northerly cold air outbreaks. Evidently a southward moving polar or arctic airstream is not a sufficient condition for polar low development; other necessary conditions must be satisfied. Several credible theories have been proposed.

Harley (1960) described a polar low occasion associated with a "trowal", or trough of warm air aloft, which could be identified by frontal contour analysis. The influence of Iceland may often be a significant factor; Miller (1968), for example, suggested that this land mass may cause non-uniformity in the low level vorticity which would be modified by strong surface heating such that cyclonic vorticity would increase and anticyclonic vorticity decrease. Examples of Icelandic lee troughs are given in "Weather in Home Fleet Waters" (1964) which also describes polar lows as regions of enhanced instability where shower activity is increased. Using Doppler radar and isentropic analysis Harrold and Browning (1969) identified widespread precipitation associated with slantwise ascent of air as well as small scale convection. Stevenson (1968) and Lyall (1972) have described the weather encountered during the passage of polar lows and both commented on the widespread and intense precipitation observed on 7th December 1967 when a polar low passed across Ireland, Wales and southern

England.

It has been shown, Mansfield (1972), that shallow baroclinic waves have similar horizontal dimensions to polar lows, that is, wavelengths in the range 1200 Km to 600 Km. The identification of a low level baroclinic zone over Britain on 7th December 1967, by Harrold and Browning (1969), encourages the view that polar lows are shallow depressions which develop by transforming available potential energy into kinetic energy of the perturbation.

1.2 Purpose of this investigation

With the basic assumption that polar lows are hydrodynamically unstable waves the experiments in the following chapters are intended to investigate shallow baroclinic waves under conditions different from those used by Mansfield (1972). His solutions were obtained under similar conditions to those of Eady (1949); rigid lid upper and lower boundaries, linear vertical wind shear, no variation in Coriolis parameter with latitude and constant static stability. Throughout this investigation static stability is defined as

$$\sigma = \frac{1}{\theta} \frac{\partial \phi}{\partial p} \frac{\partial \theta}{\partial p},$$

where θ is potential temperature, ϕ is geopotential and p is pressure.

Changes in Coriolis parameter with latitude are neglected and rigid lid upper and lower boundaries are maintained in this study, although the upper boundary is raised to 300 mb since, for example, Harrold and Browning (1969) remark on

evidence of a perturbation at 9 Km on 7th December 1967. The constant static stability assumption is unrealistic since the vertically symmetric disturbance which is implied is not observed in the atmosphere because the lapse rate does not increase with height over an appreciable depth, particularly in cyclogenetic regions. In chapter 3 the effects of allowing static stability to vary in the vertical, the other conditions remaining unchanged, are investigated.

Both vertical and horizontal wind shears are important in the development of atmospheric disturbances since, under certain conditions, these shears lead to disturbances gaining kinetic energy from available potential energy or kinetic energy of the mean flow respectively. Brown (1968) has shown that when baroclinic and barotropic modes of instability exist together some wavelengths are unstable which are not unstable through either mode separately. The influence of various forms of horizontal shear on a baroclinic atmosphere are illustrated in chapter 4.

A necessary condition for polar low development is that energy must be available to enable the perturbation kinetic energy to increase with time. Whether this kinetic energy is obtained from the kinetic energy of the mean flow or from available potential energy is discussed in chapters 5 and 6 for three polar low occasions. The vertical and horizontal distributions of kinetic and potential energy, and regions of divergence and convergence of kinetic energy†, are also described.

† Where divergence (convergence) of kinetic energy is referred to in this thesis divergence (convergence) of kinetic energy flux is intended.

The observations of Harrold and Browning (1969) suggest that it is reasonable to treat polar lows as organised disturbances with horizontal dimensions of about 1000 Km. Mansfield (1972) has shown that under certain conditions baroclinic waves of this scale are unstable; since constant pressure surfaces and constant density surfaces are not parallel the perturbation gains kinetic energy at the expense of available potential energy. A more complex numerical model is necessary if other effects which cannot be represented in Mansfield's model are to be studied. The model employed here allows static stability to vary in the vertical and puts no restriction on variation of mean flow velocity across the flow.

The initial value technique which is used is particularly suited to the investigation of single developing waves since, after a suitable time, only the most unstable mode of the system exists in the model.

It will be shown that horizontal variations in static stability may be important. A model which takes this into account would also require to consider the part played by the divergent part of the wind, as this variable is also required for a consistent set of equations in which horizontal static stability variations are permitted. Such a model would also be able to investigate the effect of allowing velocity variations along the mean flow.

CHAPTER 2

THE NUMERICAL MODEL

2.1 Introduction

In the study of growing waves in the atmosphere various techniques have been used. Eady (1949) found analytical solutions for the simplified situation where the Coriolis parameter does not vary meridionally, vertical wind shear is linear and static stability is constant. A more general method used by Haltiner (1963) made no restriction on the vertical and horizontal variations of velocity and allowed static stability to vary with height. The method used in this study has been described by Brown (1969). It has the advantage of allowing higher vertical and horizontal resolution than Haltiner's model. The quasi-geostrophic vorticity equation and a diagnostic vertical velocity equation are used to investigate the growth in time of a disturbance, the characteristics of which are dictated by the mean flow and static stability fields and by the wavelength of the perturbation. The initial guess, unless it is an exact solution of the system of finite difference equations, will have a different wave speed at each grid point. Eventually the most unstable mode develops and the integration is terminated when the wave speeds at every grid point vary by less than some predetermined amount.

2.2 Scale Consideration

The quasi-geostrophic vorticity and thermodynamic equations are used, as these are appropriate at low Rossby

numbers (see for example, Phillips (1963)).

$$\frac{d(\zeta+f)}{dt} = \overline{f}\,\frac{\partial \omega}{\partial p} \qquad 2.1$$

$$\frac{d\theta}{dt} + \overline{\sigma}\omega = 0 \qquad 2.2$$

The bar denotes average values over constant pressure surfaces. The other symbols represent, f Coriolis parameter, θ potential temperature, ζ relative vorticity, σ static stability and ω vertical velocity in pressure co-ordinates. Mansfield (1972) has pointed out that in the study of polar lows the β-effect (northward variation of f) is small compared with the vorticity changes due to stretching. Scale analysis also shows that for disturbances with vertical and horizontal scales appropriate to polar lows the β-effect has the same order of magnitude as terms involving the advection of relative vorticity by the divergent part of the wind, a term which is neglected in the derivation of equation 2.1. The effect of meridional changes in Coriolis parameter will therefore be likewise neglected hereafter.

2.3 Derivation of the Model Equations

Neglect of the β-effect and definition of a stream-function $\psi=\phi/\overline{f}$, where ϕ is the geopotential, allows equations 2.1 and 2.2 to be rewritten as

$$\left(\frac{\partial}{\partial t} - \frac{\partial \psi}{\partial y}\frac{\partial}{\partial x} + \frac{\partial \psi}{\partial x}\frac{\partial}{\partial y}\right)\nabla^2\psi - \overline{f}\,\frac{\partial \omega}{\partial p} = 0 \qquad 2.3$$

$$\text{and} \quad \left(\frac{\partial}{\partial t} - \frac{\partial \psi}{\partial y}\frac{\partial}{\partial x} + \frac{\partial \psi}{\partial x}\frac{\partial}{\partial y}\right)\frac{\partial \psi}{\partial p} + \frac{\overline{\sigma}}{\overline{f}}\omega = 0, \qquad 2.4$$

where the Laplacian is a two-dimensional operator acting over surfaces of constant pressure. The x and y directions are taken as along the flow and across the flow respectively. The streamfunction and vertical velocity may then be written in terms of a mean value and a deviation from that value, i.e.

$$\psi(x,y,p,t) = \overline{\psi}(y,p) + \psi'(x,y,p,t)$$
$$\text{and} \quad \omega(x,y,p,t) = \overline{\omega}(y,p) + \omega'(x,y,p,t). \qquad 2.5$$

Substituting the representation of 2.5 into equations 2.3 and 2.4 and neglecting second order terms, we have

$$\left(\frac{\partial}{\partial t} + U\frac{\partial}{\partial x}\right)\nabla^2\psi' - \frac{\partial^2 U}{\partial y^2}\frac{\partial \psi'}{\partial x} - \overline{f}\frac{\partial \omega'}{\partial p} = 0 \qquad 2.6$$

$$\text{and} \quad \left(\frac{\partial}{\partial t} + U\frac{\partial}{\partial x}\right)\frac{\partial \psi'}{\partial p} - \frac{\partial U}{\partial p}\frac{\partial \psi'}{\partial x} + \frac{\overline{\sigma}}{\overline{f}}\omega' = 0, \qquad 2.7$$

where $U = -\frac{\partial \overline{\psi}}{\partial y}$. Applying the Laplacian operator to 2.7, then differentiating 2.6 w.r.t. pressure and eliminating time derivatives gives

$$\overline{f}\frac{\partial^2 \omega'}{\partial p^2} + \frac{\overline{\sigma}}{\overline{f}}\nabla^2\omega' = \frac{\partial}{\partial p}\left((U\nabla^2 - \frac{\partial^2 U}{\partial y^2})\frac{\partial \psi'}{\partial x}\right) - \nabla^2\left(U\frac{\partial^2 \psi'}{\partial x \partial p} - \frac{\partial U}{\partial p}\frac{\partial \psi'}{\partial x}\right). \qquad 2.8$$

As equations 2.6 and 2.8 are linear, general solutions may be written

$$\psi' = \psi_a \sin kx + \psi_b \cos kx \qquad 2.9$$

and $\omega' = \omega_a \sin kx + \omega_b \cos kx$

where ψ_a, ψ_b, ω_a and ω_b vary with y, p and t only. Substitution of 2.9 into equations 2.6 and 2.8 leads to

$$\left.\begin{aligned}
\nabla^2\frac{\partial\psi}{\partial t}a &= kU\nabla^2\psi_b - k\frac{\partial^2 U}{\partial y^2}\psi_b + \bar{f}\frac{\partial\omega}{\partial p}a \\
\nabla^2\frac{\partial\psi}{\partial t}b &= -kU\nabla^2\psi_a + k\frac{\partial^2 U}{\partial y^2}\psi_a + \bar{f}\frac{\partial\omega}{\partial p}b \\
\bar{f}\frac{\partial^2\omega}{\partial p^2}b + \frac{\bar{\sigma}}{\bar{f}}\nabla^2\omega_b &= k\frac{\partial}{\partial p}\left(U\nabla^2\psi_a - \frac{\partial^2 U}{\partial y^2}\psi_a\right) - k\nabla^2\left(U\frac{\partial\psi}{\partial p}a - \frac{\partial U}{\partial p}\psi_a\right) \\
\bar{f}\frac{\partial^2\omega}{\partial p^2}a + \frac{\bar{\sigma}}{\bar{f}}\nabla^2\omega_a &= -k\frac{\partial}{\partial p}\left(U\nabla^2\psi_b - \frac{\partial^2 U}{\partial y^2}\psi_b\right) + k\nabla^2\left(U\frac{\partial\psi}{\partial p}b - \frac{\partial U}{\partial p}\psi_b\right).
\end{aligned}\right\} \qquad 2.10$$

Together with the boundary conditions

$$\psi_a = \psi_b = 0 \text{ at } y = 0 \text{ and } W,$$

where W is the channel width,

and $\omega_a = \omega_b = 0$ at p = 1000 mb and 300 mb,

these equations form the set on which the model is based.

The condition that the vertical velocity is zero at 300 mb reduces computer time although it also precludes stratospheric representation. In the present study the saving in computer time is thought to outweigh this disadvantage.

An analysis of energy transformations in unstable disturbances is also possible with this model by a method which has been described in detail by Brown (1968). For completeness the energy transformation terms which are used in subsequent

chapters are listed in an appendix.

2.4 Numerical Solution of the Model Equations†

A two dimensional y-p grid is used with streamfunction and vertical velocity stored at alternate vertical levels as shown in figure 2.1.

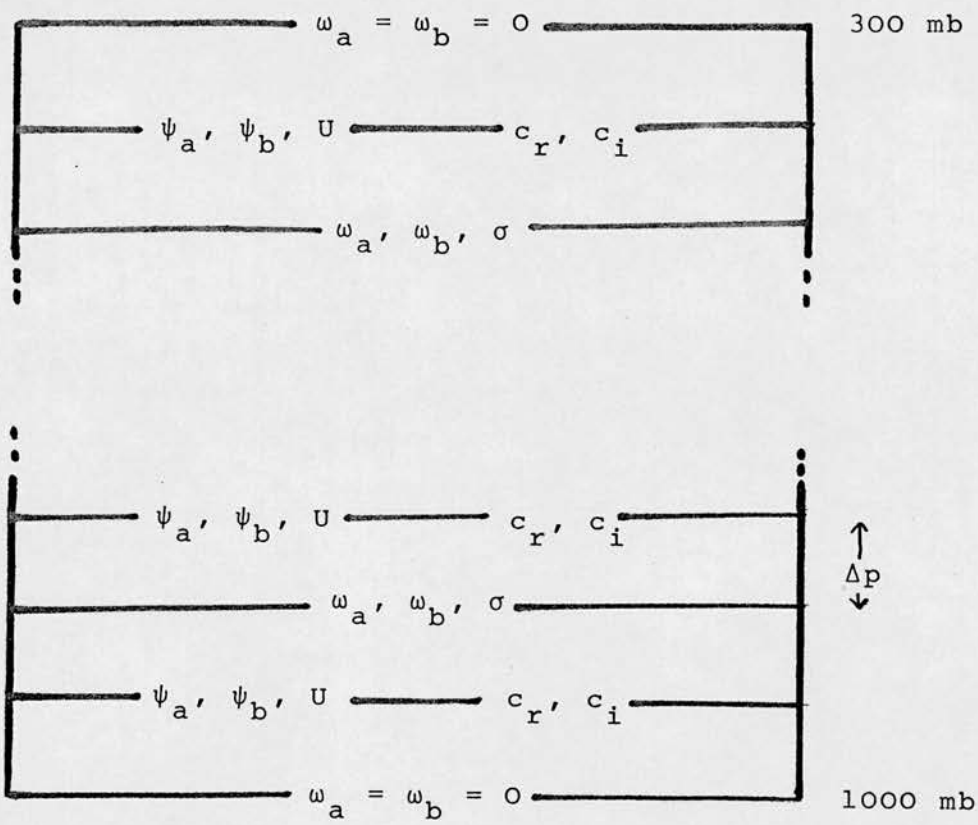

Figure 2.1: Vertical structure of the two dimensional grid

Since the Laplacian operator in equations 2.10 can be written

$$\nabla^2 \equiv \left(\frac{\partial^2}{\partial y^2} - k^2 \right)$$

the first two equations of the set are one-dimensional and were solved using the Thomas algorithm (see for example Ames (1969)).

† An experiment to investigate the accuracy of the numerical model is described in the second appendix (pp 92a and b).

The diagnostic equations for the vertical velocity are two-dimensional and were solved using the successive over-relaxation technique. Before integration began the model required specification of the mean velocity and static stability fields, the Coriolis parameter and the perturbation wavelength. An initial guess is supplied for the perturbation streamfunction; throughout this study the initial guess employed was

$$\psi_a = 10^{-4} \sin (\pi y/w), \quad \psi_b = 9 \times 10^{-5} \sin (\pi y/w).$$

To remove the two-grid length waves which sometimes appeared after the initial forward time step, a linear time-smoother was applied for the first ten leapfrog time steps. As the integration continued, the wave speeds at each grid point, which were initially different from one grid point to the next, all converged towards the wave speed of the most unstable mode of the system. When all the wave speeds varied by less than a given tolerance (0.05 ms^{-1} was used), the model was stopped.

Real and imaginary wave speeds were calculated by considering the general solution

$$\psi' = A \cos k (x - \delta)$$

which, with equation 2.9, leads to

$$\psi_a = A \sin k\delta, \qquad 2.11$$

and $$\psi_b = A \cos k\delta; \qquad 2.12$$

therefore

$$A^2 = \psi_a^2 + \psi_b^2$$

Differentiating 2.11 and 2.12 w.r.t. time yields

$$\frac{\partial \psi}{\partial t}a = \frac{\partial A}{\partial t} \sin k\delta + Ak \frac{\partial \delta}{\partial t} \cos k\delta$$

and $$\frac{\partial \psi}{\partial t}b = \frac{\partial A}{\partial t} \cos k\delta - Ak \frac{\partial \delta}{\partial t} \sin k\delta.$$

Hence

$$C_r = \frac{\partial \delta}{\partial t} = (kA^2)^{-1} \left(\psi_b \frac{\partial \psi}{\partial t}a - \psi_a \frac{\partial \psi}{\partial t}b \right),$$

and similarly

$$C_i = (kA^2)^{-1} \left(\psi_a \frac{\partial \psi}{\partial t}a + \psi_b \frac{\partial \psi}{\partial t}b \right).$$

The time integration scheme is numerically stable if $U_{max} \Delta t \leq k^{-1}$ where U_{max} is the largest mean flow velocity. The time step used varied from case to case such that

$$\Delta t = (k (U_{max} + 5))^{-1}.$$

CHAPTER 3

THE EFFECT OF VERTICAL VARIATIONS IN STATIC STABILITY

3.1 Choice of Static Stability

When air flows southwards from polar regions over the relatively warm water of the North Atlantic Ocean near Iceland, the air nearest to the surface is heated and a layer develops in which the lapse rate is close to the dry adiabatic lapse rate. In this chapter three cases are studied which represent different depths of relatively unstable layer. Table 3.1 shows the values of static stability (σ) for each case and Figure 3.1 illustrates the corresponding temperature structures if a temperature of $-54^{\circ}C$ is assumed at 250 mb.

Table 3.1 Static Stabilities for cases I, II and III

Pressure (mb)	Static Stability (m^2 mb^{-2} s^{-2})		
	Case I	Case II	Case III
300	0.200	0.140	0.1200
400	0.100	0.080	0.0430
500	0.030	0.040	0.0380
600	0.010	0.012	0.0180
700	0.005	0.007	0.0085
800	0.003	0.004	0.0055
900	0.002	0.003	0.0030
1000	0.001	0.002	0.0030

These static stabilities were used with a linear vertical wind shear of 0.05 m s^{-1} mb^{-1} and a Coriolis parameter of

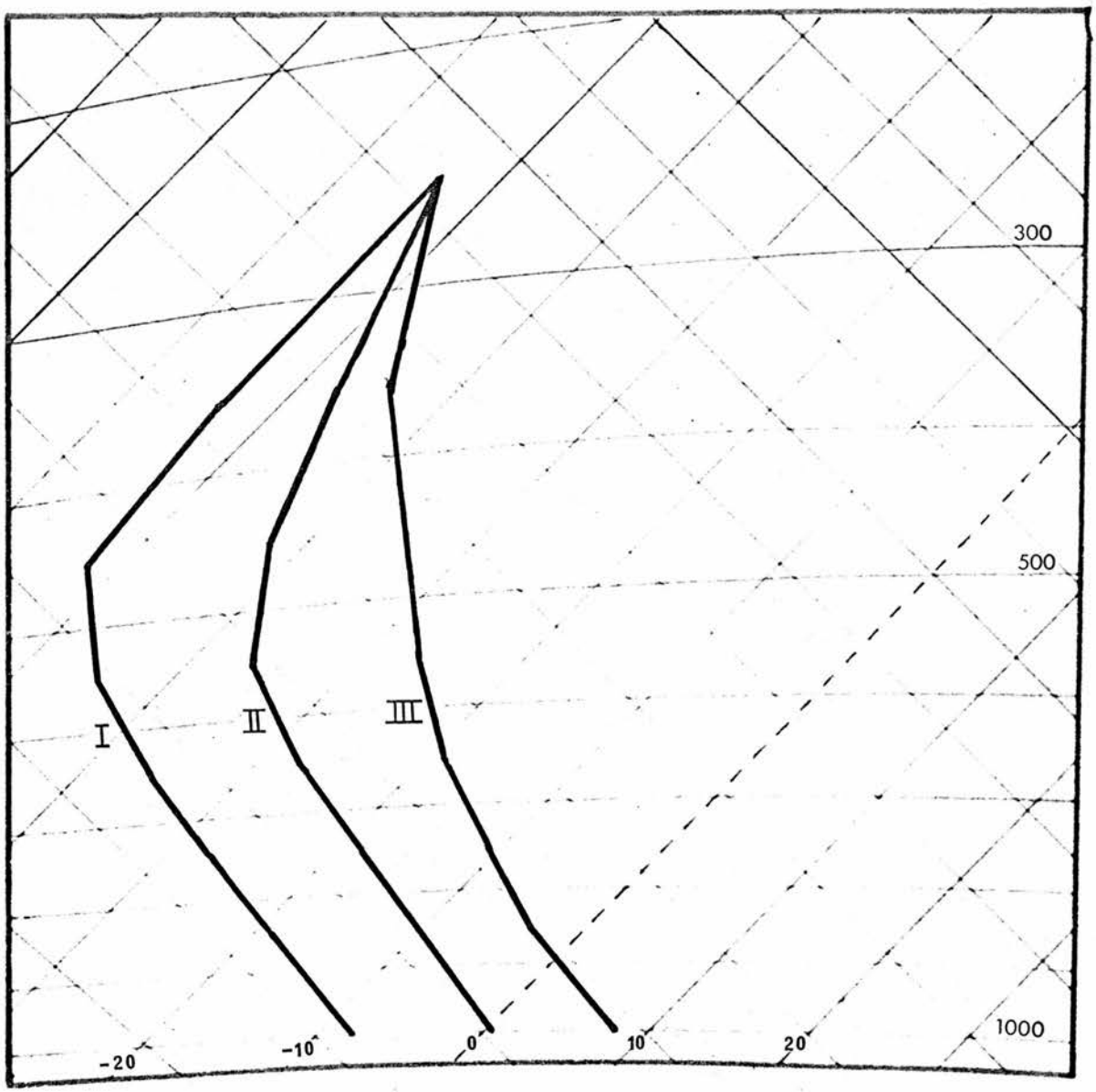

Figure 3.1 Temperature soundings corresponding to static stabilities in table 3.1. (At 250 mb a temperature of $-54^{o}C$ is assumed in each case).

1.26×10^{-4} s^{-1} in a low resolution model. The grid spacings used were Δy = 320 Km and Δp = 50 mb while the channel width was 1600 Km.

3.2 Results

In each case the most unstable wavelength is close to the observed wavelengths of polar lows. In figures 3.2, 3.3 and 3.4 are shown the growth rate and real and imaginary wave speeds as a function of wavelength for cases I, II and III respectively. At short wavelengths the model does not converge and the dashed part of the growth rate curve is obtained from the corresponding extrapolation of the imaginary wave speed curve. The phase speed is seen to decrease with decreasing wavelength since shallower disturbances exist at shorter wavelengths and this implies a lowering of the steering level.

The growth rate of 2.6 day^{-1} obtained for the 725 Km wave using the static stabilities of case I is larger than would normally be encountered in the baroclinic westerlies; this does not lack realism since rapid development of polar lows is common and is one of the features which makes them difficult to forecast. Since the low level static stabilities are larger in case II the growth rates are correspondingly smaller and the wavelength of maximum instability is larger, namely 800 Km. In figure 3.4 the upper growth rate curve shows that the wavelength of maximum instability is 1000 Km; the lower curve, which corresponds to solutions obtained with the vertical wind shear halved, has approximately the same most unstable wave-

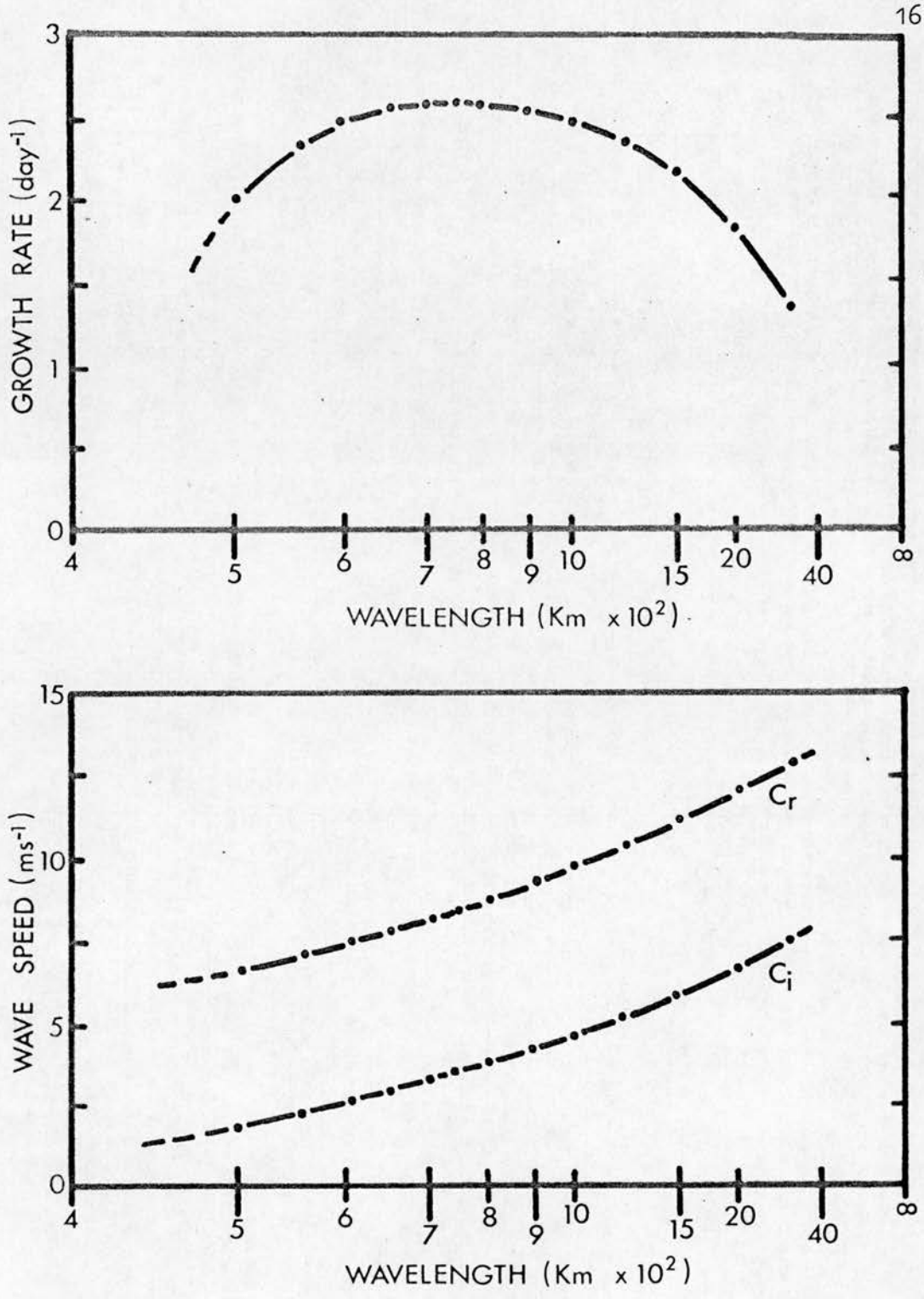

Figure 3.2 Above: Growth rate for case I.

Below: Real and imaginary wave speeds for case I.

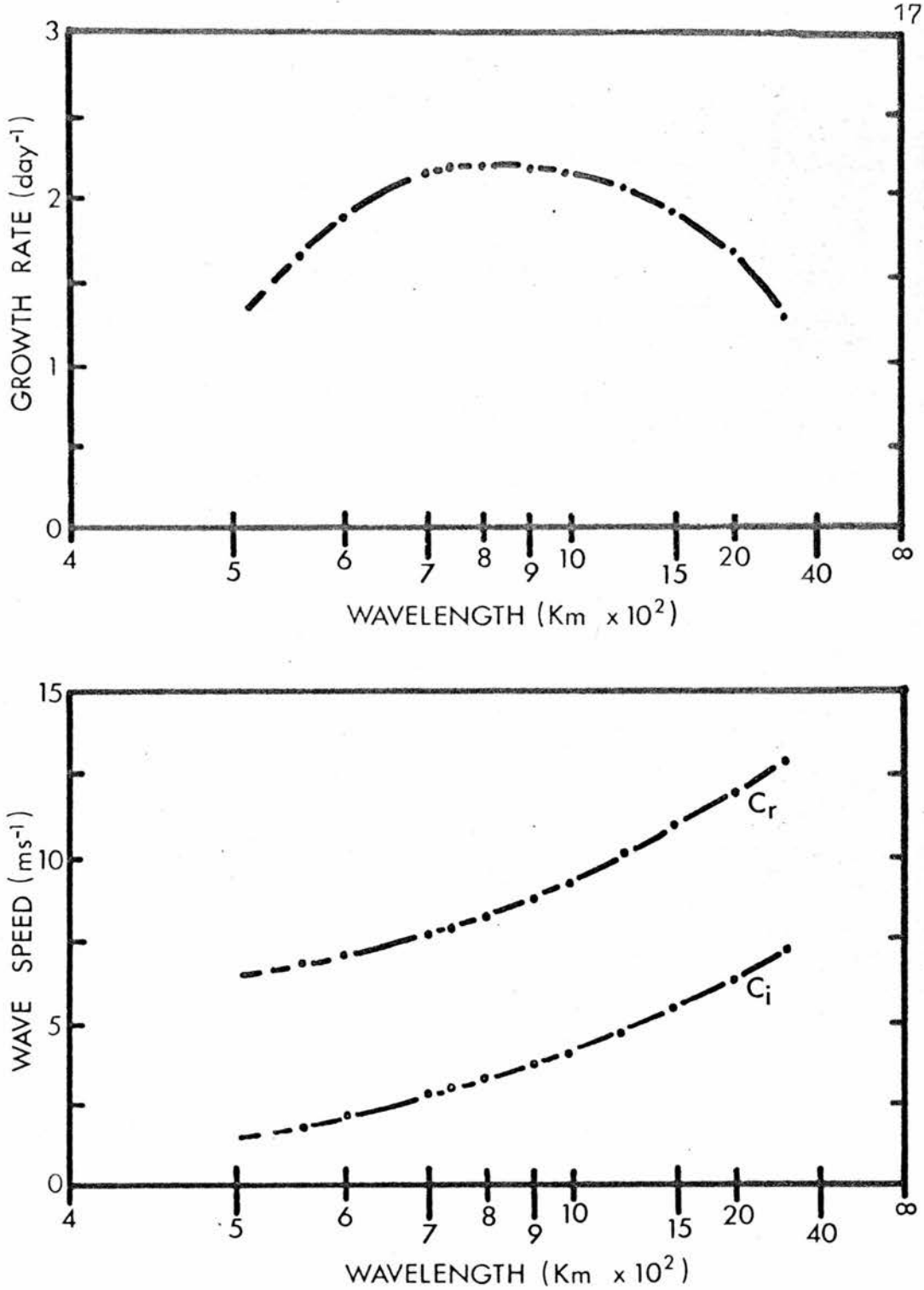

Figure 3.3 Above: Growth rate for case II.

Below: Real and imaginary wave speeds for case II.

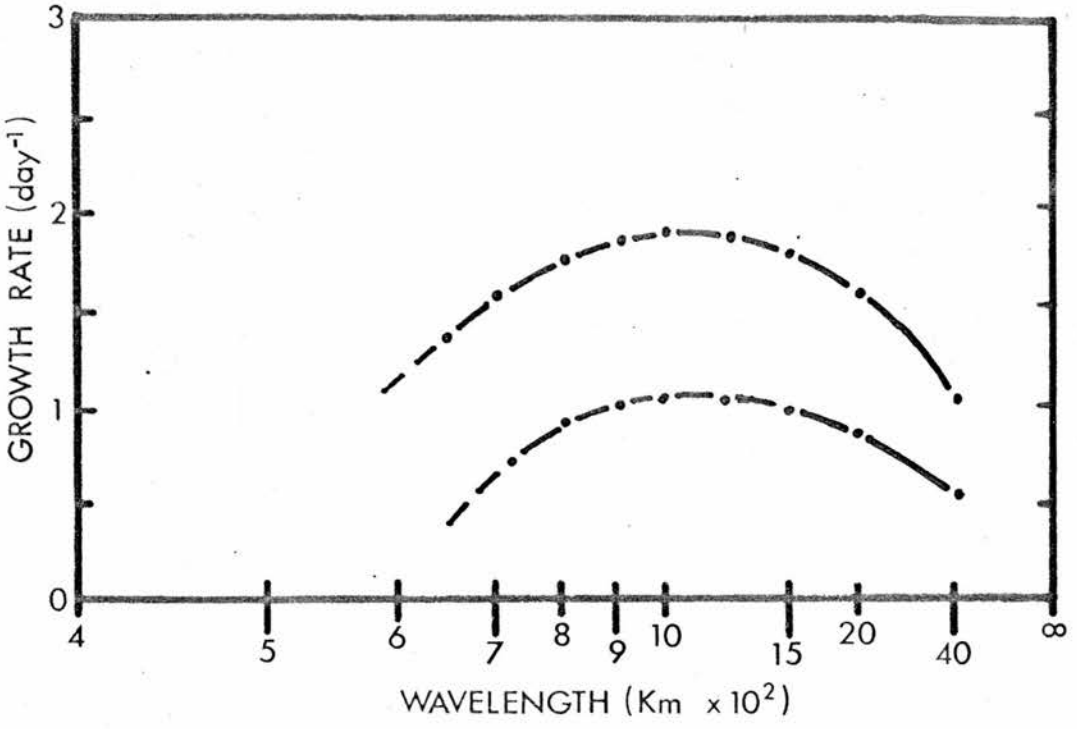

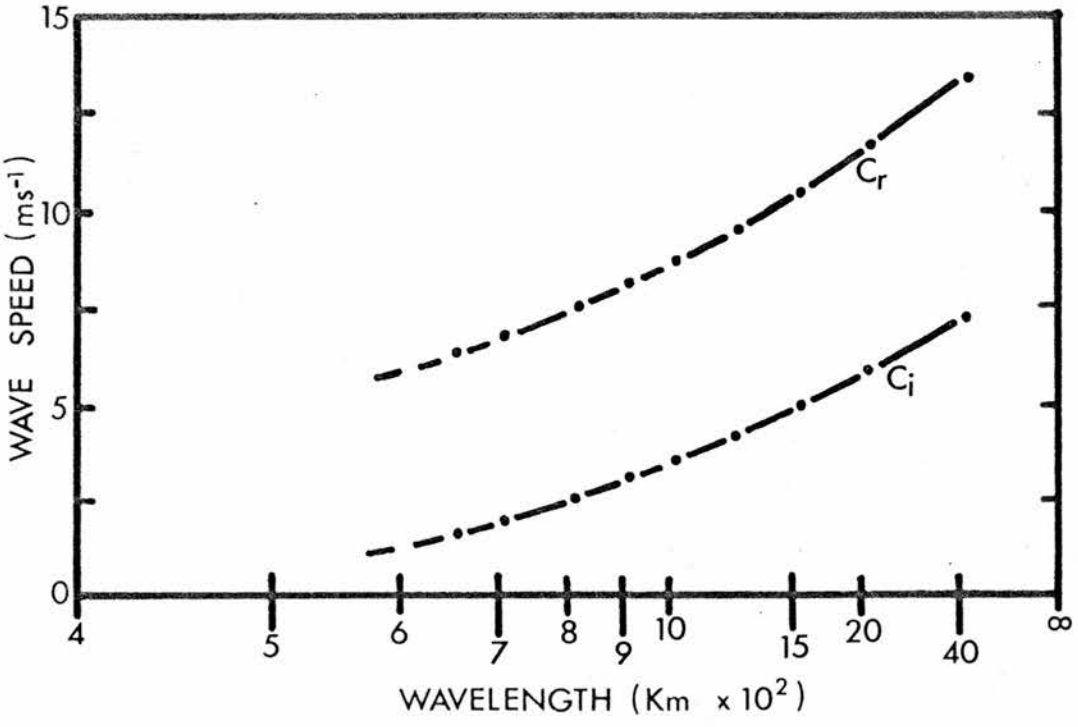

Figure 3.4 Above: Growth rate for case III; lower curve corresponds to solutions obtained using half of the vertical wind shear used in the upper curve.

Below: Real and imaginary wave speeds for case III corresponding to the upper growth rate curve above.

length but only half the growth rate of the upper example. The phase speeds of the most unstable wave in all three cases are similar, being 8.5, 8.0 and 9.3 ms^{-1}. These are close to observed polar low phase speeds.

The vertical structures of the three most unstable waves are very similar. The streamfunction amplitudes shown in figure 3.5 are normalised so that the largest value in each case is the same. At low levels the amplitude of the waves is large, but above about 500 mb it becomes very small. Also shown is the streamfunction phase lag for the 1000 Km wave in case III. Below 700 mb, the backward tilt of the trough is pronounced, but above that level only a small tilt is observed. This implies that above 700 mb the trough and the thermal perturbation wave are almost in phase.

Conversion of eddy available potential energy to eddy kinetic energy occurs mostly below 700 mb. This is illustrated in figure 3.6 along with other energy conversion rates, which are calculated as described in the appendix, for the 1000 Km wave of case III. The conversion of eddy available potential energy to eddy kinetic energy and the vertical divergence of kinetic energy are shown as positive where they tend to increase K_e and negative where they reduce the growth of K_e. Conversion of zonal to eddy available potential energy is also shown. Arbitrary energy units are used and the energy conversion rates are given in arbitrary energy units per day. Although the perturbation kinetic energy source is restricted to the lowest 350 mb the vertical divergence transfers kinetic energy

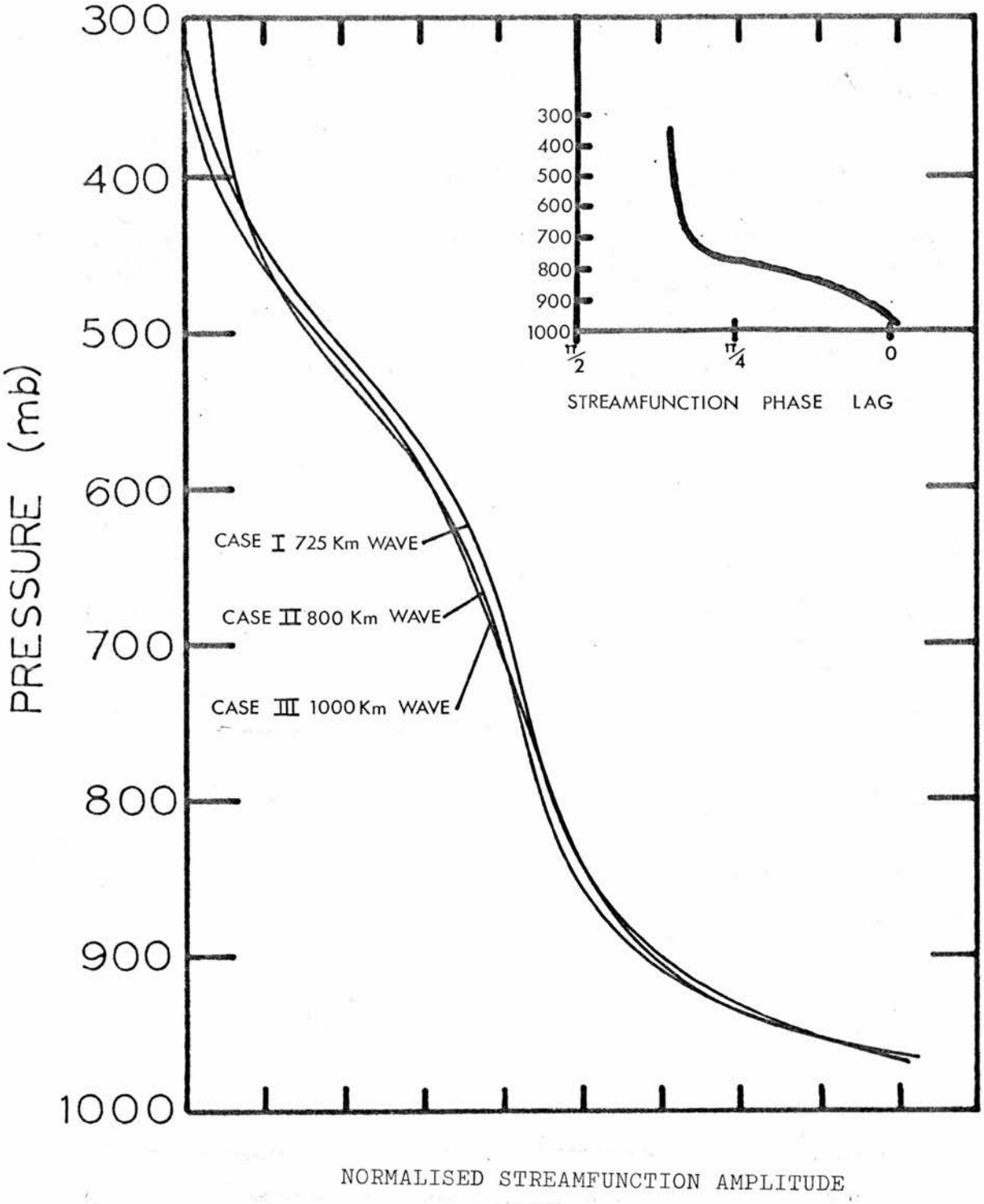

Figure 3.5 Relative streamfunction amplitude for the most unstable wavelengths of cases I, II and III. Also shown is the relative streamfunction phase lag for the 1000 Km wave of case III.

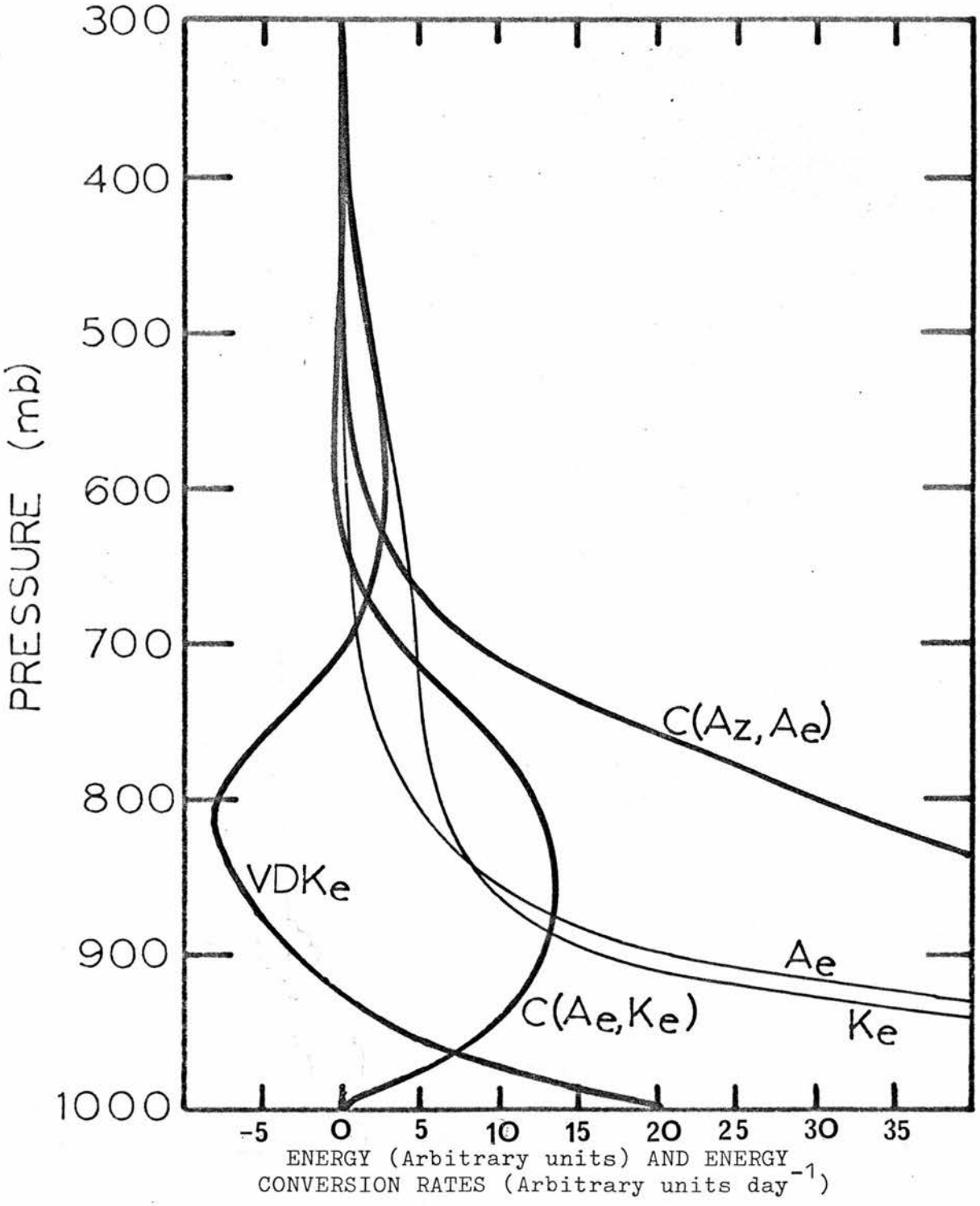

Figure 3.6 Horizontally averaged energy (arbitrary units) and energy conversion rates (arbitrary energy units day^{-1}) for the 1000 Km wave of case III.

to higher levels and also tends to increase the eddy kinetic energy at the very lowest levels. Owing to the low vertical resolution, values of the vertical divergence of kinetic energy cannot be calculated close to 1000 mb, but apparently there is convergence of kinetic energy near the surface, since the eddy kinetic energy is larger near the surface than at the level where $C(A_e, K_e)$ is largest.

CHAPTER 4

THE EFFECT OF HORIZONTAL WIND SHEAR ON SHALLOW DISTURBANCES

4.1 Types of Shear Investigated

The superposition of a horizontal wind shear on a baroclinic fluid may or may not enhance the growth of a disturbance in that fluid. In this chapter three types of horizontal shear are investigated; firstly, a symmetrical jet with amplitude increasing linearly with height; secondly, a shear with maximum wind speed at one side of the channel and minimum wind speed at the other side, with a point in the centre of the channel where $\frac{\partial^2 U}{\partial y^2}=0$; and finally a linear horizontal shear independent of height.

The symmetrical case uses a wind profile described by

$$U = U(p) + B\left(\frac{1000 - p}{700}\right)\left(1 - \cos(2\pi y/W)\right),$$

which defines the jet amplitude, B, and where p is the pressure in millibars. The term U(p) in every example in this chapter represents a linear vertical wind shear of 0.05 $ms^{-1}mb^{-1}$. The profile in the second case is given by

$$U = U(p) + B\left(\frac{1000 - p}{700}\right)\left(\tanh(1.5 - 3y/W)\right).$$

The superimposed linear shear, both cyclonic and anticyclonic, was such that the mean value of U(p) at each level was unchanged.

In the first two cases the fields of mean velocity were slightly altered by an iterative technique to maintain the

zonal available potential energy at the same value as in case III of the last chapter. Such an adjustment is not necessary in the linear shear case since the required condition exists. The effect of the adjustment is shown in figure 4.1 where the vertical shear across a 100 mb layer is shown for the cosine and tanh cases. By ensuring that the zonal available potential energy in the three cases of this chapter is the same as in case III of the last chapter a direct comparison of these is possible since, in each case, the unstable waves are primarily baroclinic in nature. Throughout this chapter the model parameters are the same as in the last chapter and the static stability is the same as in case III.

4.2 The Cosine Case

Figure 4.2 shows the growth rate as a function of wavelength for the symmetrical jet with B = 40 ms^{-1} and 20 ms^{-1}, as well as the real and imaginary wave speeds for the situation where B = 40 ms^{-1}. The wavelength of maximum instability is 1000 Km, as it was in the purely baroclinic case discussed in chapter 3; the growth rate increases as the jet amplitude increases; finally, at long wavelengths the real wave speed begins to decrease. This last was not observed in the purely baroclinic example since the β-effect, which tends to stabilise the long waves, was then neglected. In the cosine case the long waves are predominantly barotropic so that the phase speed decreases with increasing wavelength.

Although barotropic instability exists in this symmetric case, the increased growth rate, of the 1000 Km wave, is not

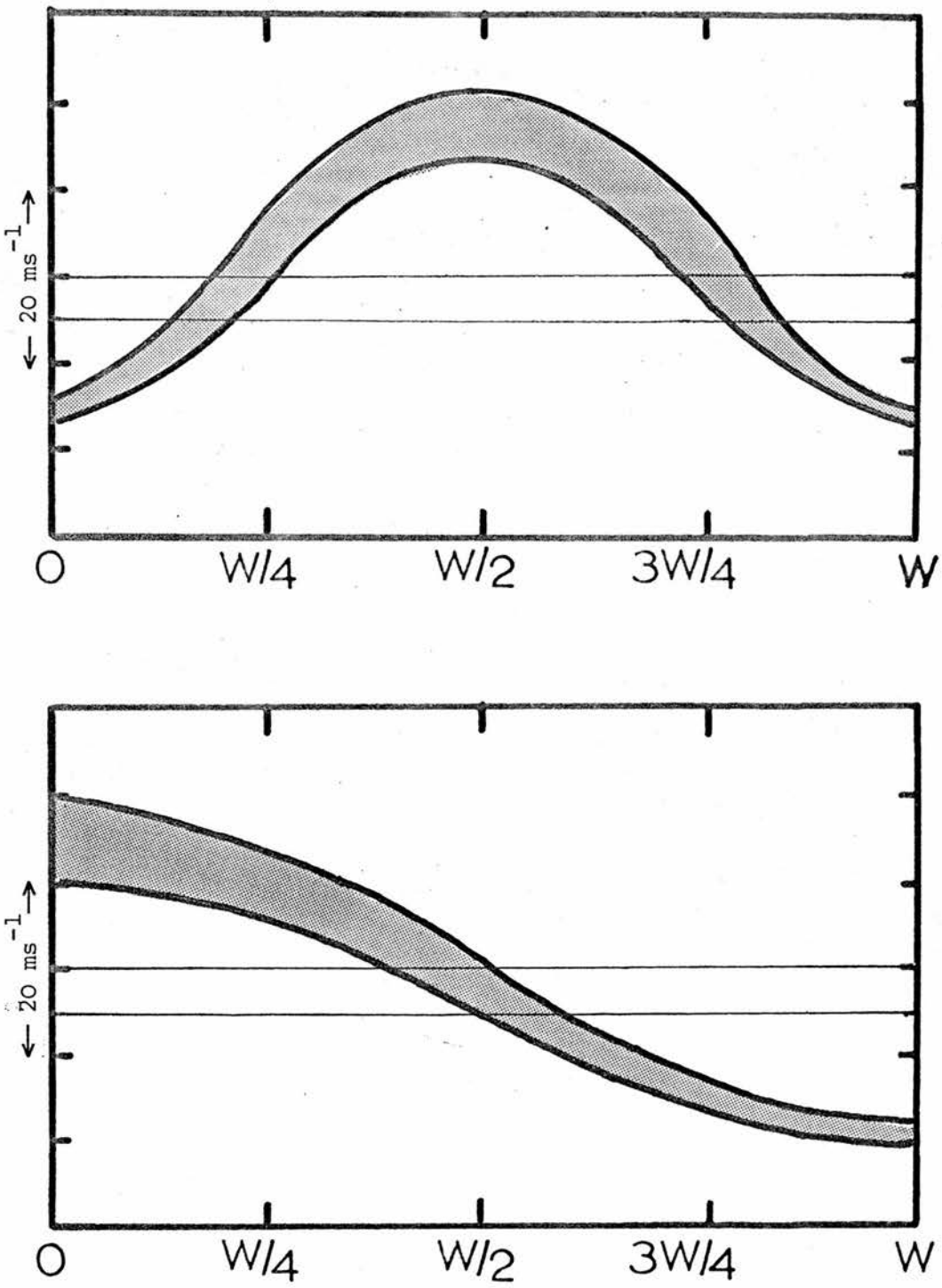

Figure 4.1 Wind shear for cosine case (above) and tanh case (below) corresponding to the 100 mb layer from 450 mb to 350 mb. Also shown is the corresponding 'pure' baroclinic shear.

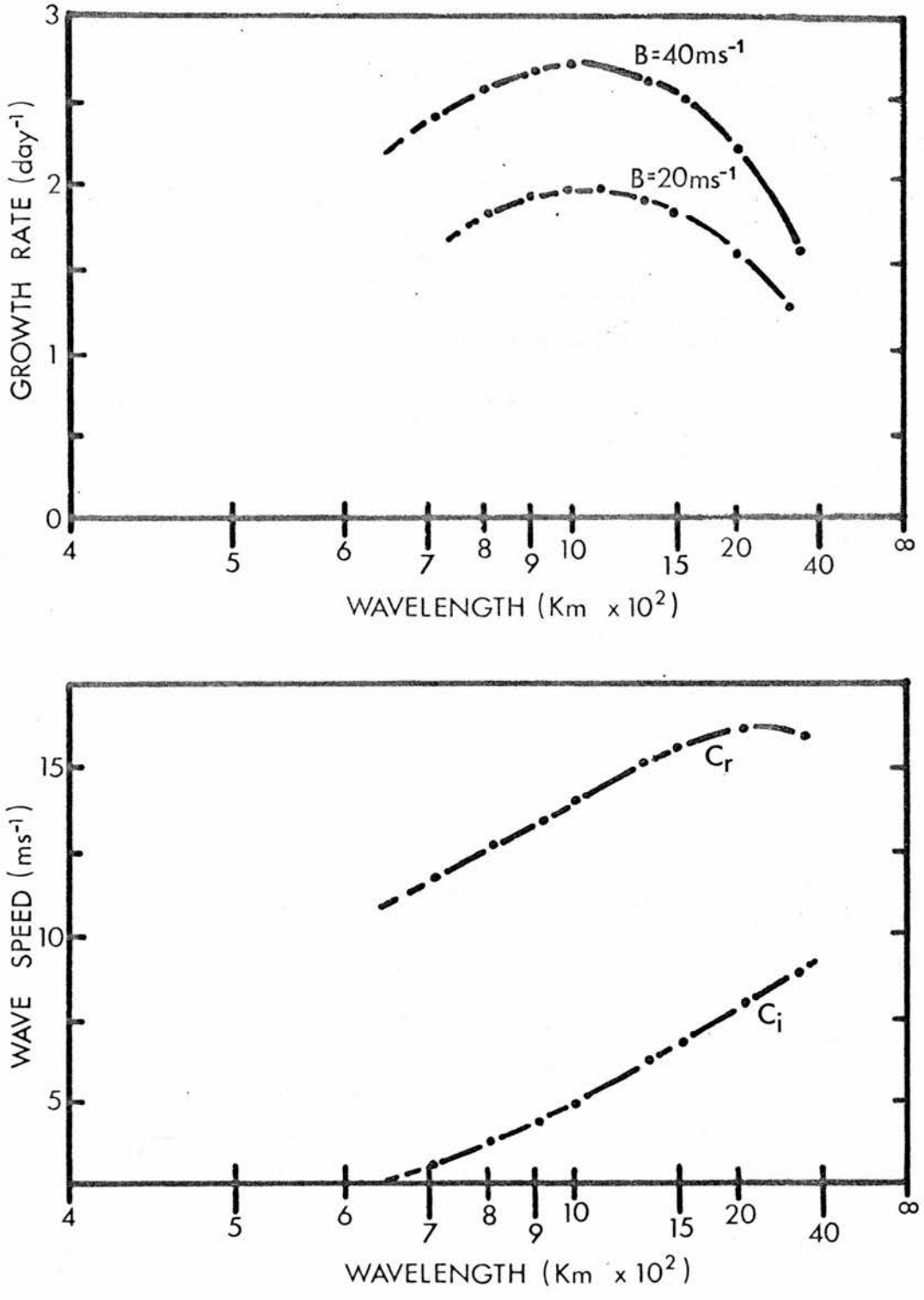

Figure 4.2 Above: Growth rate for cosine case for $B=40ms^{-1}$ and for $B=20ms^{-1}$.

Below: Real and imaginary wave speeds for cosine case for $B=40ms^{-1}$.

due to a gain in eddy kinetic energy from zonal kinetic energy, since this mode of energy conversion is at least two orders of magnitude smaller than the baroclinic mode at every point in the model. The existence of the jet allows a local increase in vertical wind shear below the jet maximum, thus leading to increased eddy available potential energy. The horizontally integrated energy conversion rates shown in figure 4.3 emphasise the similarity between this case and the purely baroclinic example. Significant differences are apparent, however, when the horizontal structure of the wave is considered. Eddy kinetic energy is concentrated near the centre of the channel when a jet is present; at $y = W/4$ and $3W/4$ it is an order of magnitude smaller than at the maximum. The backward tilt of the trough with height is similar to the purely baroclinic case but, additionally, a small backward tilt is observed towards the channel sides. This tilt is largest at 850 mb where a phase lag of $\pi/10$ occurs between the sides and the centre of the wave. The jet therefore increases the growth rate by increasing the vertical wind shear near the centre of the channel, but reduces the significant width of the disturbance by reducing the local vertical wind shear near the channel sides.

4.3 The Tanh Case

The effect of horizontal wind shear in the tanh case is similar to that observed in the last section; the unstable baroclinic waves develop in the region of maximum vertical wind shear and are damped elsewhere. The most unstable wave

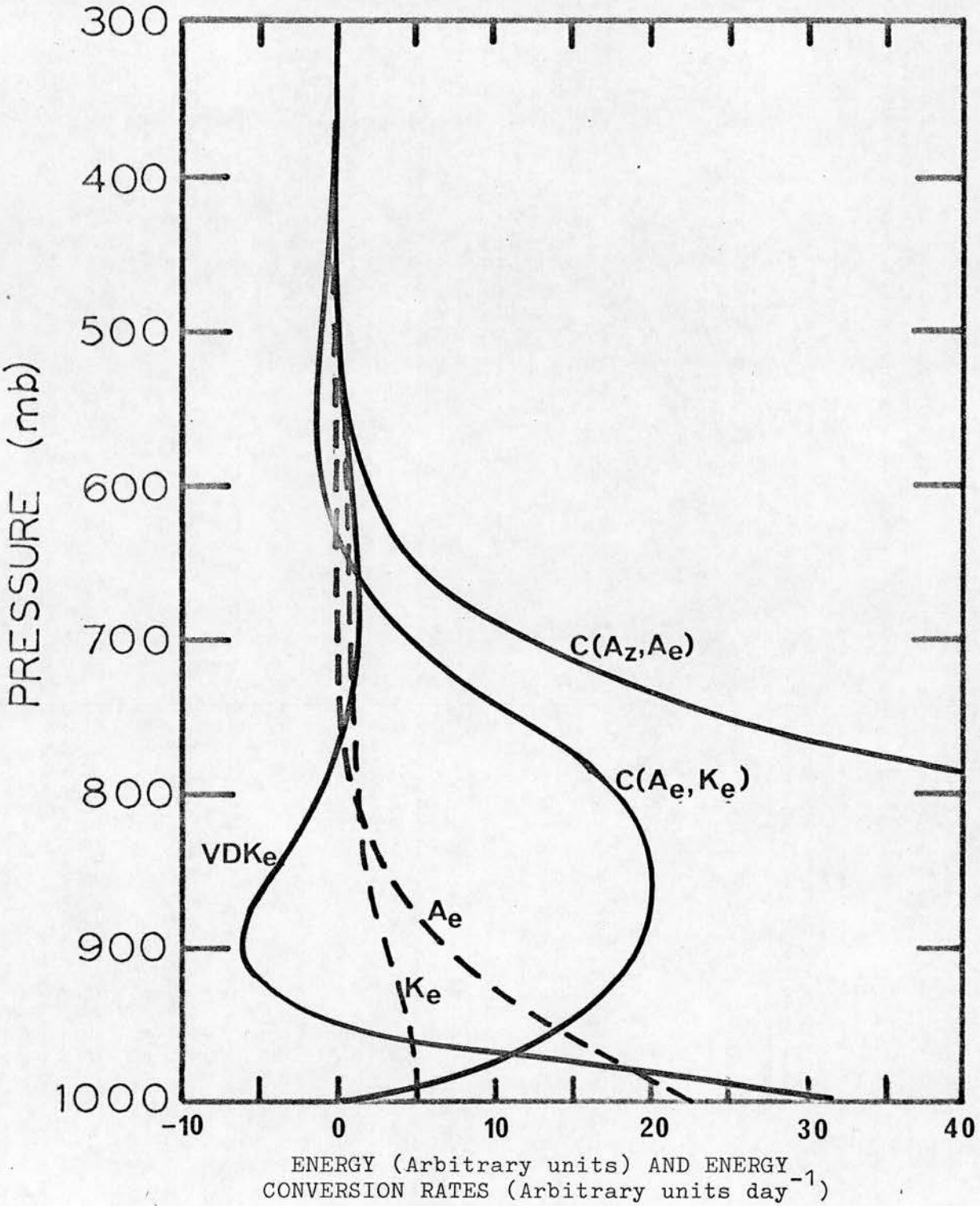

Figure 4.3 Horizontally averaged energy and energy conversion rates for the 1000 Km wave, cosine wind profile.

again has a wavelength of 1000 Km and the eddy kinetic energy is almost entirely derived from available potential energy. As there are only small differences between horizontally integrated energy conversion rates in this case and the last these are not illustrated. Streamfunction amplitudes and phase lags are shown in figure 4.4 for the purely baroclinic, cosine-jet and tanh-jet cases for the 950 mb level of the 1000 Km wave. This illustrates that regions of maximum vertical wind shear are preferred for development. Although a backward tilt in the horizontal is observed where horizontal shear exists it is noted that the perturbation amplitude decreases rapidly where this tilt occurs. Figure 4.5 shows the real and imaginary wave speeds as a function of wavelength for the tanh case where B = 40 ms^{-1} and also the growth rate curves for B = 40 ms^{-1}, B = 20 ms^{-1} and an expanded channel case, with B = 40 ms^{-1}. The expanded channel was used to investigate the inhibiting effect of the channel walls on waves developing close to the walls, as in the tanh cases. At the side of the channel where the vertical wind shear was largest two extra grid points were introduced with mean flow velocities identical to those at the previous channel wall. It can be seen that the wave developing in the expanded channel grows more rapidly than the others. However, this is not entirely due to the relaxed boundary conditions since this case also has a larger mean flow available potential energy than the less rapidly developing wave, in the narrower channel.

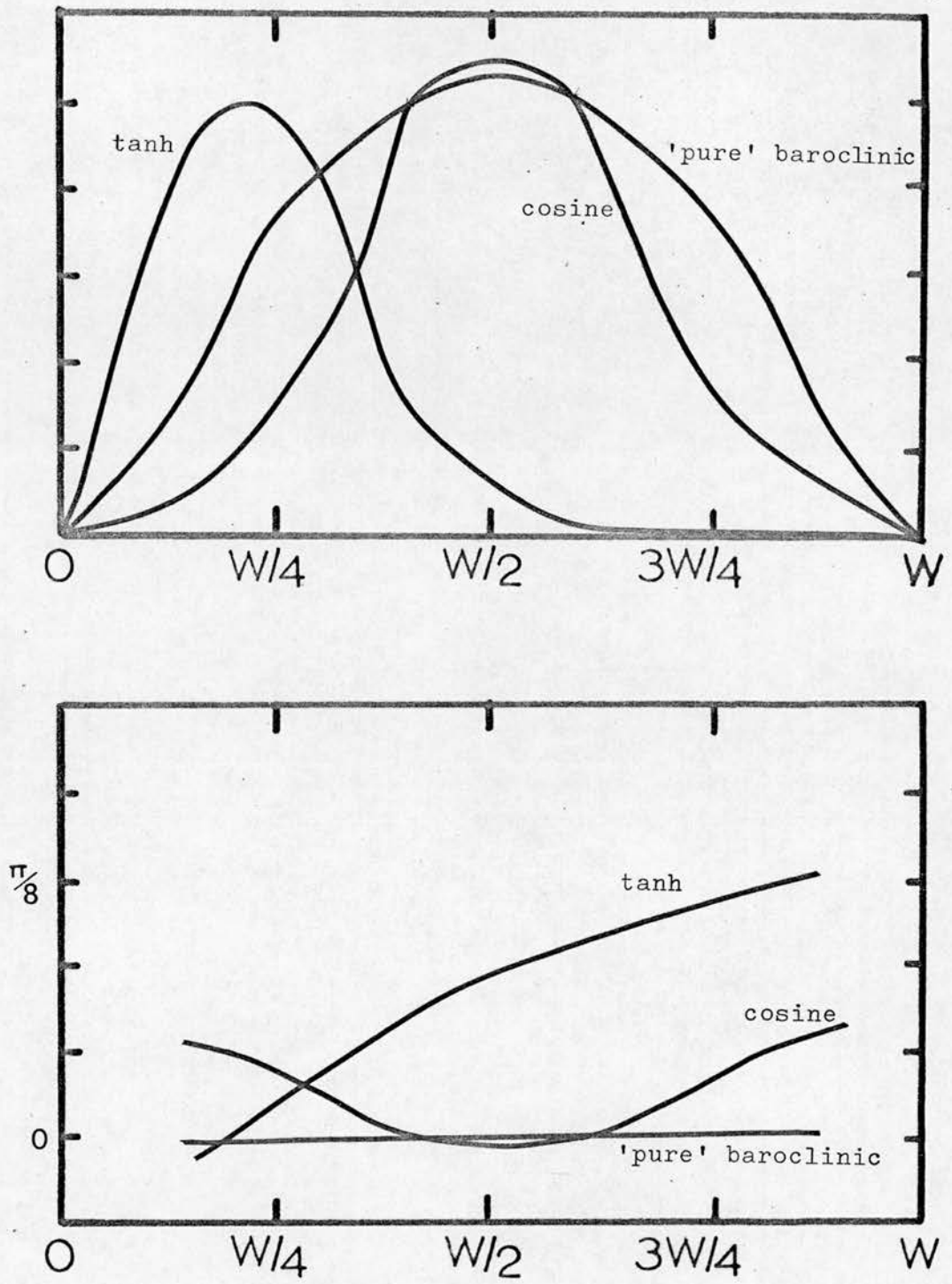

Figure 4.4 Above: Relative streamfunction amplitude at 950 mb for tanh, cosine and 'pure' baroclinic cases.

Below: Relative streamfunction phase lag at 950 mb for tanh, cosine and 'pure' baroclinic cases.

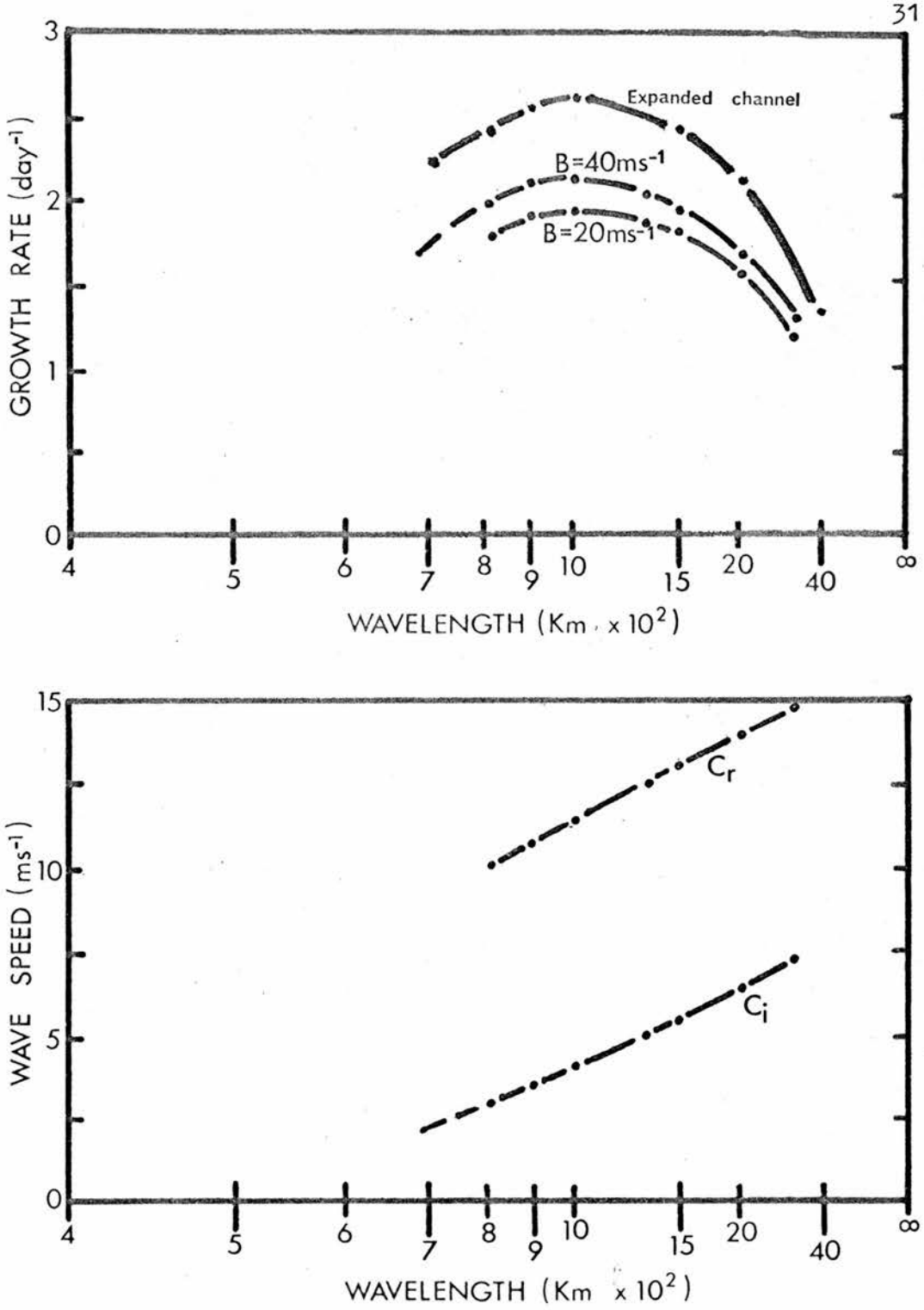

Figure 4.5 Above: Growth rate for tanh case for $B=40ms^{-1}$, $B=20ms^{-1}$ and for an expanded channel with $B=40ms^{-1}$.

Below: Real and imaginary wave speeds for tanh case for $B=40ms^{-1}$.

4.4 The Linear Case

When a linear horizontal shear is imposed on a frictionless, baroclinic fluid the unstable disturbances are damped. Haltiner (1971) has shown, for a simple situation, that for both cyclonic and anticyclonic shears the damping is the same. The horizontal shear causes horizontal tilting of the trough and of the maximum vertical velocity by different amounts, so that the area where ascent correlates well with warm air, and descent with cold air, is greatly reduced.

Table 4.1 shows the real and imaginary wave speeds and growth rates obtained with the numerical model for various horizontal shears. It can be seen that the damping is independent of the sense of the shear. Since the disturbances develop on the faster moving side of the flow the phase speeds are correspondingly larger than when no horizontal shear exists.

If friction is considered the problem becomes more complicated. The tendency for friction to reduce relative vorticity is proportional to the surface relative vorticity. It is usual, however, for vortex stretching to increase near the surface when friction is present, a factor which reduces the damping effect. In the experiments described above, the vorticity of the mean flow did not exceed 6.25×10^{-6} s^{-1}; the frictional effect would be correspondingly smaller and less important than the horizontal tilting effect.

4.5 Properties of the Model

After the experiments of the last two chapters, the

Table 4.1 Wave speeds and growth rates for cyclonic and anticyclonic linear shears superimposed on a baroclinic flow (Stability, wind shear and model parameters as in case III).

	No Shear			Anticyclonic 3.125×10^{-3} ms^{-1}Km^{-1}			Cyclonic 3.125×10^{-3} ms^{-1}Km^{-1}			Cyclonic 6.25×10^{-3} ms^{-1}Km^{-1}		
Wavelength	C_r	C_i	kc_i	C_r	C_i	kc_i	C_r	C_i	kc_i	C_r	C_i	kc_i
(Km)	ms^{-1}	ms^{-1}	day^{-1}	ms^{-1}	ms^{-1}	day^{-1}	ms^{-1}	ms^{-1}	day^{-1}	ms^{-1}	ms^{-1}	day^{-1}
4000	13.2	7.1	0.97	13.4	6.9	0.94	13.4	6.9	0.94	14.2	6.4	0.87
2000	11.5	5.6	1.52	11.9	5.3	1.45	11.9	5.3	1.45	13.0	4.9	1.34
1500	10.4	4.7	1.72	10.9	4.4	1.61	10.9	4.4	1.61	12.2	4.2	1.51
1000	8.6	3.4	1.87	9.4	3.1	1.71	9.4	3.1	1.71	10.9	3.0	1.66
900	8.1	3.0	1.84	9.0	2.8	1.68	9.0	2.8	1.68	10.5	2.6	1.62
800	7.5	2.6	1.76	8.4	2.3	1.57	8.4	2.3	1.57	NO CONVERGENCE		

Table 4.2 Summary of Results of Chapters 3 and 4

Stability	Shear	Most Unstable Wavelength (Km)	C_r (ms^{-1})	C_i (ms^{-1})	Growth Rate (day^{-1})
I	Baroclinic ($0.05ms^{-1}mb^{-1}$)	725	8.5	3.5	2.61
II	Baroclinic ($0.05ms^{-1}mb^{-1}$)	800	9.2	3.9	2.14
III	Baroclinic ($0.05ms^{-1}mb^{-1}$)	1000	8.6	3.4	1.87
III	Baroclinic ($0.025ms^{-1}mb^{-1}$)	1000	6.8	1.7	0.95
III	Cosine ($B=20ms^{-1}$)	1000	11.5	4.2	2.30
III	Cosine ($B=40ms^{-1}$)	1000	14.1	5.0	2.71
III	Tanh ($B=20ms^{-1}$)	1000	9.9	3.6	1.96
III	Tanh ($B=40ms^{-1}$)	1000	11.4	3.9	2.15
III	Linear ($3.125x10^{-3}ms^{-1}Km^{-1}$)	1000	9.4	3.1	1.71
III	Linear ($6.25x10^{-3}ms^{-1}Km^{-1}$)	1000	10.9	3.0	1.66

results of which are summarised in table 4.2, the convergence of the model was assessed. Using information from 79 model runs it was found that although wave speeds vary considerably from grid point to grid point at the beginning of a run it would be possible to obtain solutions using a larger tolerance than $\varepsilon = 0.05$ ms^{-1} if the required accuracy is known beforehand. With the assumption that the solution obtained with $\varepsilon = 0.05$ ms^{-1} is accurate to $\pm$ 0.025 ms^{-1}, table 4.3 shows the tolerance required in the 79 runs to ensure that all solutions are known to the accuracy shown.

Table 4.3 Worst error obtained as a function of tolerance

Tolerance ms^{-1}	Worst error encountered	
	C_r ms^{-1}	C_i ms^{-1}
2.0	$\pm$ 1.00	$\pm$ 1.08
1.5	$\pm$ 0.77	$\pm$ 0.74
1.0	$\pm$ 0.50	$\pm$ 0.54
0.5	$\pm$ 0.28	$\pm$ 0.27
0.1	$\pm$ 0.08	$\pm$ 0.08

Although in many cases the computer time involved is small this is not always so when asymmetrical velocity fields are used; several examples were encountered where the use of $\varepsilon = 0.3$ ms^{-1} would have resulted in a halving of computer time.

CHAPTER 5

THE CASE STUDIES

5.1 Origin and Treatment of Data

Three cases of polar low development have been investigated using the model described earlier. In each, data were obtained from the National Oceanographic and Atmospheric Administration, Northern Hemisphere Data Tabulations and the U.K. Daily Aerological Report. Upper air soundings were noted for the stations shown in figure 5.1 at 00Z on 5th April 1968, 7th December 1967 and 2nd January 1965. At the stations shown by lower case letters geopotential heights at standard pressure levels from 1000 mb to 300 mb were recorded while at the stations indicated by capital letters the temperature soundings were used to determine heights at every 50 mb between 1000 mb and 250 mb.

5.2 The Objective Analysis

Dixon et al. (1972) have described the method of objective analysis, using orthogonal polynomials, which was employed in this study. Using trivariate polynomials of the form

$$P(x,y,p) = a_0 + a_1x + a_2y + a_3p + a_4x^2 + a_5xy + a_6xp + a_7y^2 + a_8yp + a_9p^2 + a_{10}x^3 + a_{11}x^2y + a_{12}x^2p + a_{13}xy^2 + a_{14}xyp + a_{15}xp^2 + a_{16}y^3 + \ldots\ldots$$

each observed height can be represented by an equation

$$h(x,y,p) = P(x,y,p).$$

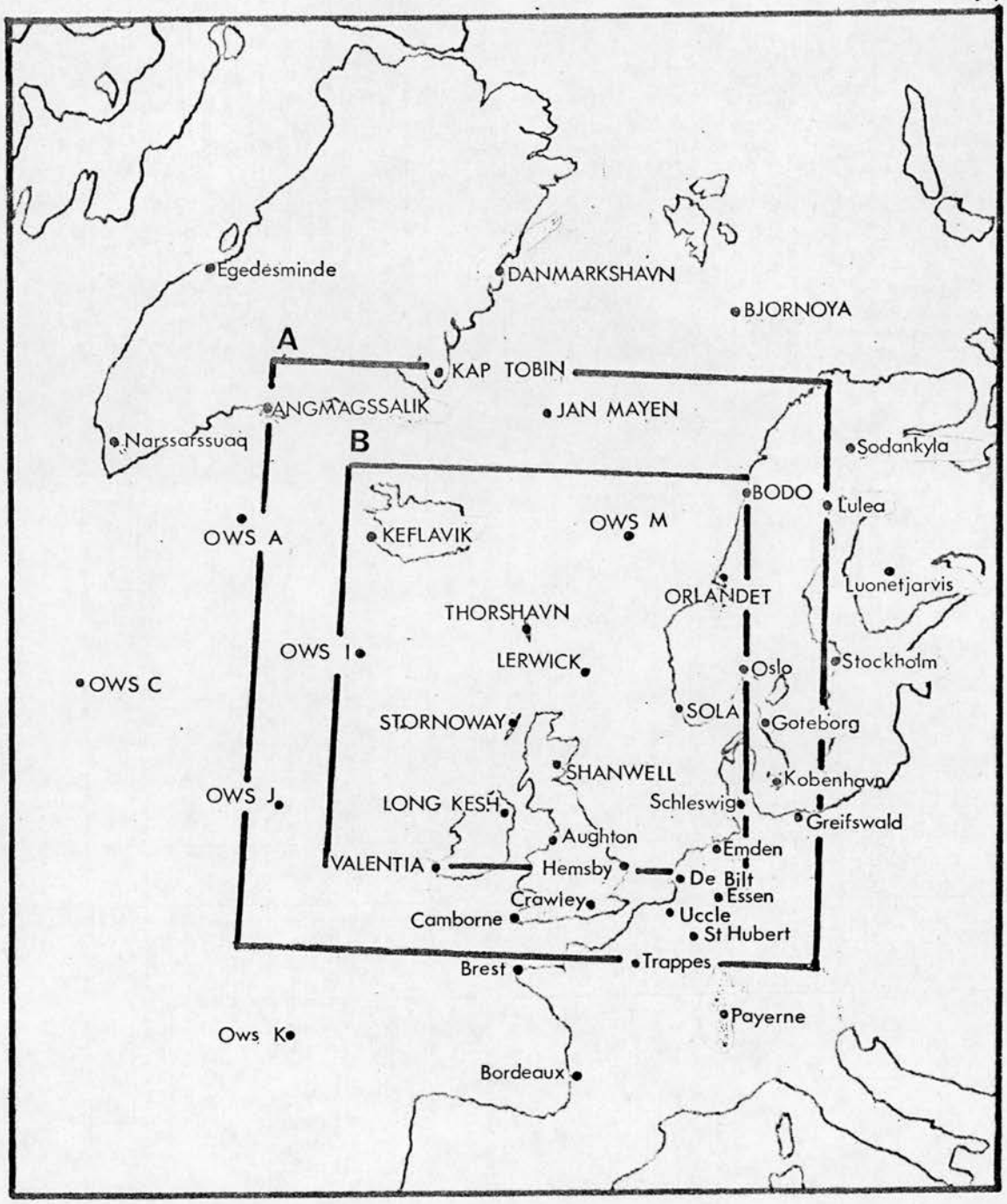

Figure 5.1 Stations used in objective analyses for case studies; upper case letters indicate stations where heights at each 50 mb level between 1000 mb and 250 mb were used; lower case letters indicate stations where heights at standard levels between 1000 mb and 300 mb were used.

The objective analysis problem is to find the coefficients, a_n, of the polynomial, P. If the number of coefficients, n, is less than the number of observations, m, then the system is over-determined and can be solved by a least squares method. The ill-conditioning problem which usually arises when m is large is greatly reduced by first finding the coefficients in orthonormal vector space, where the orthonormal vectors are obtained from the position vectors in x,y,p space, using the Gram-Schmidt process, then transforming the coefficients back to physical space. Dixon also suggests that optimum fitting is obtained when $3<m/n<4$.

5.3 Objective Analysis Test

In an area of sparse data such as that between Iceland and Scotland objective analysis may serve only to give the impression of detailed knowledge where none exists. Human analysts working in these regions use knowledge and experience to compile analyses and for this reason large differences between one human analysis and another are rarely observed. If the difference between objectively and subjectively analysed fields is similar to the difference between independent subjective analyses then the objective analysis must be acceptable.

Using observed 500 mb heights on 5th April at 00Z six subjective analyses were produced by different people. A three dimensional objective analysis was performed on the 428 observations available using a 6th power fitting ($^m/n = 5.1$). Although 7th power may be more suitable it was found that

6th power was sufficient and was capable of being calculated entirely in core store. The objectively analysed 500 mb heights were compared with the subjectively analysed fields and the subjective analyses were compared with each other. Table 5.1 shows the root mean square differences obtained in the areas shown in figure 5.1. While it is obvious that the subjective analyses are superior in the large area (A), the objective analysis appears indistinguishable from the others in the smaller area (B). The mean difference between subjective analyses is 16.9 m in area B, with a standard deviation of 3.6 m between them.

Table 5.1 R.m.s. differences between objective and subjective analyses; figures above the diagonal refer to area A and below the diagonal to area B in figure 5.1

	OBJ	A	B	C	D	E	F
OBJ		32.0	26.2	30.6	33.7	27.9	27.8
A	15.6		18.4	17.2	25.4	15.3	18.7
B	14.0	15.9		17.2	19.9	15.4	15.6
C	16.7	16.9	13.5		22.2	13.7	14.6
D	20.3	26.2	18.2	17.3		19.8	21.1
E	14.0	15.9	12.5	16.3	22.4		16.3
F	13.2	15.4	13.0	13.8	21.1	15.2	

Throughout the following case studies only objectively analysed fields were used within the small area. To ensure

that each case study was objectively analysed in a similar manner the r.m.s. difference between observed and analysed heights at every 50 mb from 1000 mb to 250 mb at selected stations was noted. The values obtained are shown in table 5.2.

Table 5.2 R.m.s. differences between observed and analysed heights at 50 mb intervals from 1000 mb to 250 mb at Keflavik, Lerwick, Stornoway, Thorshavn, O.W.S. 'I' and O.W.S. 'J'

	5.4.68	7.12.67	2.1.65
R.m.s. difference	16.7m	18.0m	11.0m
Number of observations	428	445	436

5.4 Use of Objective Analysis

The smoothing which is inherent in objective analysis was considered desirable for this study since the characteristics of the mean flow were required. By representing the continuous atmosphere by a continuous polynomial it is possible to interpolate accurately between stations and to obtain smooth, continuous derivatives. For each polar low occasion, fields of geopotential height, meridional velocity, zonal velocity and relative vorticity were obtained at 50 mb intervals between 1000 mb and 300 mb using polynomial representations for the derivatives. Also at each 50 mb level values of static stability were obtained from,

$$\sigma = \frac{1}{\theta} \frac{\partial \phi}{\partial p} \frac{\partial \theta}{\partial p} = g \left\{ \frac{\partial^2 z}{\partial p^2} + (1 - R/c_p) \frac{1}{p} \frac{\partial z}{\partial p} \right\}$$

In this case finite difference derivatives were used, with $\Delta p = 25$ mb, to obtain mean values for each 50 mb layer. Below 900 mb the vertical gradients of height appear to be less accurate, probably due to the absence of observations at pressures greater than 1000 mb. This difficulty was overcome at the upper boundary by including observations at 250 mb. It is also possible that since the observations are for 00Z the objective analysis had difficulty in reconciling the presence of a nocturnal inversion at land stations with its absence over the ocean.

5.5 5th April 1968

Between 00Z and 12Z on 5th April 1968 a polar low developed south of Iceland. The surface situation at 12Z is shown in figure 5.2a and the path taken by the depression, marked by its position at six hourly intervals, is shown in figure 5.2d. The quasi-stationary surface front indicates the baroclinic region in which the development occurred. In this area a northerly flow existed at all levels throughout the troposphere as can be seen in figure 5.3 which shows the contours of the 1000 mb, 700 mb, 500 mb and 300 mb levels. The 500 mb chart also shows (thin lines) the analysis published in the British Daily Aerological Report for this occasion. As this example was the one used to test the objective analysis in section 5.3 it is worth noting the differences and similarities between the 500 mb analyses.

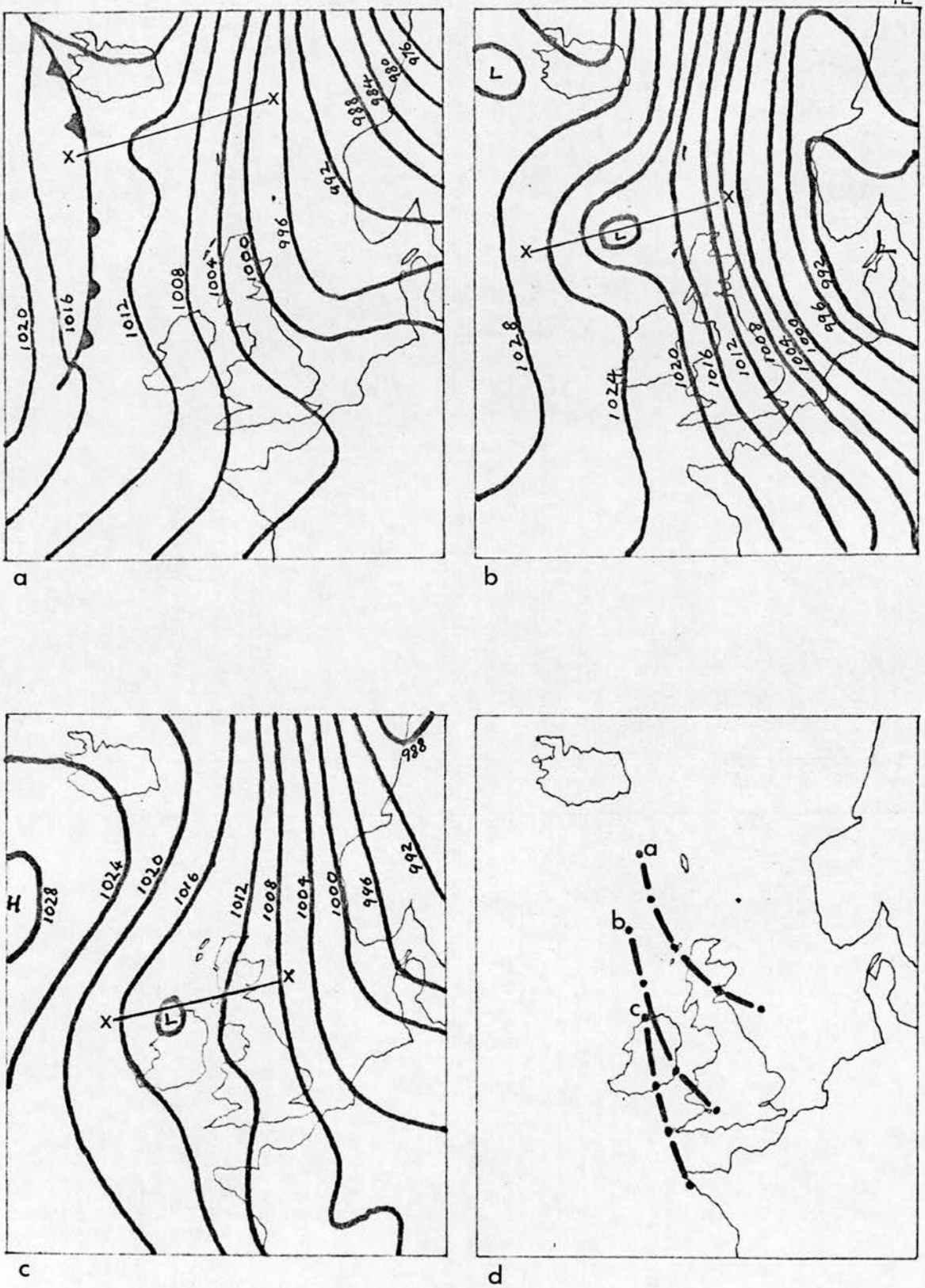

Figure 5.2 Surface analyses for each case study illustrating cross-sections used in numerical model

(a) 5th April 1968
(b) 7th December 1967
(c) 2nd January 1965
(d) Paths taken by each polar low (position indicated at six hourly intervals).

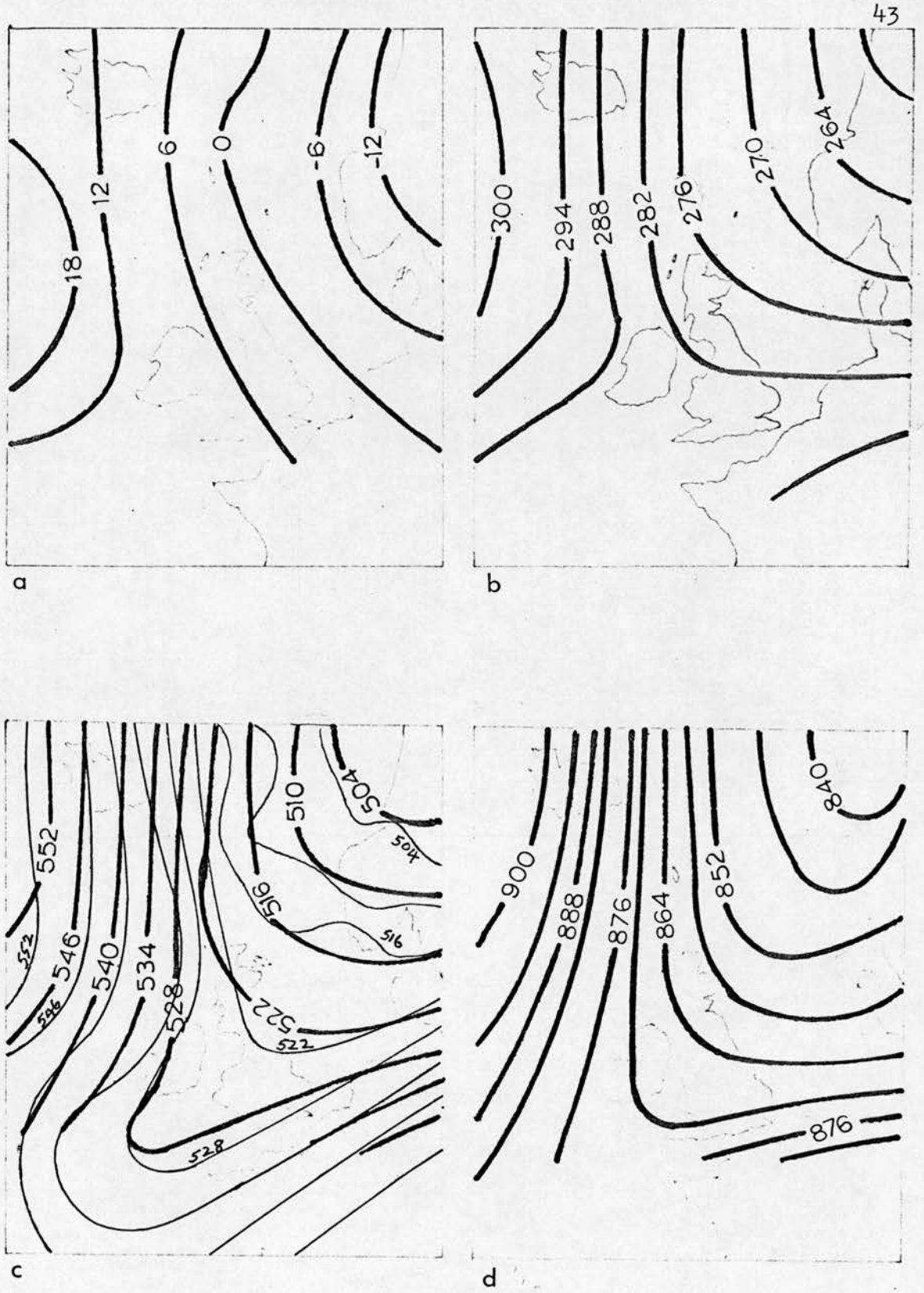

Figure 5.3 Objectively analysed surfaces; 5th April 1968, 00Z.

(a) 1000 mb
(b) 700 mb
(c) 500 mb; thin lines from U.K. Daily Aerological Report 500 mb analysis
(d) 300 mb

(Contours in decametres).

The sharpness of the major trough is well represented by the objective analysis but the minor troughs over the Norwegian sea in the Meteorological Office analysis are smoothed. However, since none of the six human analysts who participated in the test included these minor troughs it seems likely that more information must have been available for the Meteorological Office analysis. The objectively analysed contours near the edges of the area shown are well behaved, but depart more widely from observed values farther from this region. Extremes are usually not well fitted by objective analysis, but in this case good agreement is obtained, both for the anticyclone over mid-Atlantic and the depression over northern Norway resulting in an accurate estimate of the gradient near Iceland. At 850 mb the geostrophic wind, obtained from the polynomial derivative of the height field, is strongest in the baroclinic region as shown in figure 5.4a. The 1000-700 mb thickness field, figure 5.4b, indicates a strong horizontal mean temperature gradient in the area over and to the south of Iceland; along the section X-X the thickness gradient implies a vertical wind shear of 0.03 $ms^{-1}mb^{-1}$; corresponding to a horizontal temperature gradient of 11°C over 1000 Km.

To the west of the baroclinic zone the geostrophic wind veers slightly with height while to the east the wind backs, implying an intensification of the horizontal temperature gradient. Between 1000 mb and 700 mb warm air advection is largest over Ireland as the cold trough over the British Isles moves eastwards. The consequent increase in thickness over

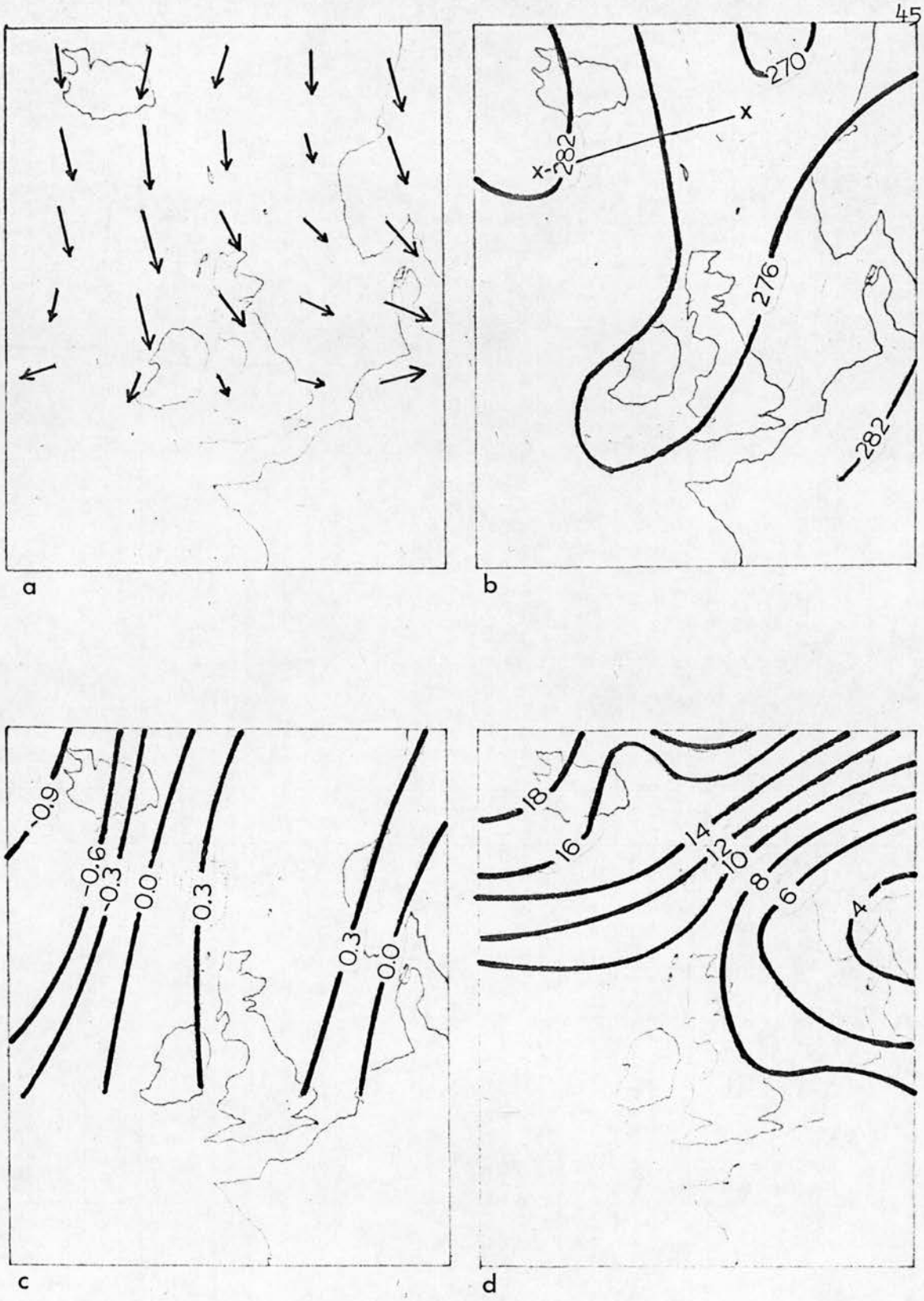

Figure 5.4 5th April 1968, 00Z.

(a) Geostrophic wind at 850 mb (1 cm=20 ms^{-1})
(b) 1000-700 mb thickness (decametres)
(c) Geostrophic vorticity at 350 mb ($x10^{-4}$ s^{-1})
(d) Mean 1000-700 mb static stability ($x10^{-3}$ m^2 s^{-2} mb^{-2}).

Ireland was probably the cause of the leftward turning of the depression on the 6th April.

Figure 5.4c shows the geostrophic vorticity, obtained by polynomial differentiation, at the 350 mb level. The condition for barotropic instability to exist is that an extreme should exist in the relative vorticity; this arises from the fact that the vorticity of the mean flow varies almost entirely along latitude lines so that variations of Coriolis parameter with latitude can be ignored. The velocity field along the section X-X is shown in figure 5.5 and this field was used in the numerical model to investigate the behaviour of unstable waves in this environment. The largest vertical wind shear exists to the west of the centre of the section below the high level jet and a vorticity extreme exists at all levels to the east of the centre. The use of a static stability, in the model, averaged over pressure surfaces is in accordance with the quasi-geostrophic assumption. An area extending 600 Km on each side of the cross-section was used to find the mean static stability and the values obtained are shown in table 5.3 along with corresponding values for the other case studies.

Although horizontal variations in static stability are neglected in the numerical model it is possible to consider the consequences in simple terms. The simplest solution for a baroclinic phenomenon is obtained by considering rigid lid upper and lower boundaries, a linear vertical wind shear,

Table 5.3 Static stabilities employed in numerical model. Averages obtained over constant pressure surfaces over an area extending 600 Km on either side of the appropriate cross-section in figure 5.2.

	Mean Static Stability (m^2 s^{-2} mb^{-2})		
Pressure	5.4.68	7.12.67	2.1.65
400	0.0379	0.0616	0.0427
500	0.0193	0.0298	0.0221
600	0.0213	0.0252	0.0168
700	0.0230	0.0111	0.0167
800	0.0111	0.0060	0.0099
900	0.0079	0.0030	0.0020

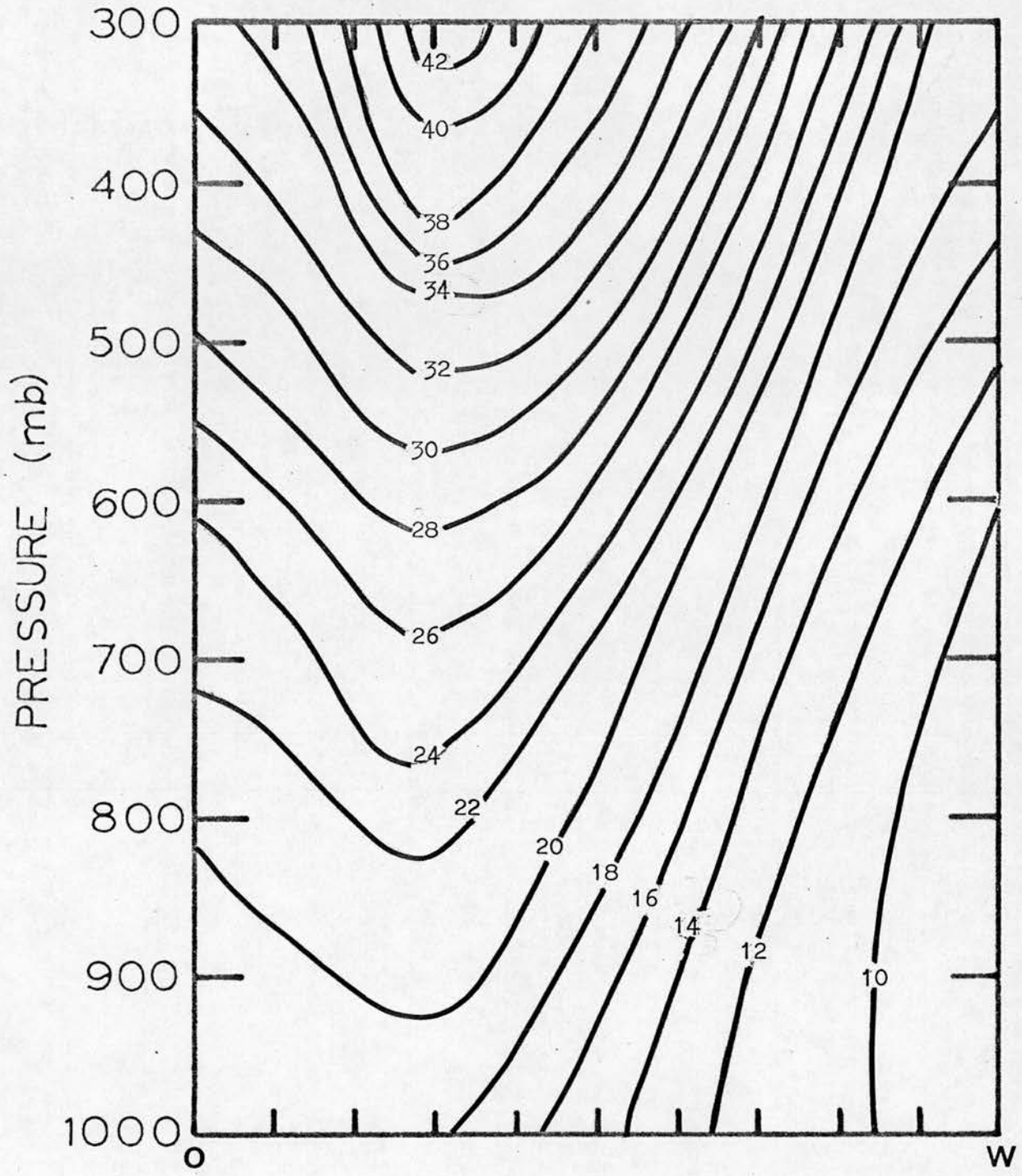

Figure 5.5 Velocity field along cross-section X-X shown in figure 5.2a (isotachs in ms^{-1}).

a constant static stability and $\beta=0$; this solution was first obtained by Eady (1949). While the growth of baroclinic waves depends upon the static stability the depth of the perturbation is also an important factor. In figure 5.6 temperature soundings for Keflavik, Thorshavn and Stornoway are shown for 00Z on the 5th April 1968. It can be seen that the depth of the low level unstable layer varies from 100 mb at Keflavik to 300 mb at Stornoway. Average static stabilities for the 1000-700 mb layer are shown in figure 5.4d. Naturally, largest values are observed where the unstable layer is shallowest in the north-west of the region shown. The most unstable wavelengths for the Eady problem are shown in figure 5.7 as a function of static stability and depth of unstable layer. The corresponding short wavelength cut-off to instability is also illustrated. With the conditions shown in the lowest 300 mb at Stornoway the most unstable Eady wave would be between 900 Km and 1000 Km. At the other stations shorter wavelengths would be expected since the unstable layer, though shallower than that at Stornoway, is similar in intensity. Mansfield (1972) has described the effect of friction on shallow baroclinic waves; in addition to the expected damping he suggests a shift of the wavelength of maximum instability towards longer values. The situation on 5th April 1968 therefore suggests unstable waves with horizontal and vertical dimensions similar to polar lows. A more detailed description of waves developing under less restrictive conditions is given in the next chapter.

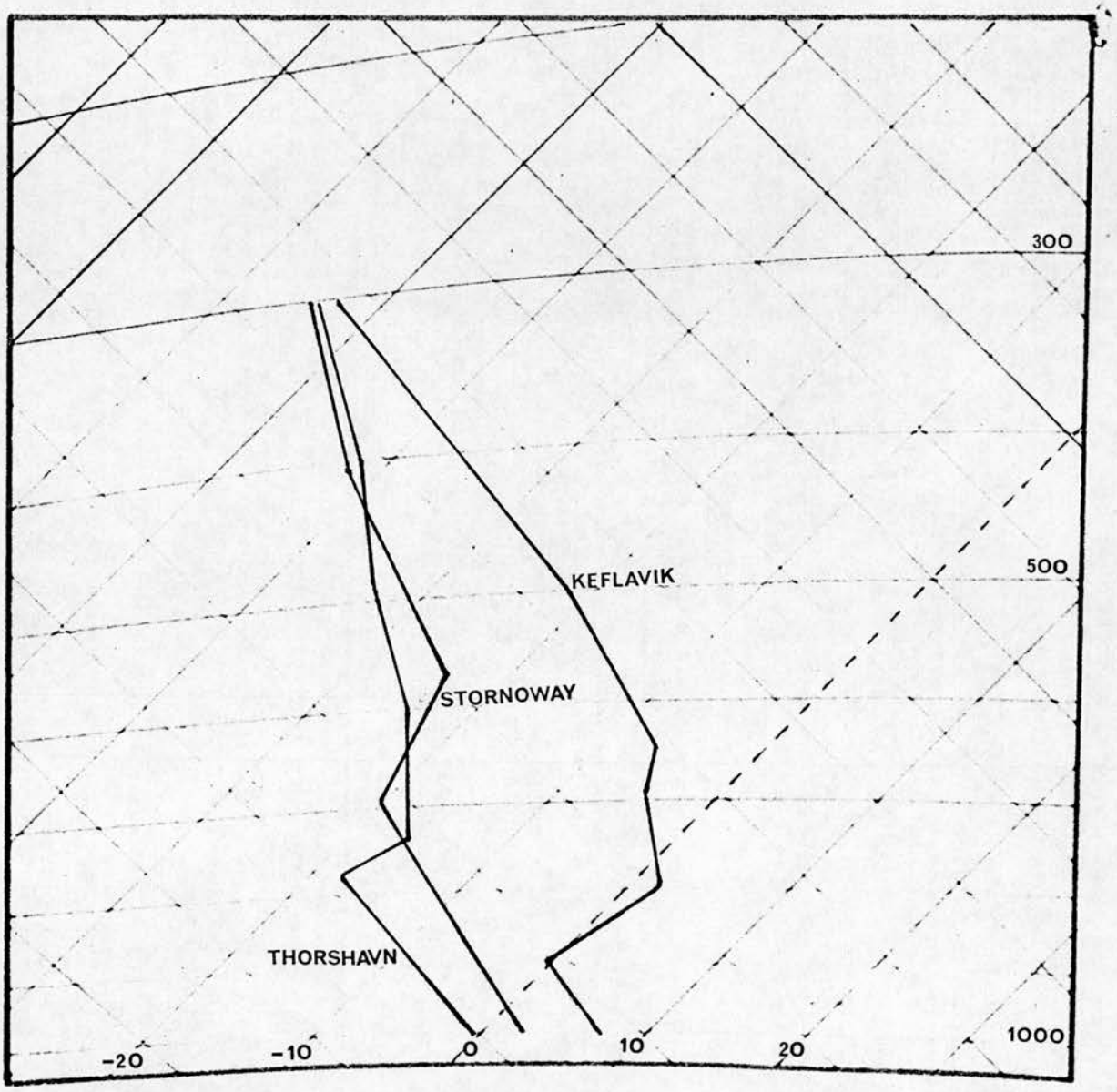

Figure 5.6 Temperature soundings for Thorshavn, Stornoway and Keflavik at 00Z on 5th April 1968.

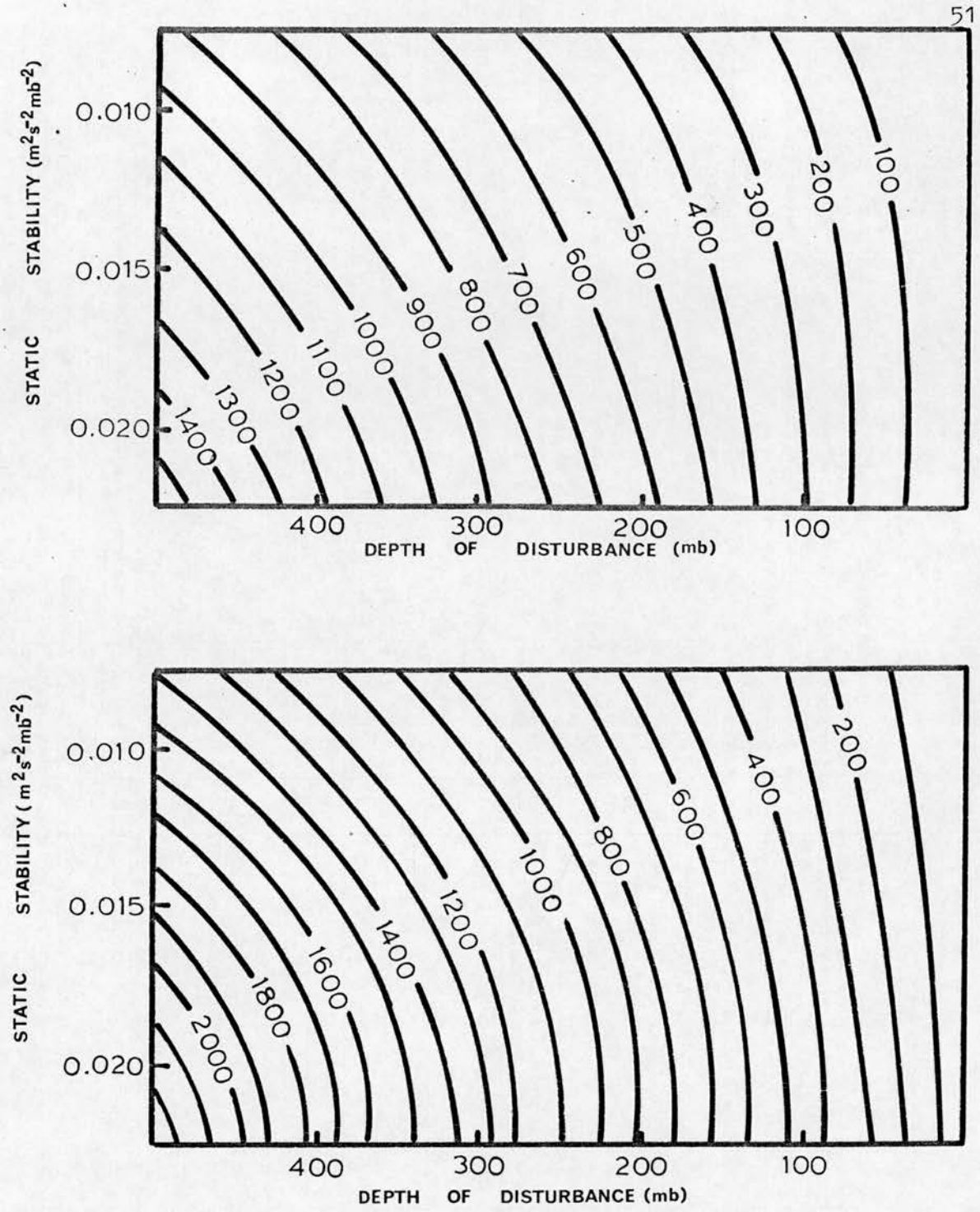

Figure 5.7 Above: Short wave cut-off to instability, for Eady problem, as a function of static stability and disturbance depth; $f=1.26 \times 10^{-4}\ s^{-1}$. (Isopleths in Km).

Below: Wavelength of maximum instability for Eady problem as a function of static stability and disturbance depth; $f=1.26 \times 10^{-4}\ s^{-1}$. (Isopleths in Km).

5.6 7th December 1967

Two polar lows crossed Britain on the 7th and 9th December 1967 after developing originally to the west of Iceland. Only the first of these depressions will be studied here. Mansfield (1972) has pointed out that this polar low developed in a baroclinic region to the west of Iceland, and Harrold and Browning (1969) identified a shallow baroclinic zone as the depression passed across the British Isles. The surface situation at 12Z on the 7th December is shown in figure 5.2b and the subsequent path of the depression in figure 5.2d. The second low can be seen to the west of Iceland and the separation of the centres at this stage is 1000 ± 150 Km. As the first low was still developing at this stage it is appropriate to use a linear model in this study. Objectively analysed contours for the 1000 mb, 700 mb, 500 mb and 300 mb levels are shown in figure 5.8 with the 500 mb analysis from the British Daily Aerological Report also shown in figure 5.8c. The mean flow is well represented by these objectively analysed fields since neither perturbation is observed at the 1000 mb level. A strong jet is apparent at the 300 mb level with geostrophic winds of about 56 ms^{-1} over Ireland and S.W. England.

At low levels a large horizontal wind shear exists. This is particularly noticeable in the 850 mb level winds in figure 5.9a. In figure 5.9b the 1000-700 mb thickness indicates that the region of greatest wind shear is to the west of the developing depression. There are two probable

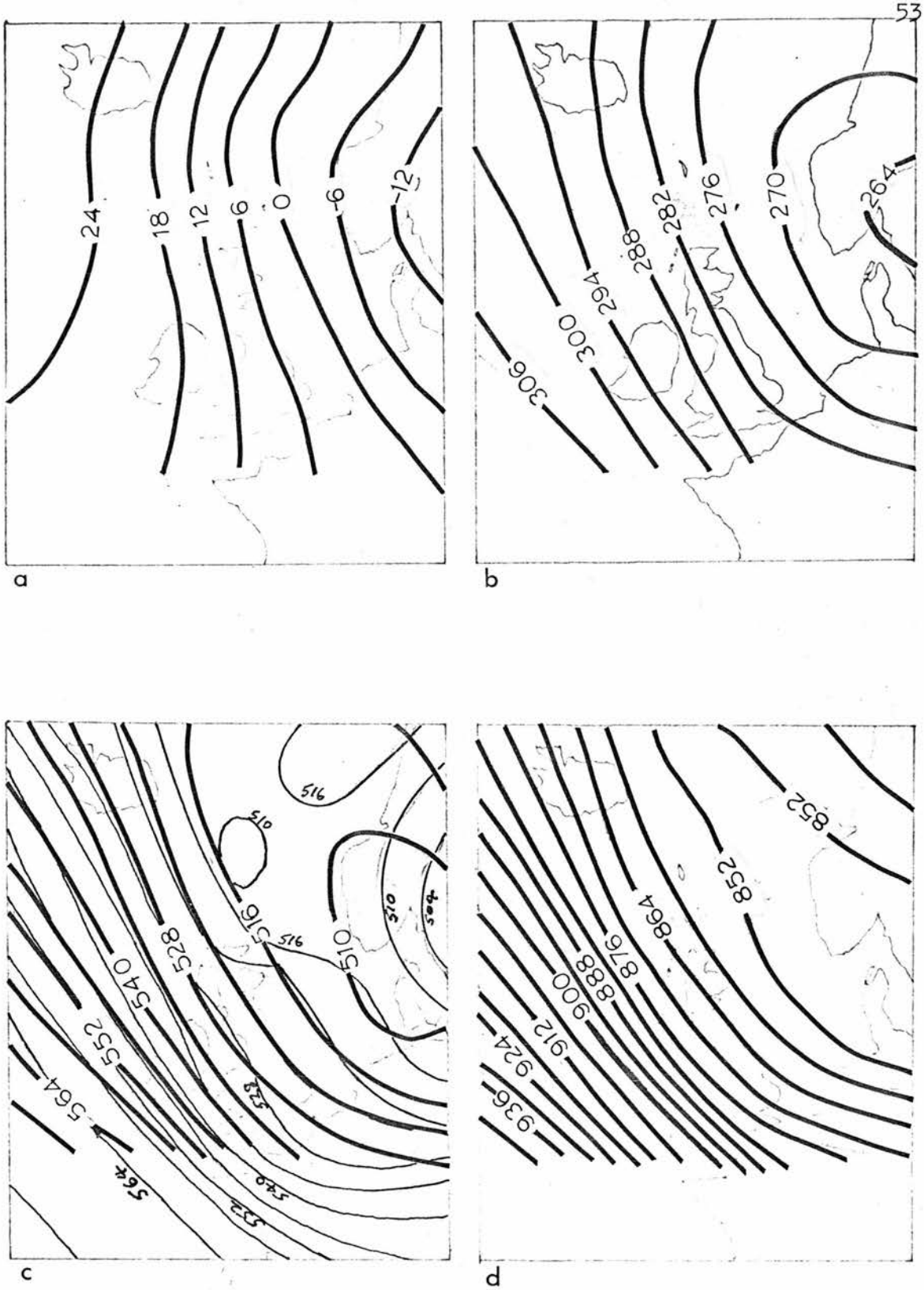

Figure 5.8 Objectively analysed surfaces; 7th December 1967, 00Z.

(a) 1000 mb
(b) 700 mb
(c) 500 mb; thin lines from U.K. Daily Aerological Report 500 mb analysis
(d) 300 mb

(Contours in decametres).

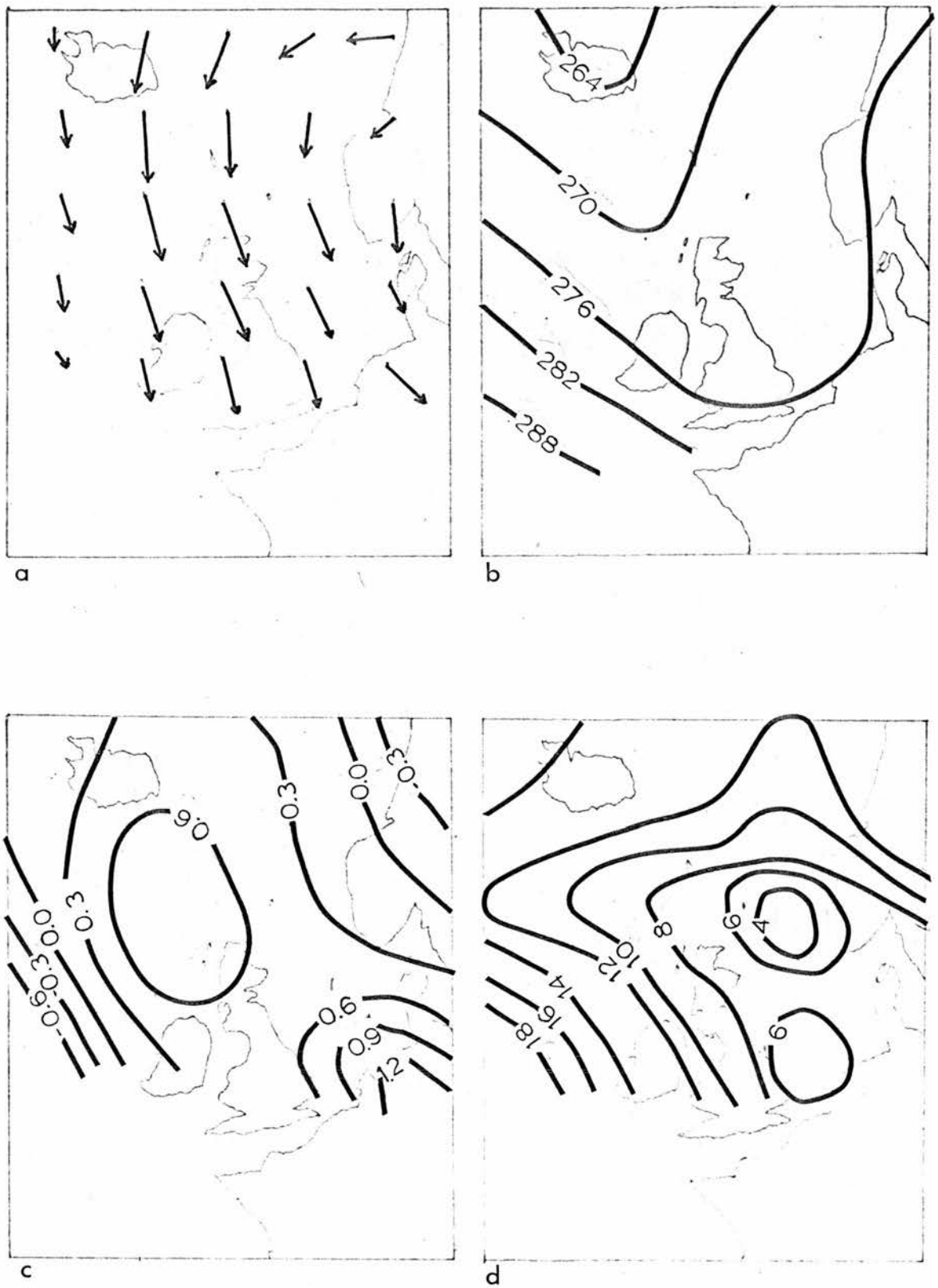

Figure 5.9 7th December 1967, 00Z.

(a) 850 mb geostrophic winds (1 cm = 20 ms^{-1})

(b) 1000-700 mb thickness (decametres)

(c) 350 mb geostrophic vorticity ($x10^{-4}$ s^{-1})

(d) Mean 1000-700 mb static stability ($x10^{-3}$ m^2 s^{-2} mb^{-2}).

reasons why the area with greater wind shear was not preferred; the large horizontal shear already mentioned may have had a damping effect and the mean 1000-700 mb static stability shown in figure 5.9d was larger in the area of strong shear, implying smaller growth rates than in the area in which the depression did develop. A maximum in the geostrophic vorticity existed at 350 mb, figure 5.9c, almost directly above the polar low.

Temperature soundings from Stornoway, Thorshavn and O.W.S. 'I', shown in figure 5.10, illustrate an unstable layer from the surface to between 650 mb and 700 mb. This implies that the wavelength of maximum instability is between 1000 Km and 1150 Km for Eady waves if the static stability is 0.01 $m^2 s^{-2} mb^{-2}$. Weak cold air advection existed below 700 mb over all of the area between Iceland and the south of England so that the baroclinic zone was neither weakened nor strengthened.

The velocity field in the vertical cross-section X-X in figure 5.2b exhibits an intense jet at 300 mb, shown in figure 5.11. Where low level baroclinity exists a strong horizontal wind shear is also present. Velocities shown are normal to the cross-section, as was the direction of travel of the depression.

5.7 2nd January 1965

The surface northerly flow in which a polar low developed to the north of Ireland is shown in figure 5.2c. At higher levels the flow backed slightly and figure 5.12 illustrates this at the 1000 mb, 700 mb, 500 mb and 300 mb levels. The

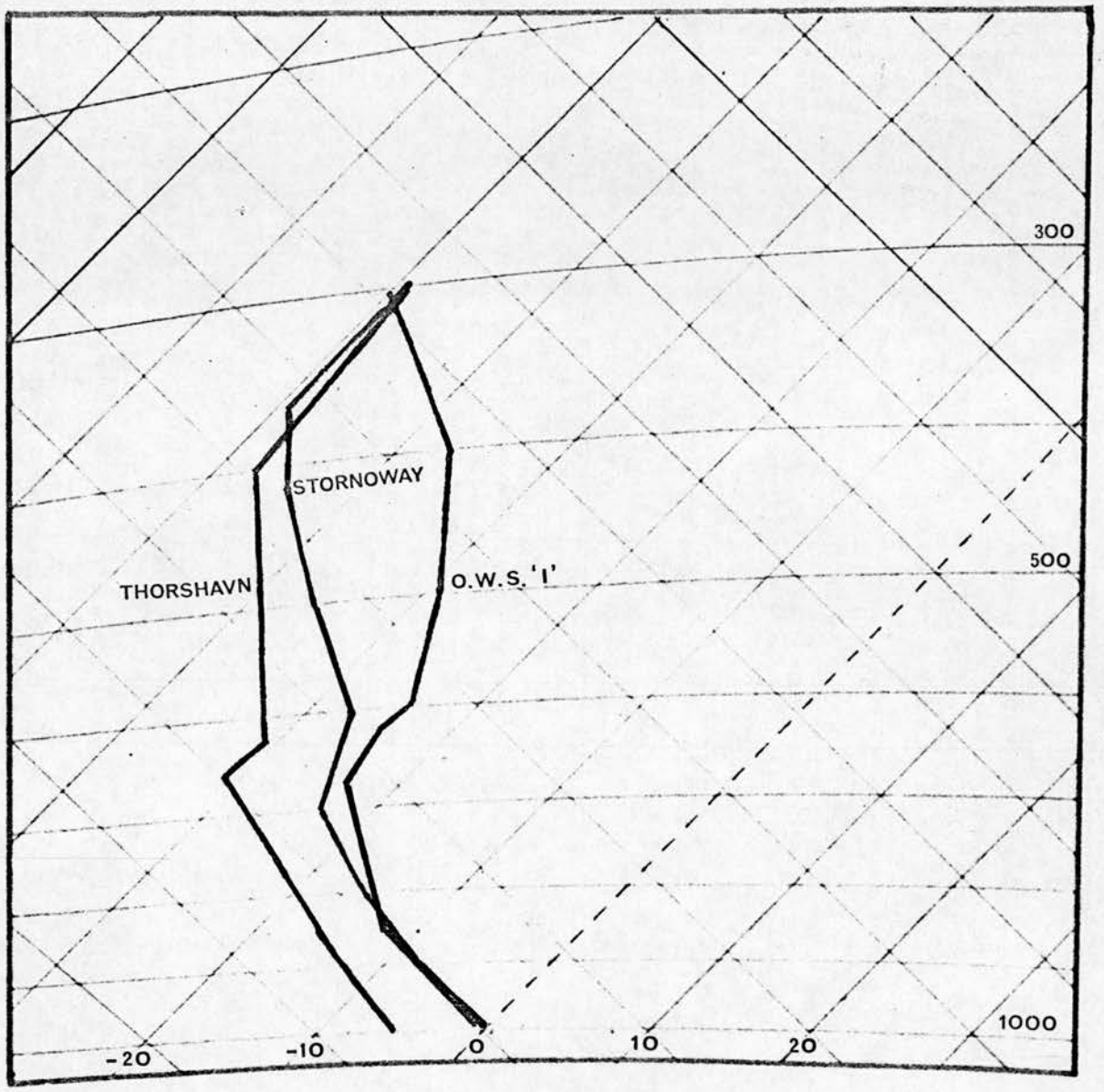

Figure 5.10 Temperature soundings for Thorshavn, Stornoway and O.W.S. 'I' at 00Z on 7th December 1967.

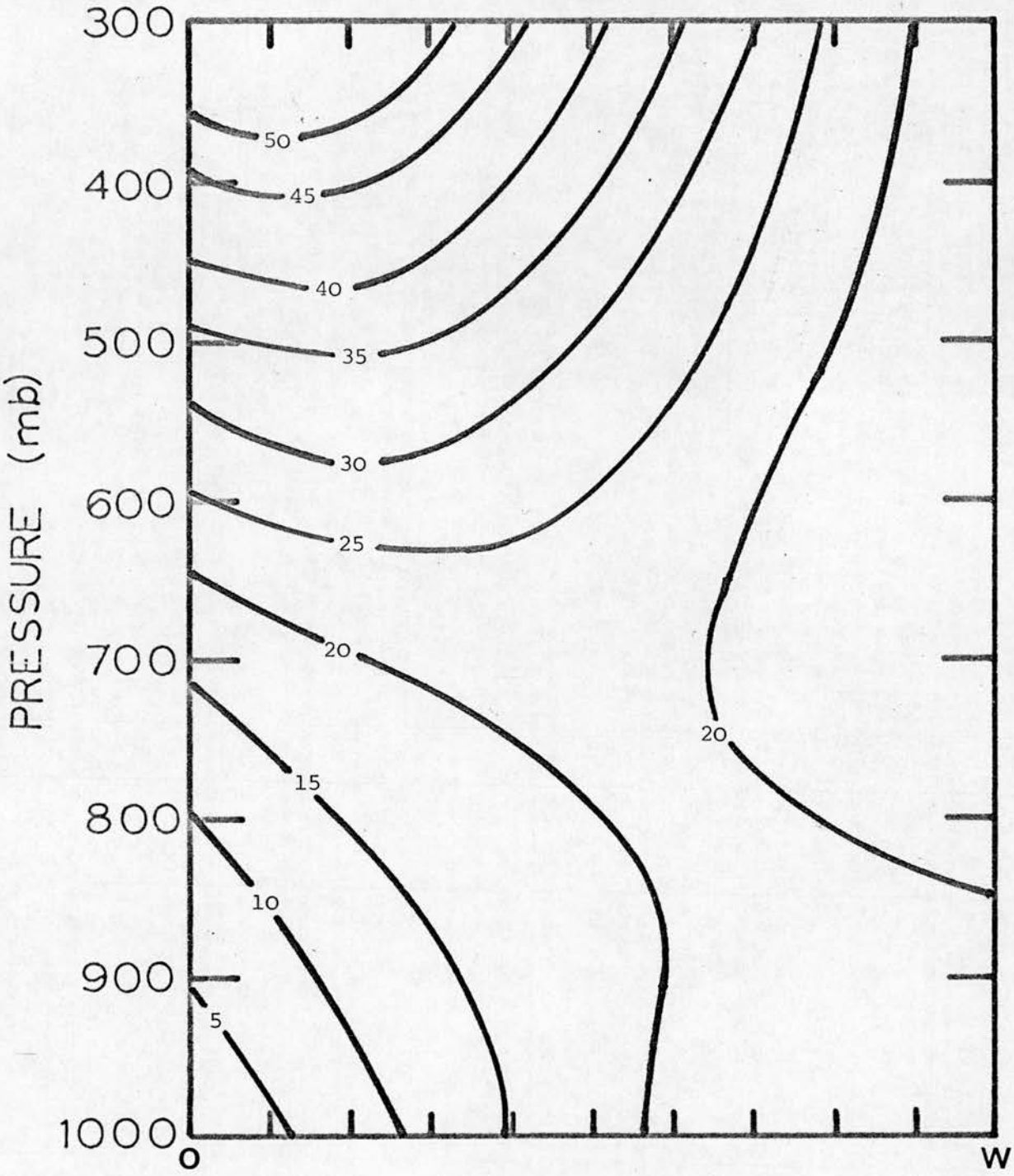

Figure 5.11 Velocity field along cross-section X-X in figure 5.2b (isotachs in ms^{-1}).

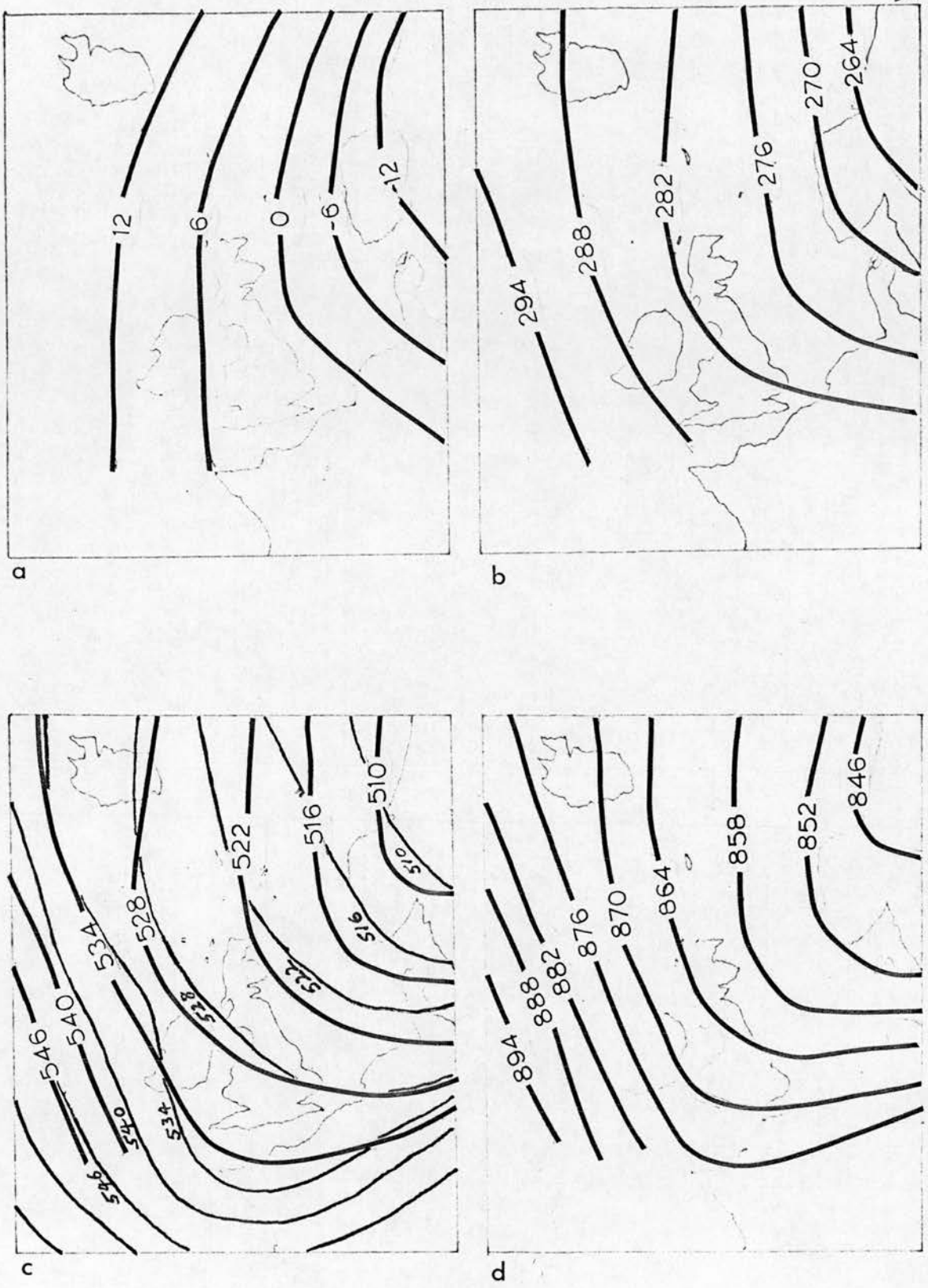

Figure 5.12 Objectively analysed surfaces, 2nd January 1965, 00Z.

(a) 1000 mb
(b) 700 mb
(c) 500 mb, thin lines from U.K. Daily Aerological Report 500 mb analysis
(d) 300 mb

(Contours in decametres).

thermal wind in the lowest 300 mb, as indicated by the 1000-700 mb thickness, is not parallel to the mean flow in this layer, as shown in figure 5.13. Growth of unstable waves will be diminished under these circumstances since the efficiency of the baroclinic process is reduced. Figure 5.13 also gives the relative vorticity and mean 1000-700 mb static stability fields. Very low values of mean static stability are observed near Northern Ireland and at 900 mb σ is negative in this region. At Long Kesh the 00Z radio-sonde ascent shows a shallow nocturnal inversion. The January mean sea surface temperature to the north of Ireland is about $9^{o}C$ so that over the sea the boundary layer would be unstable, as it was at O.W.S. 'I' and Valentia, figure 5.14, where the wind was from the sea.

The static stabilities shown in table 5.3 and the geostrophic wind field, figure 5.15, were used in the numerical model. These winds correspond to values on the cross-section X-X in figure 5.2c.

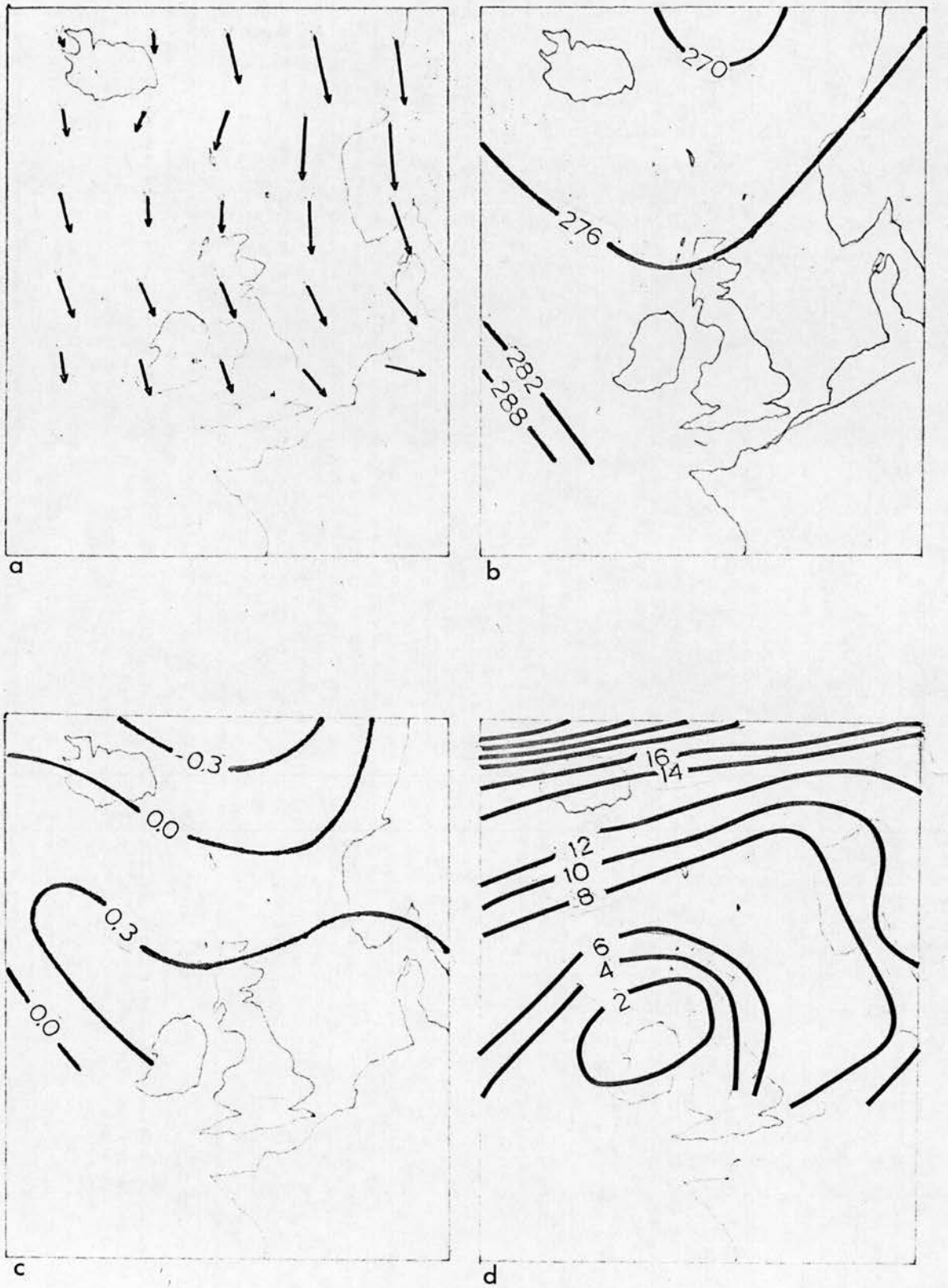

Figure 5.13 2nd January 1965, 00Z.

(a) 850 mb geostrophic winds (1cm=20 ms^{-1})
(b) 1000-700 mb thickness (decametres)
(c) 350 mb geostrophic vorticity (x10^{-4} s^{-1})
(d) Mean 1000-700 mb static stability (x 10^{-3} m^2 s^{-2} mb^{-2}).

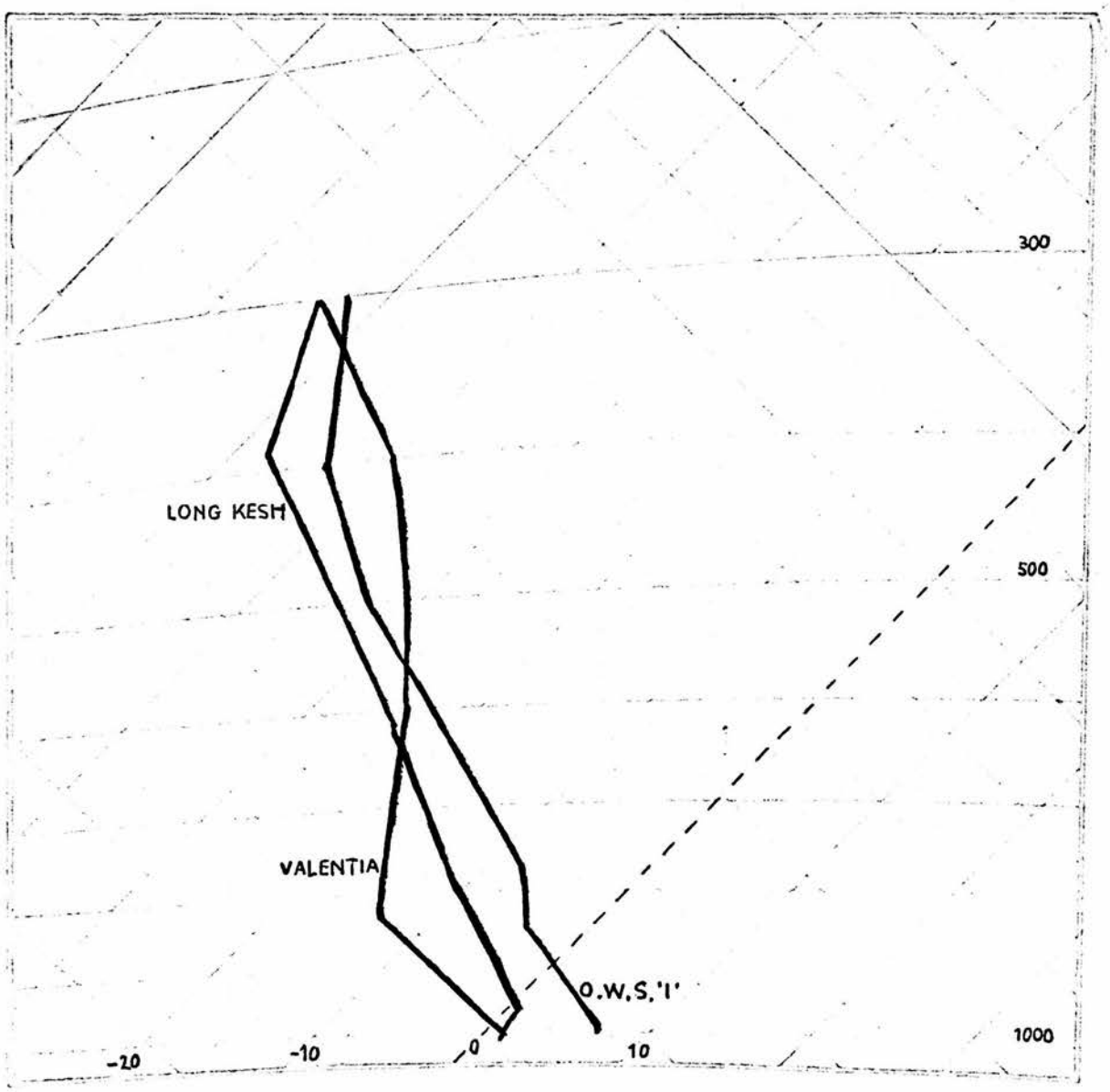

Figure 5.14 Temperature soundings for Long Kesh, Valentia and O.W.S. 'I' at 00Z on 2nd January 1965.

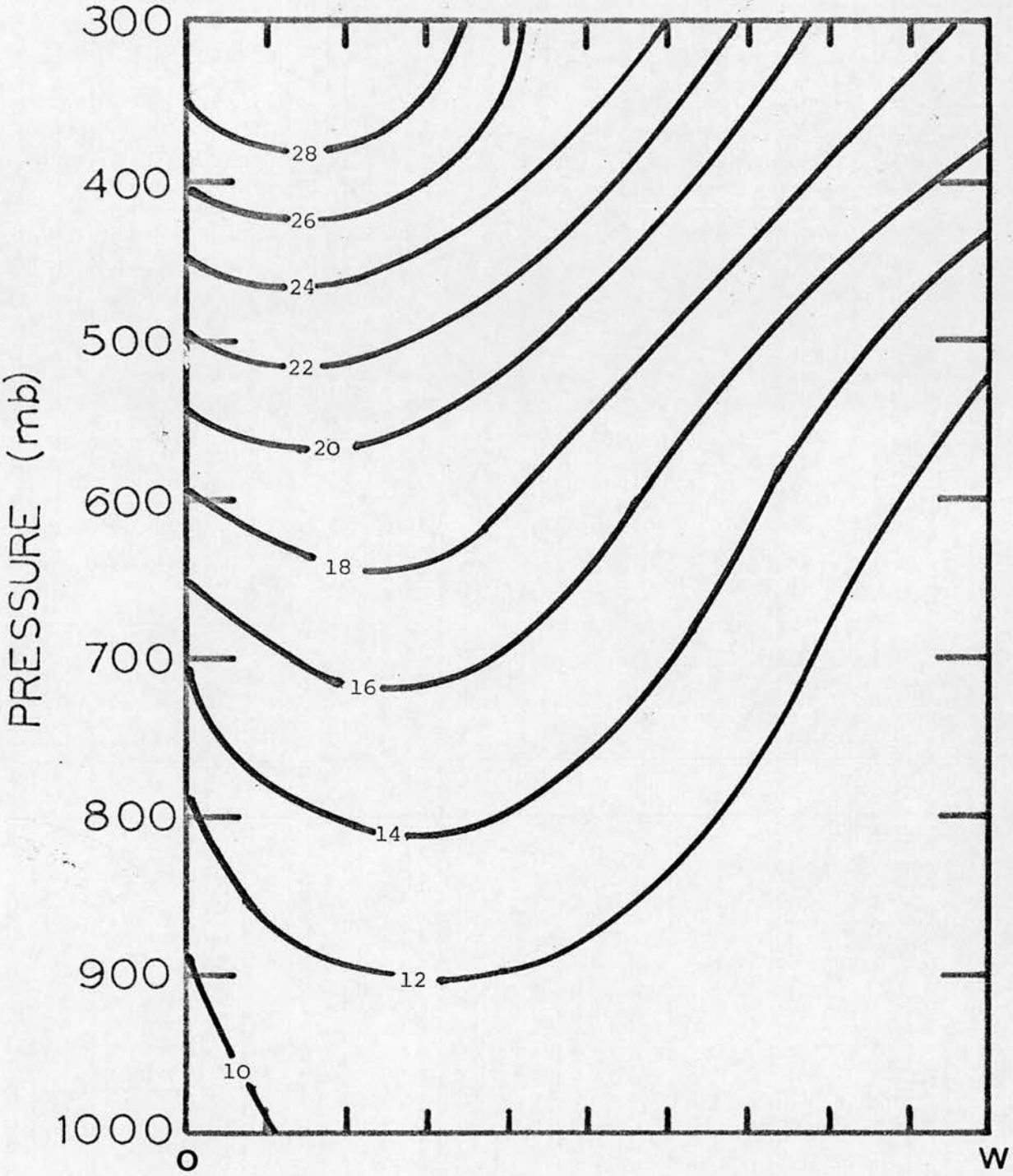

Figure 5.15 Velocity field along cross-section X-X in figure 5.2c (isotachs in ms^{-1}).

CHAPTER 6

CASE STUDY RESULTS

6.1 Introduction

Using the velocity fields illustrated in figures 5.5, 5.11 and 5.15 and the static stabilities in table 5.3 the range of wavelengths from 4000 Km to 400 Km was investigated by means of the numerical model. Convergence rates were found to be much slower in these realistic situations than in the earlier examples and the convergence tolerance was therefore reduced to $\varepsilon = 0.1$ ms^{-1}.

In each experiment the Coriolis parameter used was 1.26×10^{-4} s^{-1}. A vertical difference of 50 mb and a horizontal grid length of 120 Km were used. As before, the time step used was varied with wavelength to allow rapid convergence at longer wavelengths.

6.2 5th April 1968

The model rates of growth and the wave speeds appropriate to conditions on 5th April 1968 are shown in figure 6.1. The most unstable wavelength was 1500 Km, with a growth rate of 0.48 day^{-1} and a phase speed of 20.5 ms^{-1}; these compare with observed values at 12Z of a wavelength of 1100 $\pm$ 200 Km and a phase speed of 12 $\pm$ 1 ms^{-1}. The effect of removing the channel walls and allowing the wavelength to extend laterally to infinity is to reduce the most unstable wavelength to 1272 Km.

The relative streamfunction amplitude, figure 6.2, illustrates that the perturbation is largest at low levels

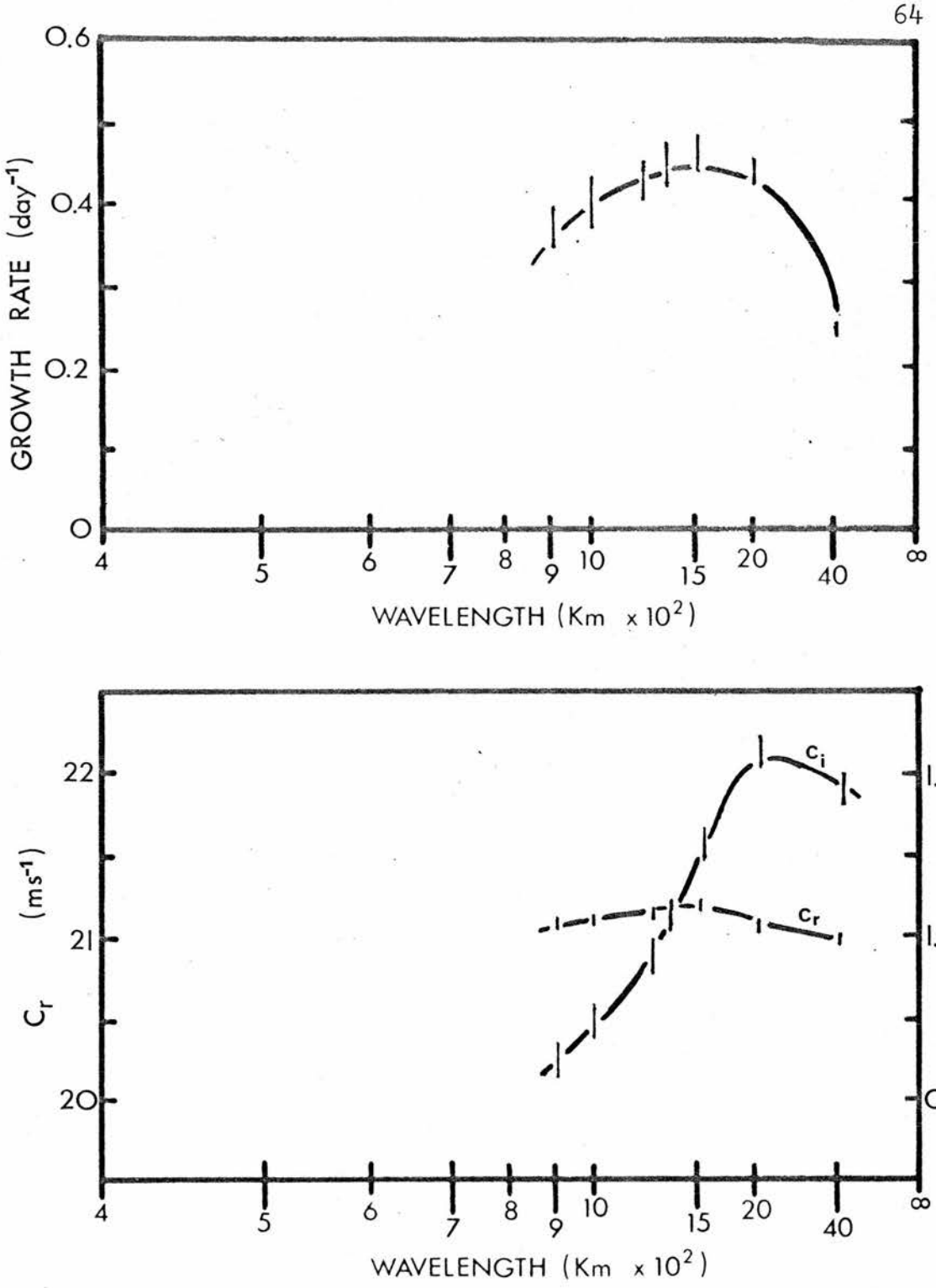

Figure 6.1 5th April 1968.

Above: Growth rate as a function of wavelength.

Below: Real and imaginary wave speeds as a function of wavelength.

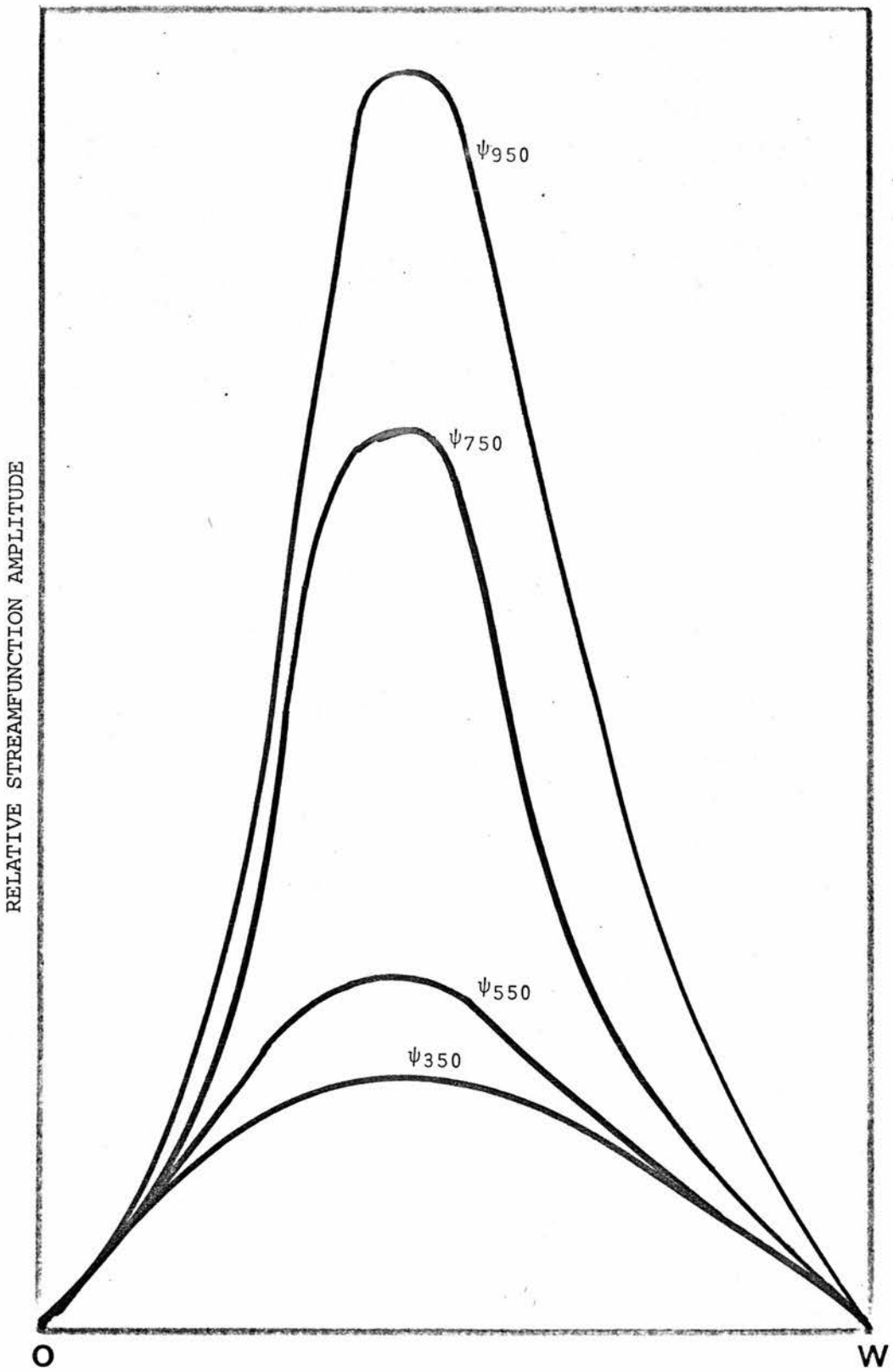

Figure 6.2 5th April 1968; Relative streamfunction amplitude at 950, 750, 550, 350 mb for the 1500 Km wave.

for the 1500 Km wave. The vertical averages of eddy kinetic energy and available potential energy, not shown, indicate a broad maximum in the eddy kinetic energy near the centre of the channel.

Typically, a baroclinic wave developing under frictionless conditions has a phase lag of about $\pi/2$ between the trough and vertical velocity maximum. This is true only near the centre of the channel in this case, as can be seen in figure 6.3. The backward tilt of the trough line is most pronounced in the lowest 300 mb, implying that at upper levels the trough and thermal wave are almost in phase. Since the perturbation amplitude decreases rapidly with height above 700 mb the warm part of the thermal wave becomes almost in phase with the trough. Also shown are the relative phases of trough and maximum vertical velocity at one grid length from the eastern and western sides of the channel where energy conversion rates are very small.

The eddy available potential energy is largest close to the surface where static stabilities are low while the vertical eddy kinetic energy distribution, figure 6.4, indicates a decrease above 700 mb. At this level eddy kinetic energy increases are due entirely to vertical convergence of kinetic energy since the conversion of eddy available potential energy to eddy kinetic energy is virtually confined to the 950-750 mb layer. Figure 6.4 also illustrates the energy conversion rates, averaged over constant pressure surfaces, as a function of pressure. At all levels, particularly near the surface,

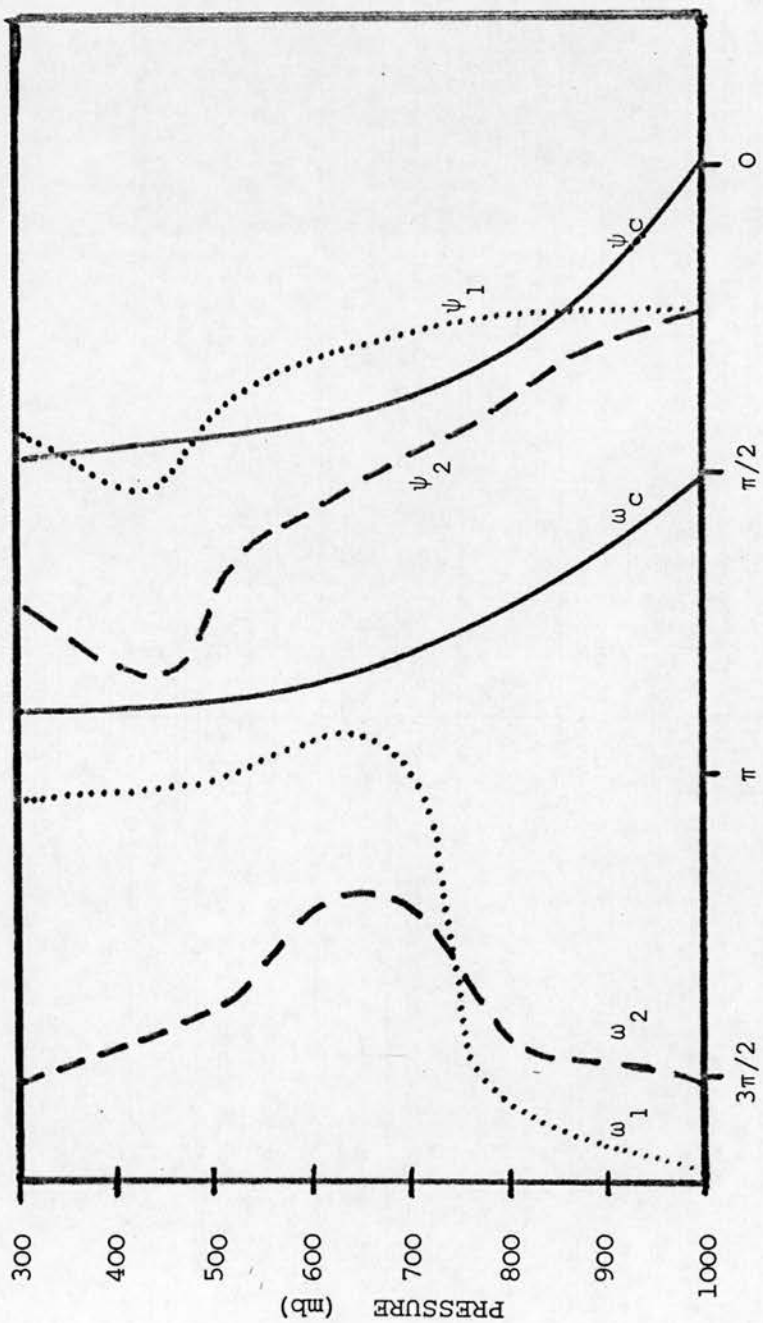

Figure 6.3 5th April 1968; relative streamfunction and vertical velocity phases for 1500 Km wave. Subscripts refer to, c, centre of channel, 1, one grid length from eastern channel wall, 2, one grid length from western channel wall.

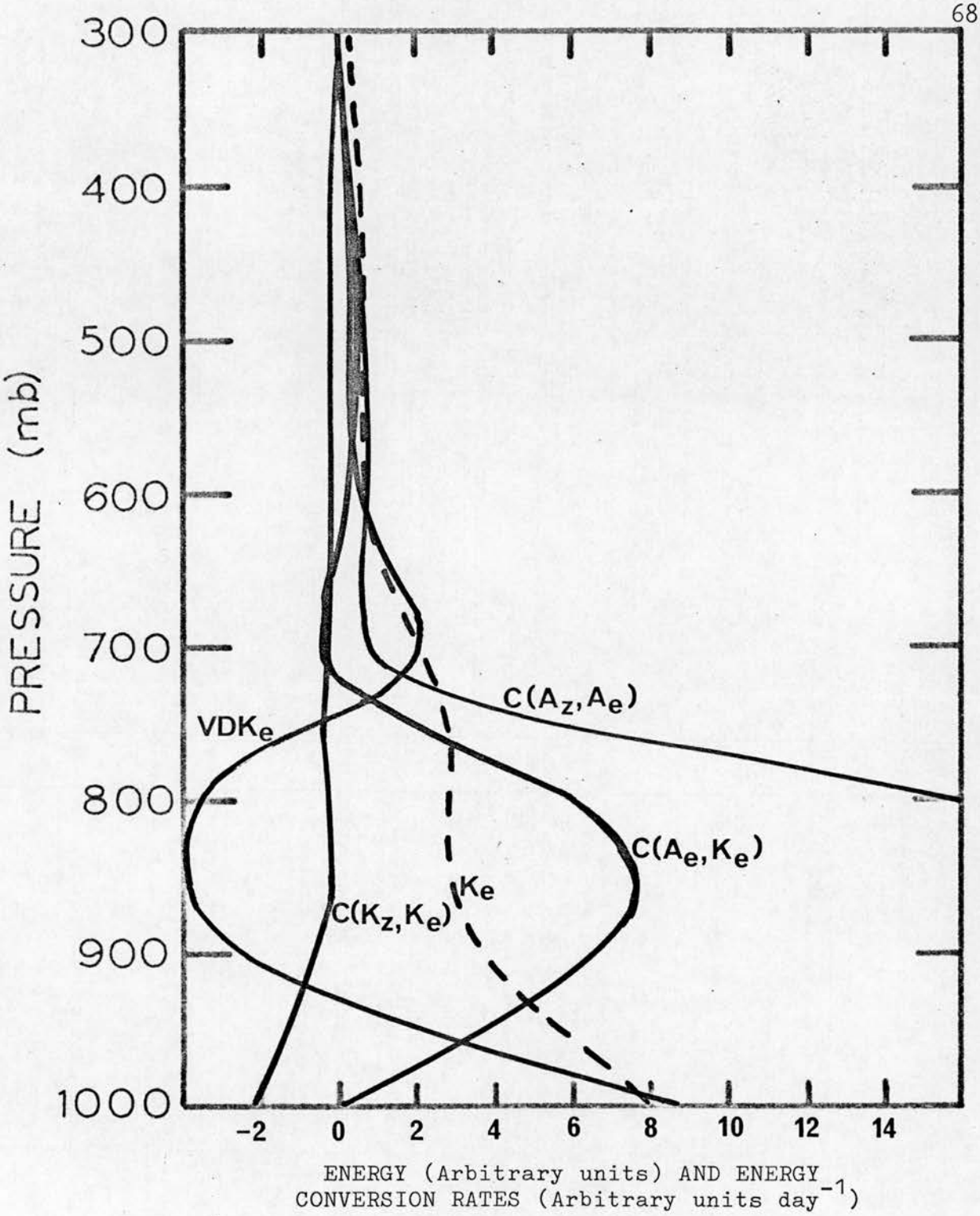

Figure 6.4 5th April 1968; Horizontally averaged energy and energy conversion rates for 1500 Km wave.

a kinetic energy sink exists in the form of conversion of eddy kinetic energy to zonal kinetic energy. The large eddy kinetic energy near 1000 mb is due to downward transfer of kinetic energy from the 800-900 mb layer.

When averages over constant pressure surfaces are taken the conversion of zonal to eddy kinetic energy and lateral divergence of kinetic energy are very small. This is not true, however, at different points across the channel, as shown in figure 6.5. Vertically averaged energy conversion rates show that at many grid points the conversion of eddy available potential energy to eddy kinetic energy is considerably smaller than either the lateral divergence of kinetic energy or the conversion of zonal to eddy kinetic energy. However, the last two of these almost counteract each other so that their sum has a negative contribution to $\frac{\partial K_e}{\partial t}$ near the centre of the disturbance and a positive contribution near the sides, leading to a broad region of large eddy kinetic energy growth.

The model disturbance appears to describe accurately the depression which developed on 5th April 1968 with the exception of the phase speed. Friction would reduce the phase speed, but the model value of 20.5 ms^{-1} appears high in spite of this. In the model the perturbation at 500 mb has about one third of the surface perturbation amplitude. No trough is shown in the 500 mb chart of the Daily Aerological Report although this may be due to the distance between the disturbance and the nearest upper air station.

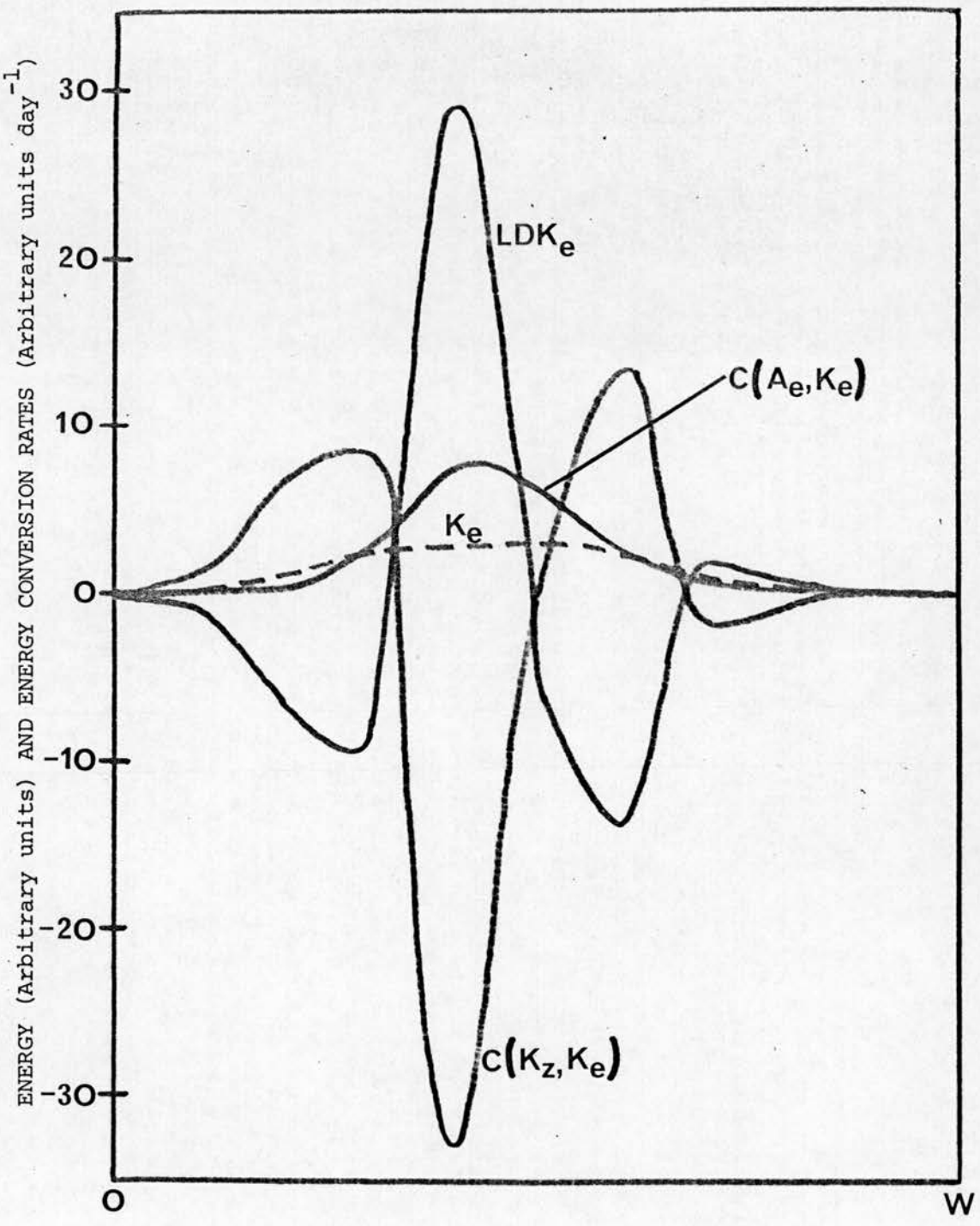

Figure 6.5 5th April 1968; vertically averaged energy and energy conversion rates for the 1500 Km wave.

6.3 7th December 1967

The velocity field in figure 5.11 illustrates two low-level baroclinic regions. On the western side of the cross-section the wind speed increases with height so that the thermal wind is in the same direction as the mean flow. At low levels on the eastern side the wind speed decreases with height and the thermal wind is in the opposite direction to the mean flow. If the static stabilities shown in table 5.3 are used in the numerical model the upper growth rate curve, shown in figure 6.6, is obtained. However, if the 900 mb static stability is doubled to 0.006 $m^2\ s^{-2}\ mb^{-2}$, the lower curve is obtained. The real and imaginary wave speeds shown correspond to the latter case. It can be seen that the phase speed increases as the wavelength decreases; the opposite is true for the situation where $\sigma = 0.003\ m^2\ s^{-2}\ mb^{-2}$ at 900 mb.

It appears that two distinctly different modes of instability exist and that the static stability at 900 mb determines the dominant mode. The relative streamfunction amplitudes for the 450 Km wave with $\sigma = 0.003\ m^2\ s^{-2}\ mb^{-2}$ and the 900 Km wave with $\sigma = 0.006\ m^2\ s^{-2}\ mb^{-2}$ at 900 mb are shown in figures 6.7 and 6.8 respectively. It can be seen that the two unstable modes occur at opposite sides of the channel; the longer wave on the eastern side of the channel and the shorter wave, corresponding to $\sigma = 0.003\ m^2\ s^{-2}\ mb^{-2}$, on the western side.

The relative phases of the trough and vertical velocity

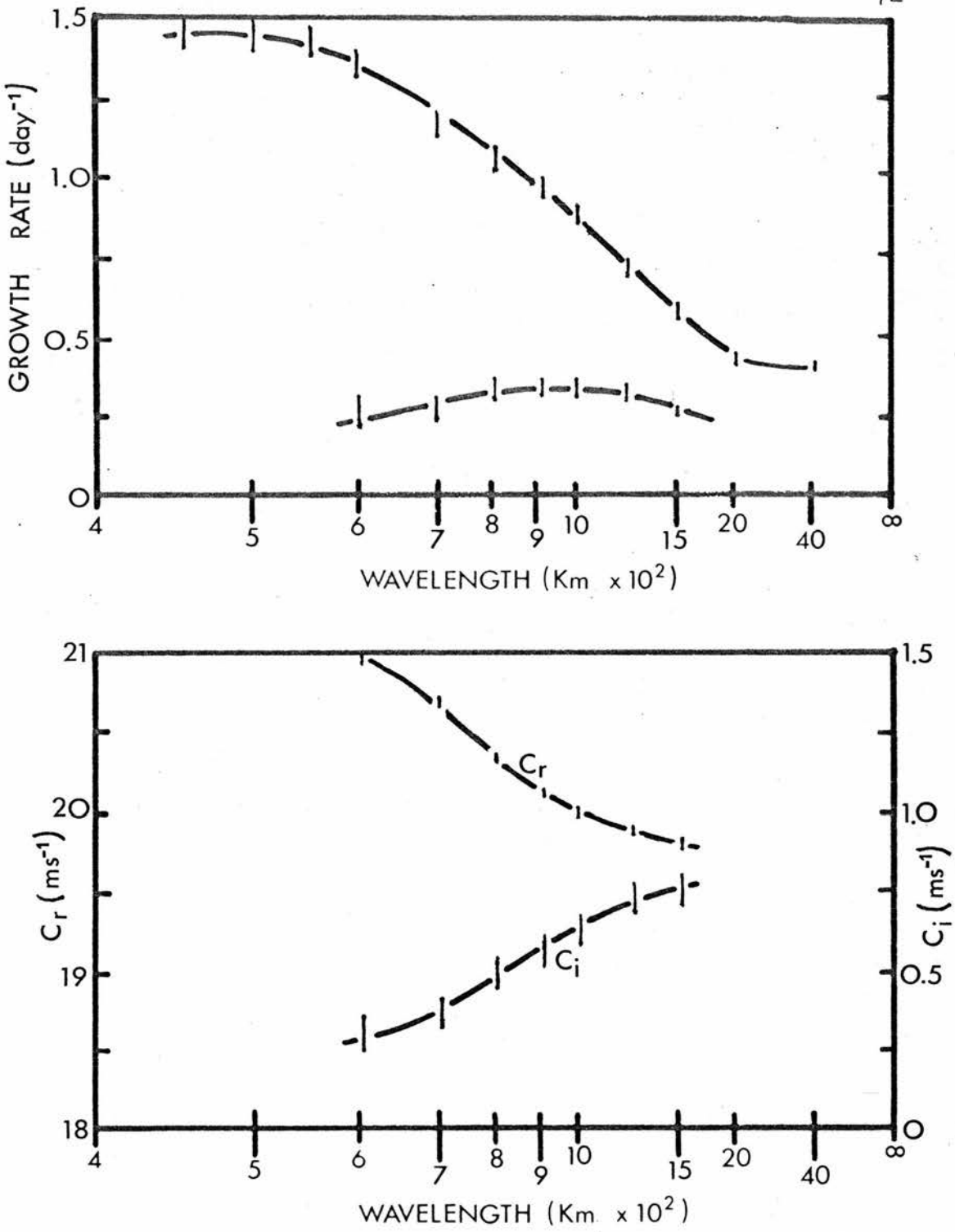

Figure 6.6 7th December 1967.

Above: Growth rate as a function of wavelength for $\sigma = 0.003\ m^2\ s^{-2}\ mb^{-2}$ at 900 mb (upper curve) and $\sigma = 0.006\ m^2\ s^{-2}\ mb^{-2}$ at 900 mb (lower curve).

Below: Real and imaginary wave speeds corresponding to lower growth rate curve.

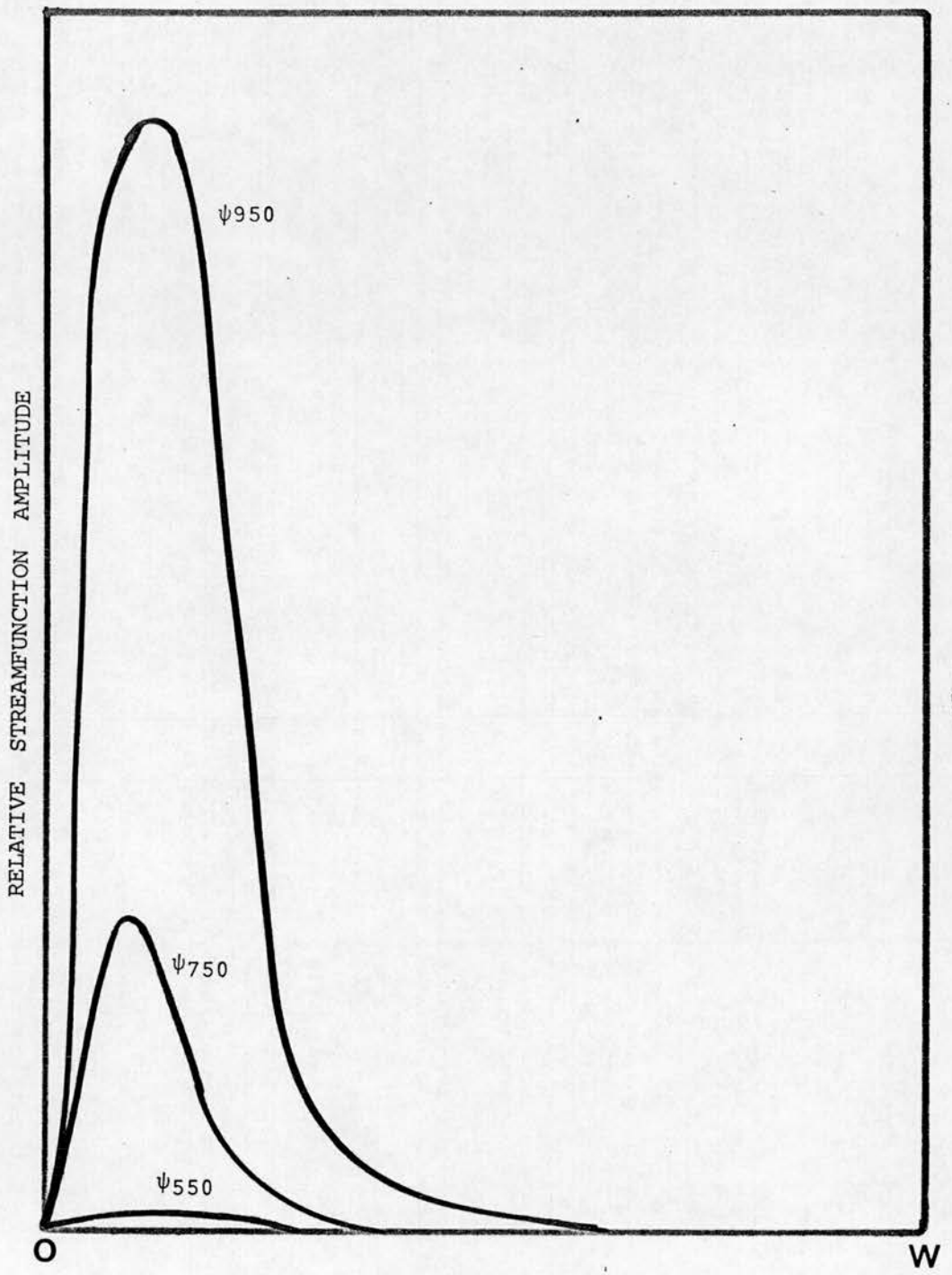

Figure 6.7 7th December 1967; relative streamfunction amplitude at 950, 750 and 550 mb for 450 Km wave with σ=0.003 m^2 s^{-2} mb^{-2} at 900 mb.

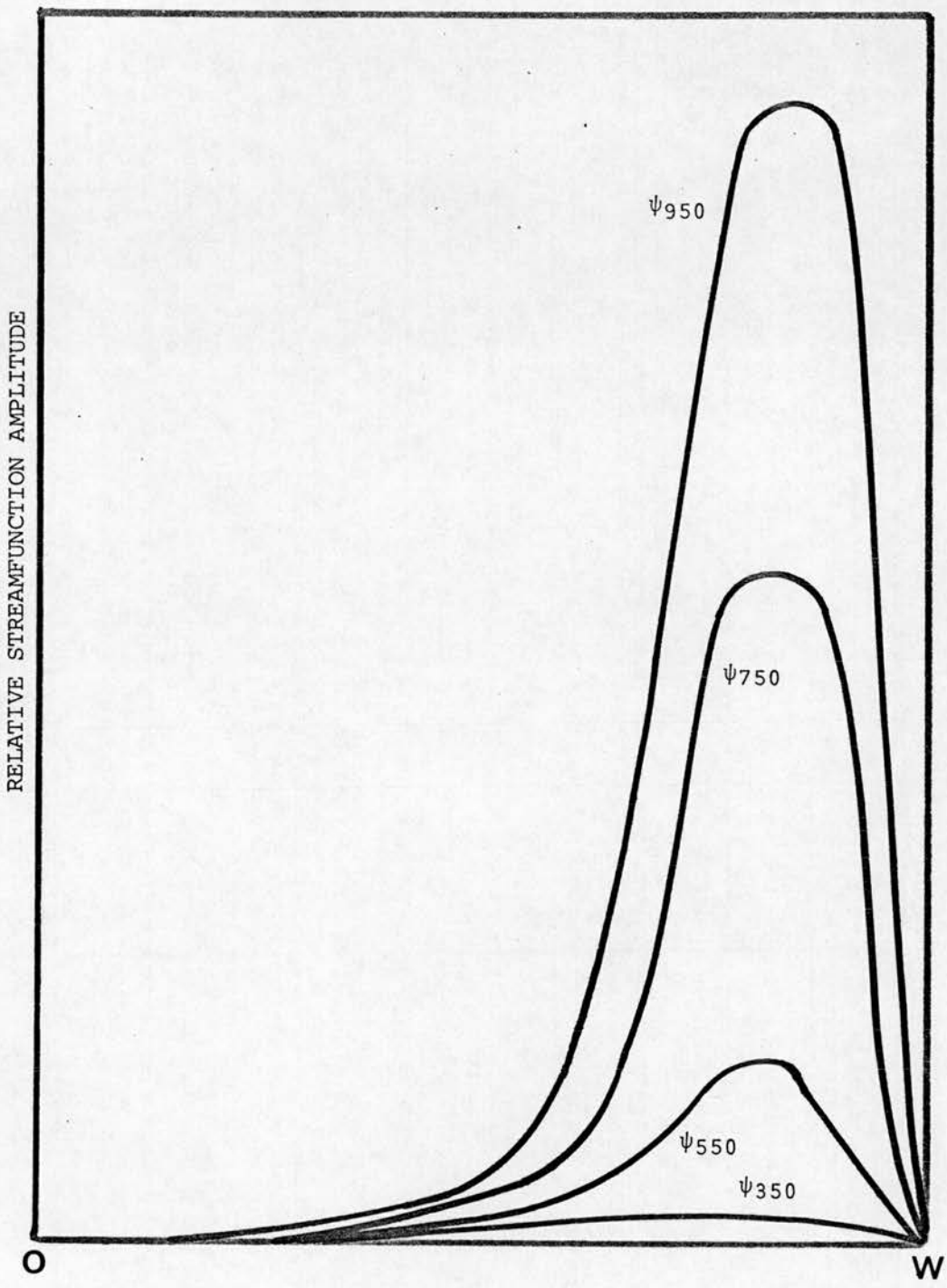

Figure 6.8 7th December 1967; relative streamfunction amplitude at 950, 750, 550 and 350 mb for the 900 Km wave with σ=0.006 m^2 s^{-2} mb^{-2} at 900 mb.

of the 450 Km wave on the western side of the channel are shown in figure 6.9. The horizontally averaged eddy kinetic energy, not shown, is large only below 800 mb in the 450 Km wave.

Figure 6.10 illustrates the relative phases of the trough and vertical velocity of the 900 Km wave at the eastern side of the channel. Although the conversion of eddy available potential energy to eddy kinetic energy is positive only below 700 mb in this wave, the horizontally averaged eddy kinetic energy, figure 6.11, indicates that convergence of eddy kinetic energy exists between 700 mb and 500 mb. The vertically averaged energy conversion rates for the 900 Km wave are shown in figure 6.12; the structure of this wave can be seen to be very similar to the waves described previously, despite the fact that in this situation the wind speed decreases with height. This example illustrates that polar lows may develop in the absence of a high level jet stream if low level vertical wind shear exists.

The unstable waves which developed in the numerical model bear little resemblance to the polar low which developed on 7th December 1967. Due to the imposed condition that the static stability should be constant over constant pressure surfaces, growth is encouraged in regions where, in reality, it would be inhibited by large static stabilities. Experiments which specified static stabilities of 0.005 and 0.004 $m^2\ s^{-2}\ mb^{-2}$ at 900 mb were also carried out; the former led to unstable waves similar to those obtained with $\sigma = 0.006\ m^2\ s^{-2}\ mb^{-2}$ with

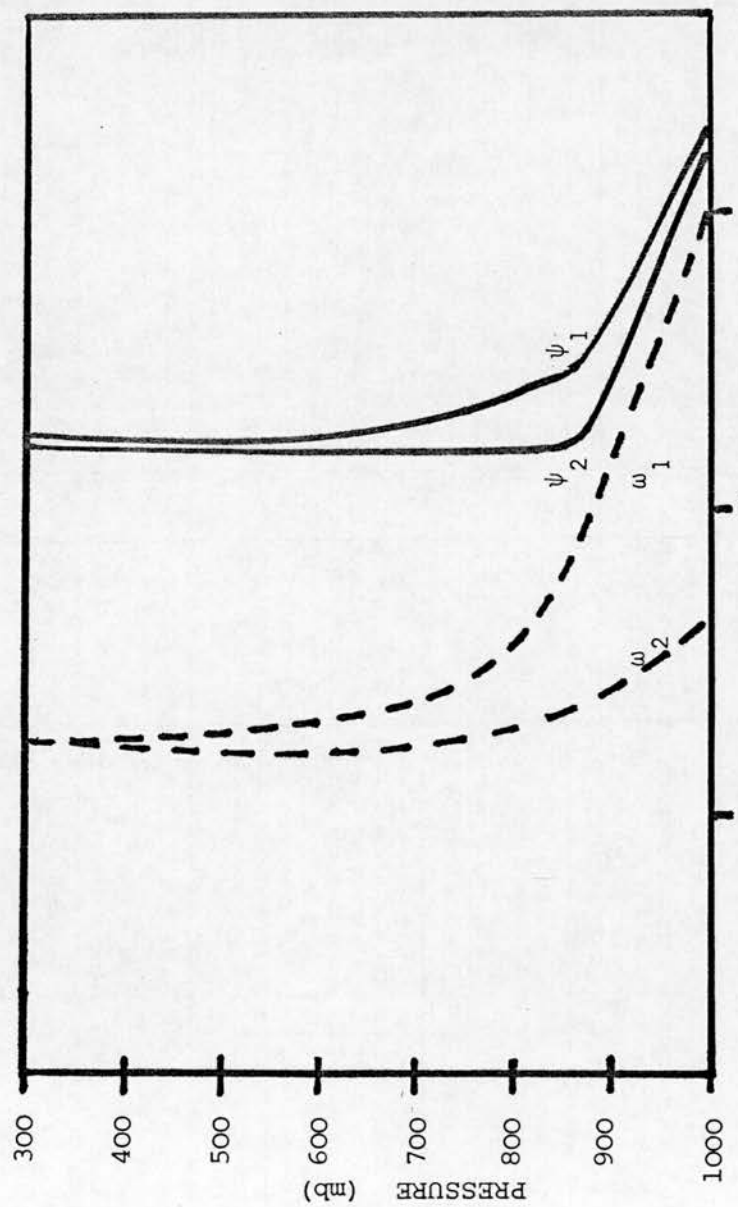

Figure 6.9 7th December 1967; relative streamfunction and vertical velocity phases at one grid length (subscript 1) and two grid lengths (subscript 2) from western channel wall, for 450 Km wave with σ=0.003 m^2 s^{-2} mb^{-2} at 900 mb.

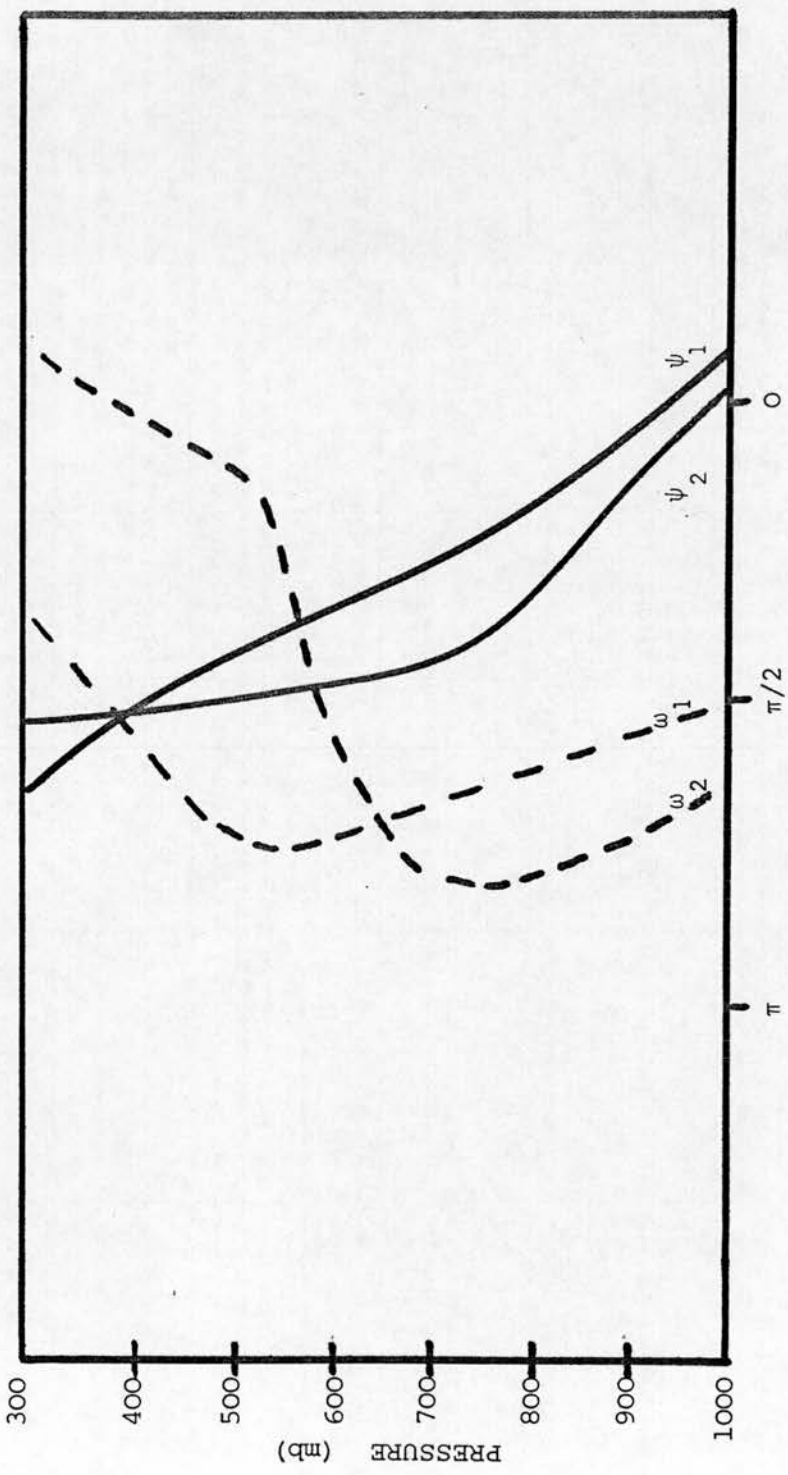

Figure 6.10 7th December 1967; relative streamfunction and vertical velocity phases at one grid length (subscript 1) and two grid lengths (subscript 2) from eastern channel wall, for 900 Km wave where σ=0.006 $m^2 s^{-2} mb^{-2}$ at 900 mb.

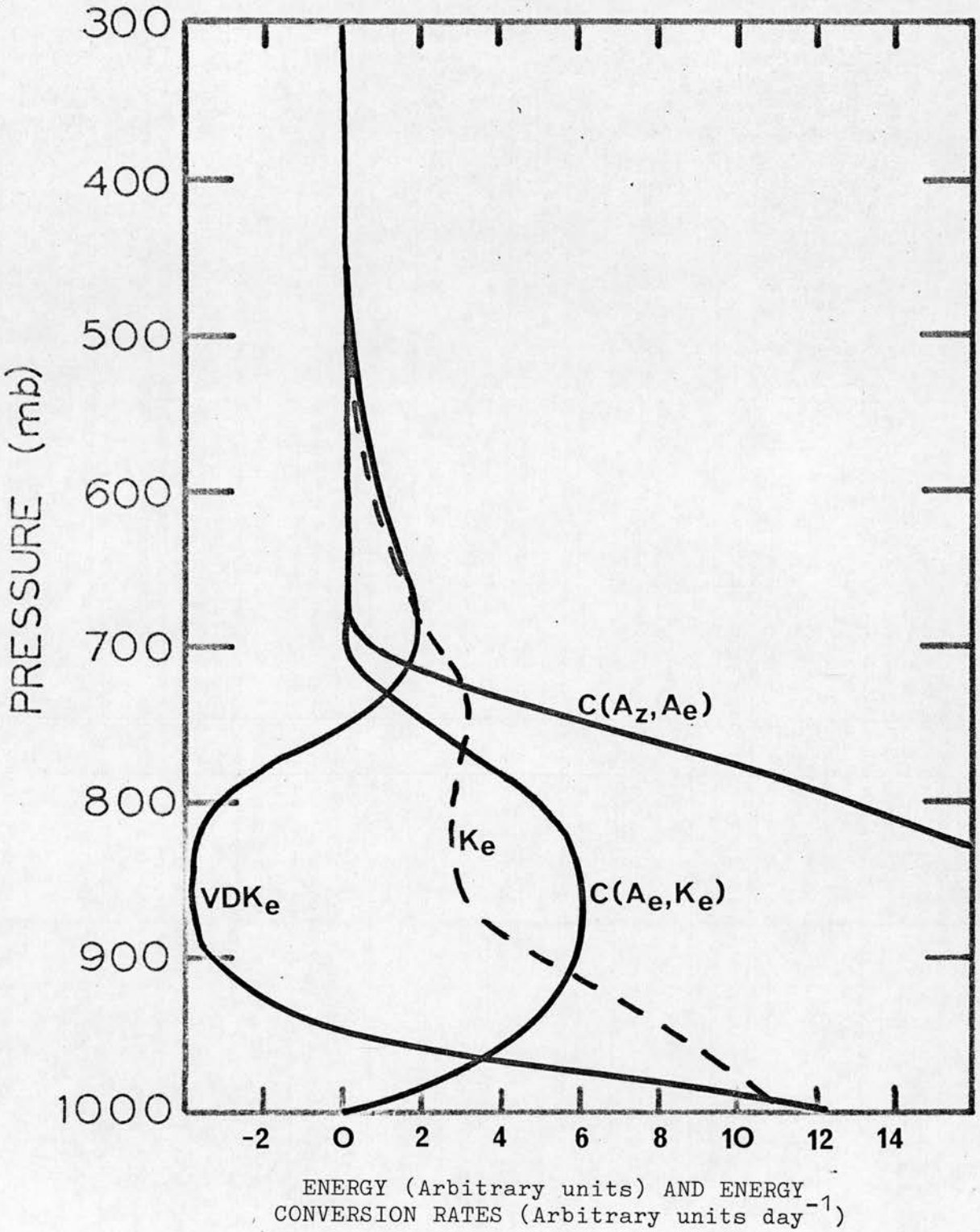

Figure 6.11 7th December 1967; horizontally averaged energy and energy conversion rates for 900 Km wave with $\sigma = 0.006$ m^2 s^{-2} mb^{-2} at 900 mb.

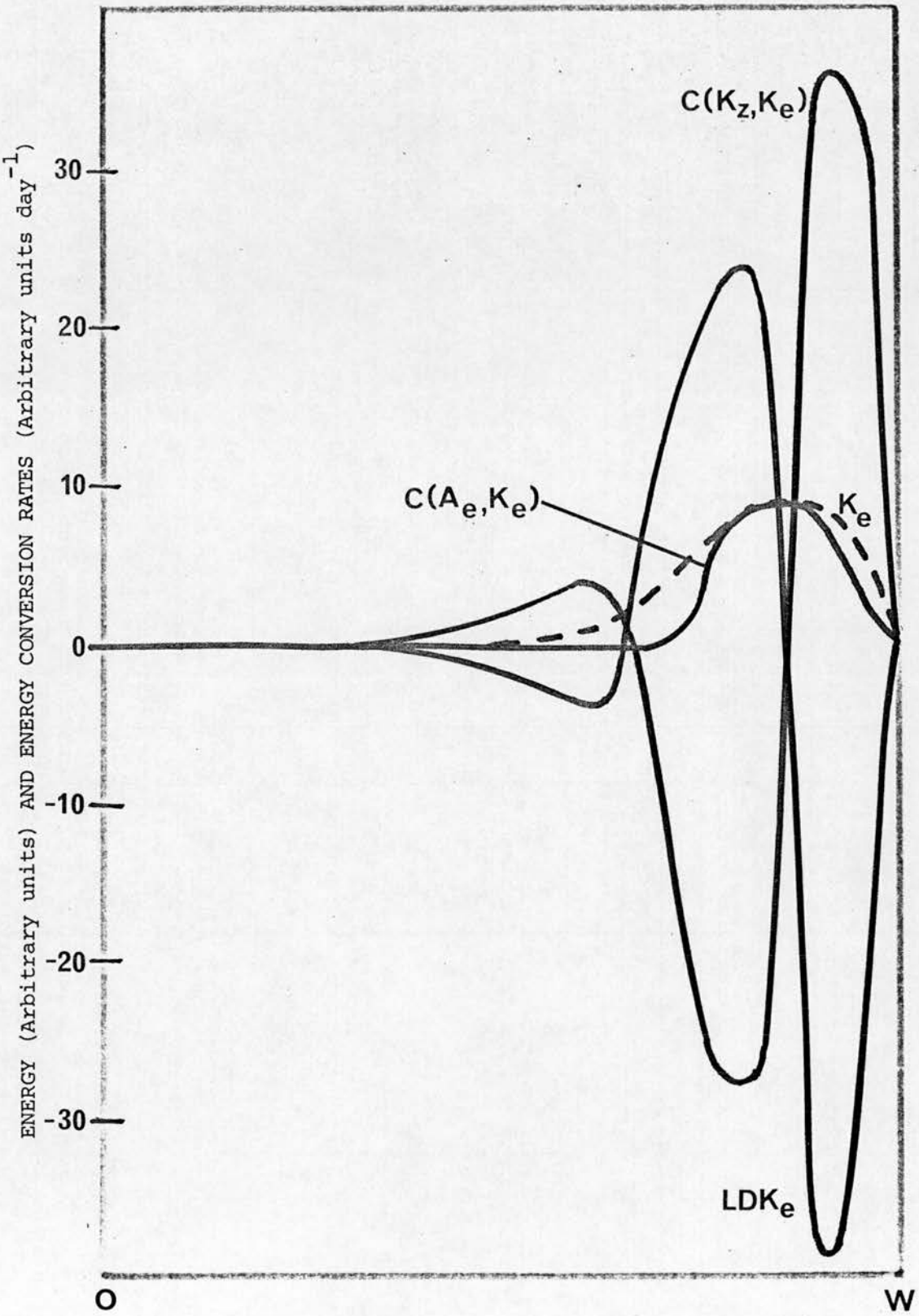

Figure 6.12 7th December 1967; vertically averaged energy and energy conversion rates for the 900 Km wave with σ=0.006 m^2 s^{-2} mb^{-2} at 900 mb.

a wavelength of maximum instability of 600 Km; in the latter no convergence was obtained with the numerical model, presumably because the growth rate of each mode was similar.

These results indicate the importance, for forecasting purposes, of a knowledge of the horizontal distribution of static stability in the lowest 300 mb of the atmosphere.

6.4 2nd January 1965

As in the last section the static stability at 900 mb is important in determining the wavelength of maximum instability. In figure 6.13 are shown the growth rates as a function of wavelength for $\sigma=0.002\ m^2\ s^{-2}\ mb^{-2}$ and $\sigma=0.005\ m^2\ s^{-2}\ mb^{-2}$ at 900 mb. Also shown are real and imaginary wave speeds for the latter example. At 900 mb these static stabilities are approximately equivalent to an increase in potential temperature of $0.8^{\circ}C$ and $1.7^{\circ}C$, respectively, over 100 mb.

Only the situation appropriate to $\sigma=0.005\ m^2\ s^{-2}\ mb^{-2}$ is discussed in detail since a discernible wavelength of maximum instability exists in this case. The relative streamfunction amplitude for the 600 Km wave is shown at various levels in figure 6.14; it may be seen that the unstable wave is very shallow and develops in the area on the western side of the channel, where the vertical wind shear is largest. Relative streamfunction and vertical velocity phase lags, figure 6.15, illustrate that the backward tilt of the trough exists only to 850 mb. At grid points east of the perturbation maximum the lag between trough and vertical

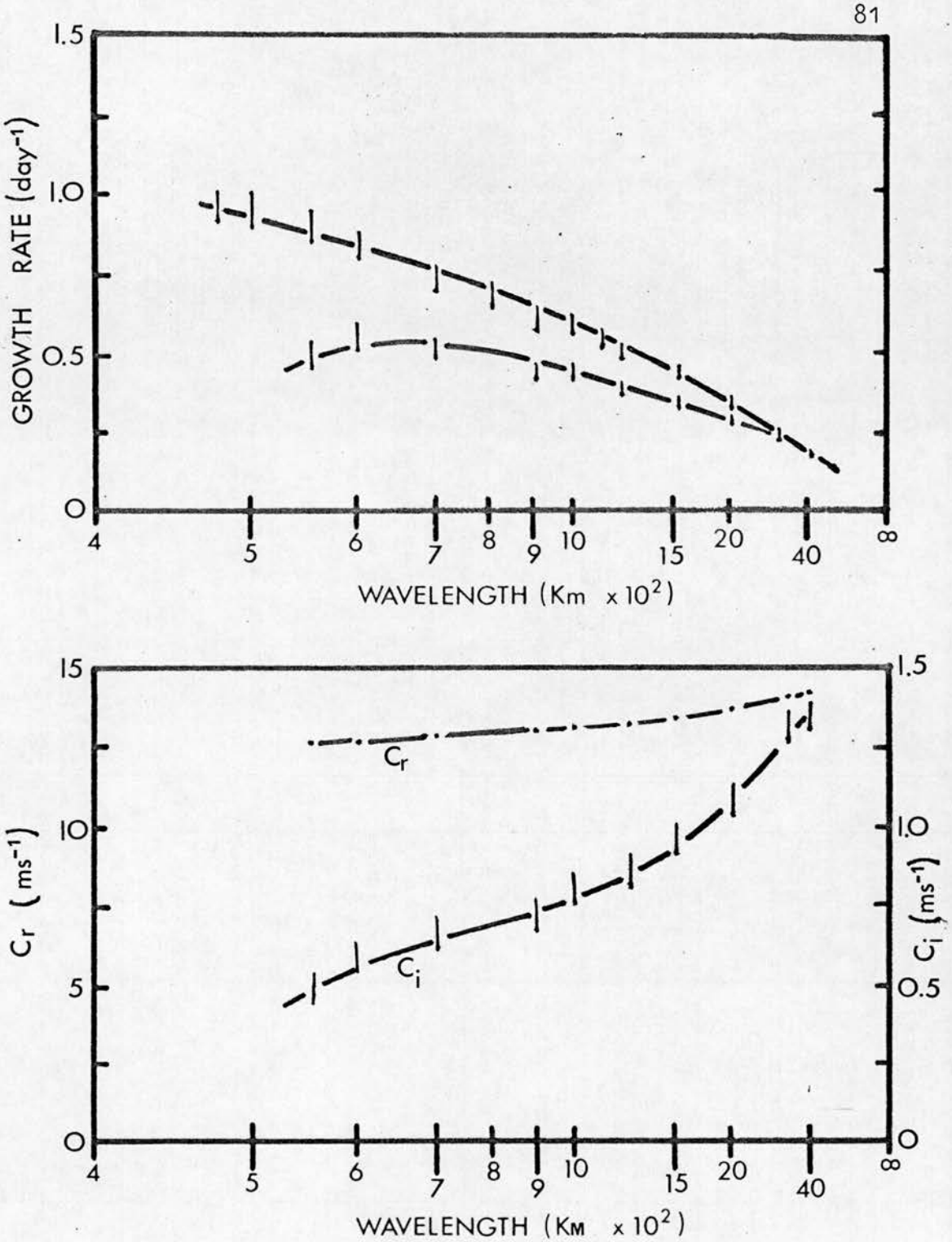

Figure 6.13 2nd January 1965.

Above: Growth rate obtained with $\sigma = 0.002$ m^2 s^{-2} mb^{-2} at 900 mb (upper curve) and with $\sigma = 0.005$ m^2 s^{-2} mb^{-2} at 900 mb (lower curve).

Below: Real and imaginary wave speeds corresponding to lower growth rate curve.

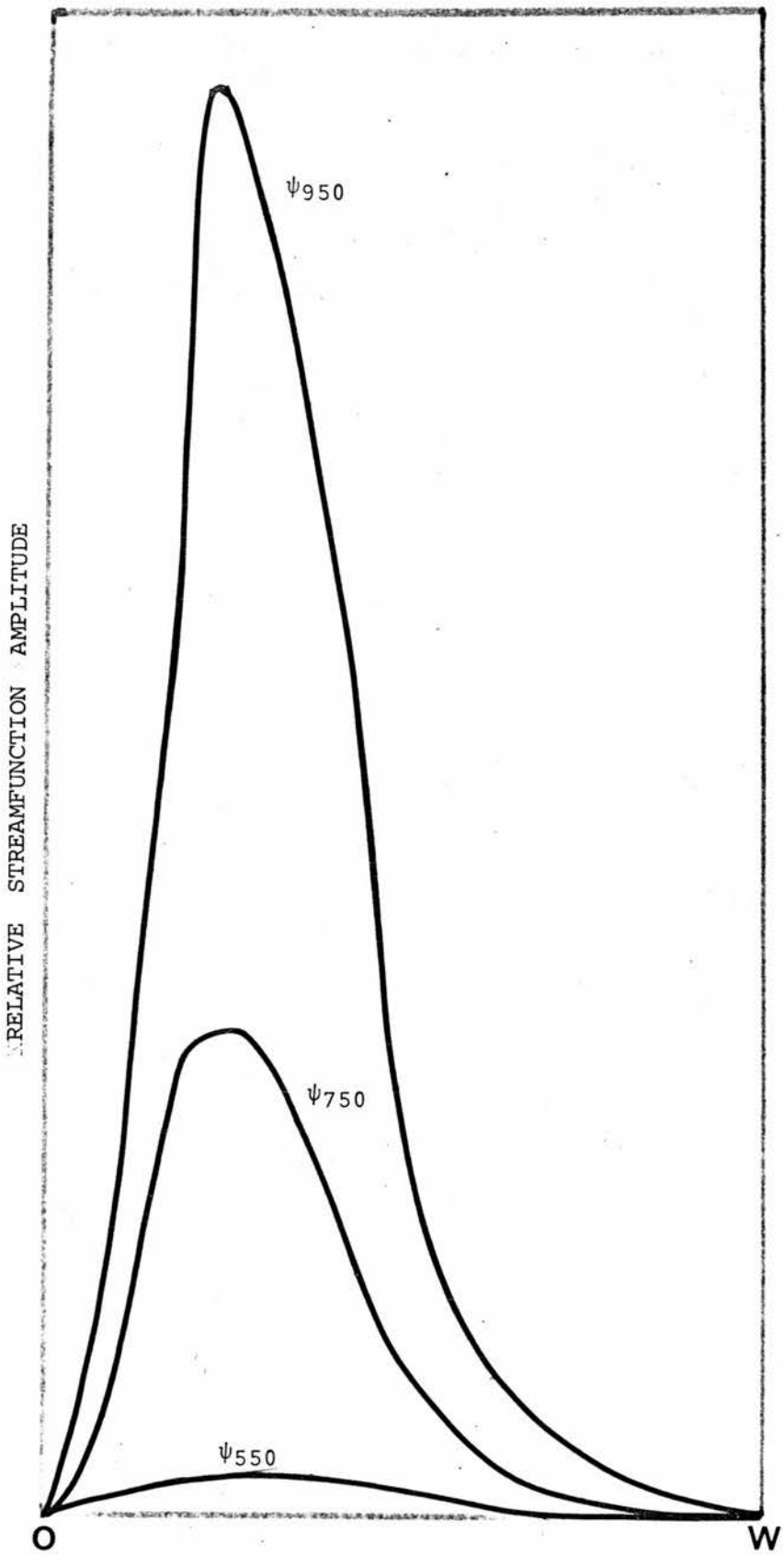

Figure 6.14 2nd January 1965; relative streamfunction amplitude at 950, 750 and 550 mb for 600 Km wave with σ=0.005 m^2 s^{-2} mb^{-2} at 900 mb.

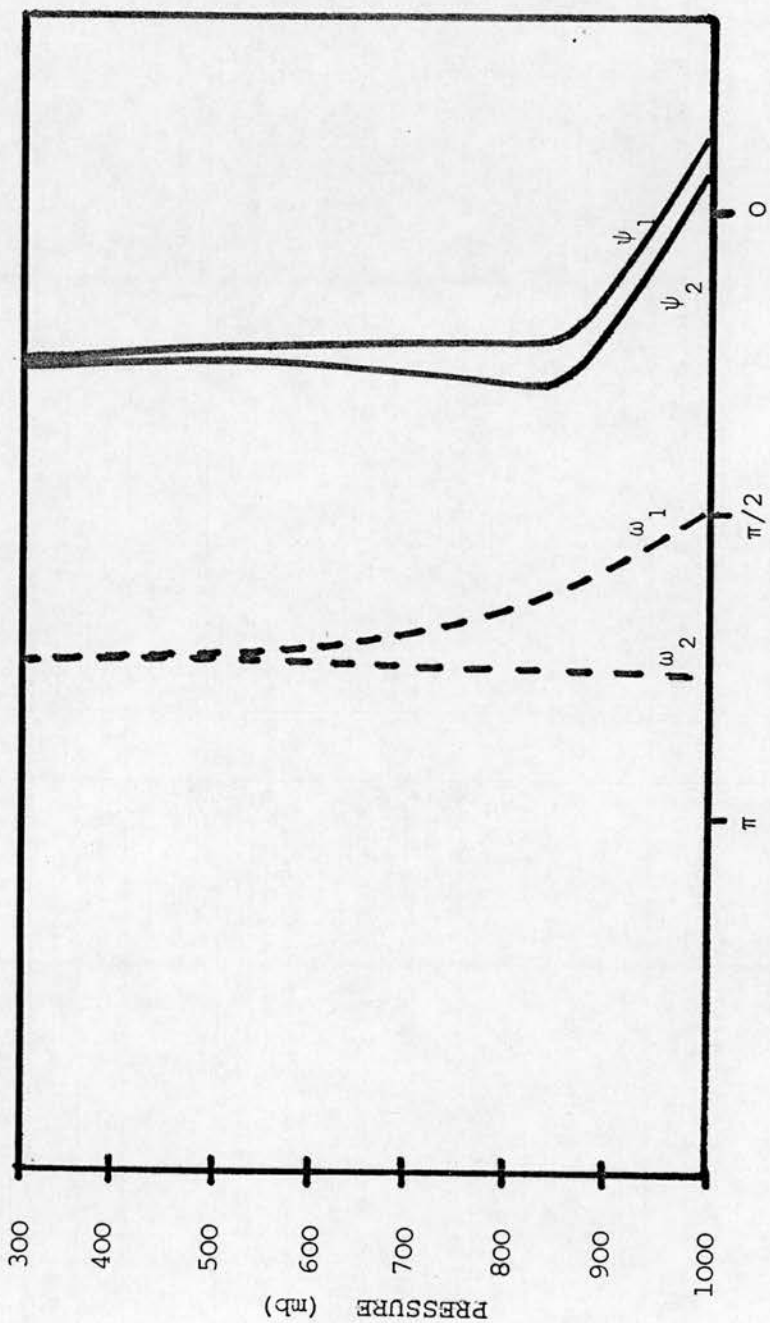

Figure 6.15 2nd January 1965; relative streamfunction and vertical velocity phases at two grid lengths (subscript 1) and one grid length (subscript 2) from the western channel wall, for the 600 Km wave with σ=0.005 $m^2 s^{-2} mb^{-2}$ at 900 mb.

velocity maximum departs from the optimum value of $\pi/2$, thus decreasing the efficiency of the conversion of available potential energy to kinetic energy.

The very shallow nature of the wave is emphasised when horizontally averaged energy conversion rates are considered. In figure 6.16 it can be seen that the eddy kinetic energy receives a positive contribution from available potential energy only below 800 mb and that vertical motions increase the eddy kinetic energy above 800 mb and also close to 1000 mb. A small part of the eddy kinetic energy is lost to zonal kinetic energy in the 600 Km wave although at longer wavelengths (>900 Km) the eddy kinetic energy is increased by conversion of zonal kinetic energy.

Vertically averaged energy conversion rates, figure 6.17, indicate that lateral divergence of kinetic energy almost counteracts the conversion of zonal to eddy kinetic energy. While the net effect is to decrease the rate of growth of kinetic energy at the centre of the perturbation an increase in the rate of growth is observed away from the centre. The disturbance can be seen to develop almost entirely in the western side of the channel.

In the case where $\sigma = 0.002\ m^2\ s^{-2}\ mb^{-2}$ the short waves are very similar to the 600 Km wave described above. Due to the lower static stability at 900 mb, however, the growth of eddy kinetic energy through the baroclinic process is greater and hence the growth rate is larger.

The shallow, model disturbance appears to adequately

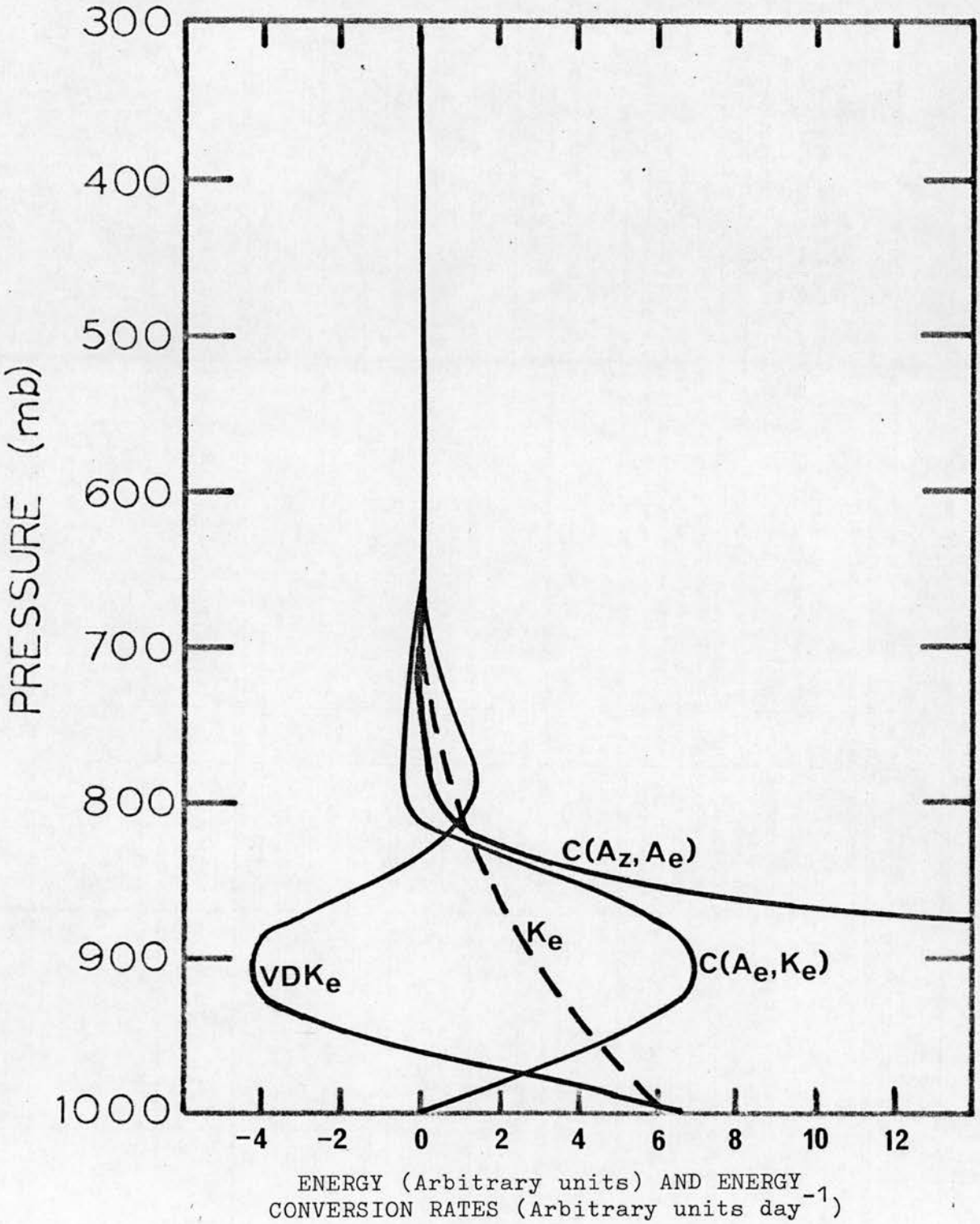

Figure 6.16 2nd January 1965; horizontally averaged energy and energy conversion rates for the 600 Km wave with σ=0.005 m^2 s^{-2} mb^{-2} at 900 mb.

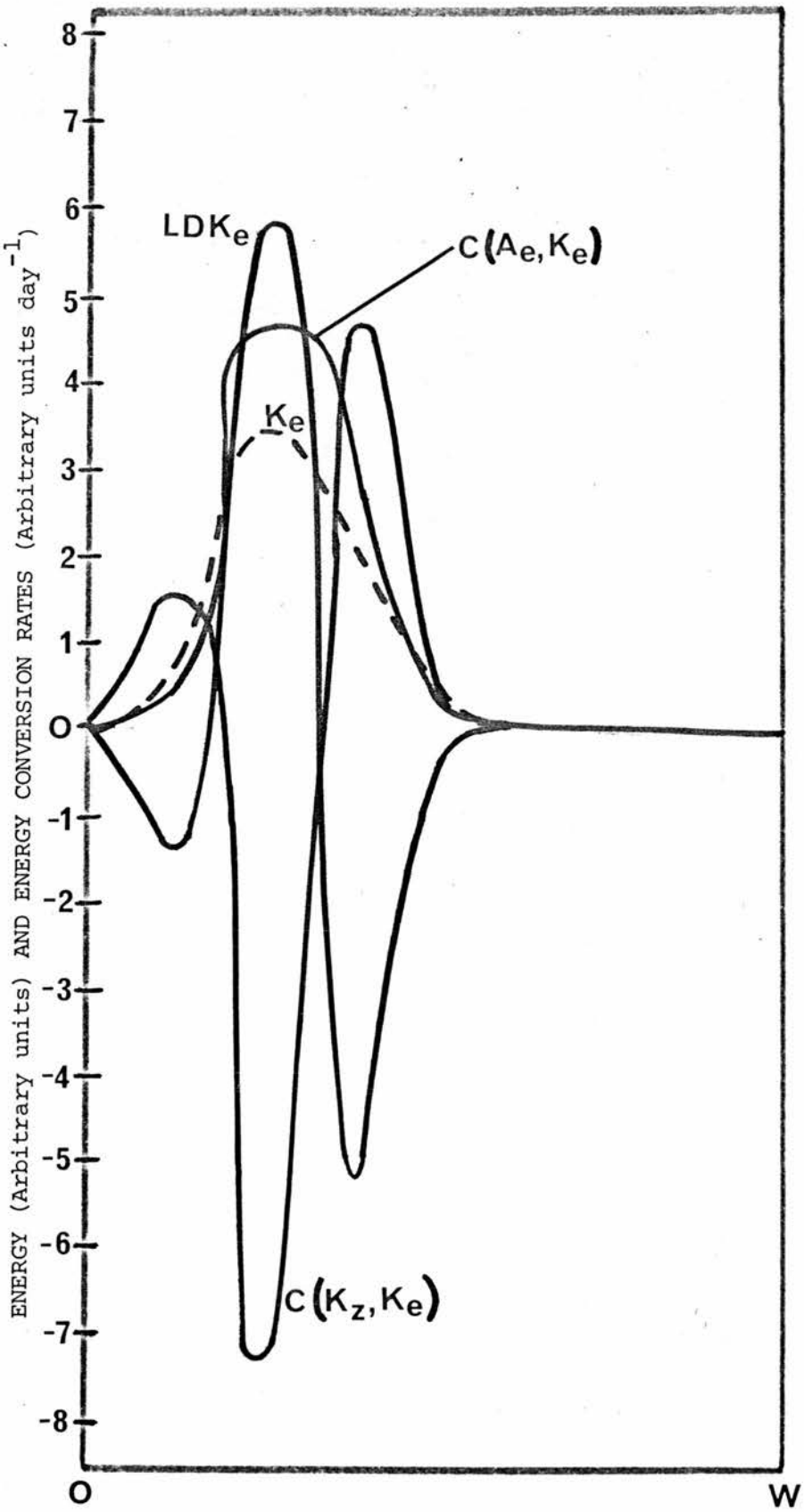

Figure 6.17 2nd January 1965; vertically averaged energy and energy conversion rates for 600 Km wave with σ=0.005 m^2 s^{-2} mb^{-2} at 900 mb.

resemble the polar low of 2nd January 1965. The observed wavelength was 800 $\pm$ 200 Km and the phase speed was 12 $\pm$ 1.5 ms^{-1}. Between 1000 Km and 600 Km the model phase speeds varied from 13 ms^{-1} to 12 ms^{-1}.

CHAPTER 7

CONCLUSIONS

An inspection of surface charts from January 1963 to December 1972 revealed that northerly outbreaks, defined as flow over the N.E. Atlantic, from a direction between north-west and north-east, persisting for more than 48 hours, were much more frequent than polar lows, defined as depressions developing in the northerly flow. Care was taken to exclude secondary depressions from those considered. During this ten-year period 133 northerly outbreaks were recorded and 57 polar lows developed. More than half (32) of the polar lows developed in October, November or December, when the air-sea temperature difference would be large, which suggests that low level instability is important.

Although in most cases the surface air was colder to the east of the polar lows than to the west, about one third of the cases exhibited temperatures increasing from west to east. This suggests that polar lows may develop in situations where the thermal wind is in the opposite direction to the mean flow, as well as the more common situation where wind speed increases with height. The assumption is made that the surface temperature gradient is representative of the temperature gradient in the lower part of the atmosphere, where polar lows develop.

To predict the expected wavelength and phase speed of polar lows it seems suitable to use solutions to the Eady problem; the corresponding growth rates can, however, be

considered as an upper limit to the likely instability. The wavelength of maximum instability depends very much upon static stability, varying from 930 Km (σ=0.01 m^2 s^{-2} mb^{-2}) to 415 Km (σ=0.002 m^2 s^{-2} mb^{-2}) for a disturbance of 300 mb depth at latitude 60°N.

Wind shear is never as simple as in the Eady case and horizontal wind shears were found not to contribute to the growth of eddy kinetic energy in the cases investigated. Large velocities at high levels facilitate development by increasing the vertical wind shear at low levels; regions of such shear appear to be preferred for polar low development.

This study has neglected surface friction; its effect on baroclinic waves has previously been found to be a reduction in instability and phase speed and a shift of the wavelength of maximum instability towards longer wavelengths. Surface heating has also not been considered explicitly as a turbulent eddy transfer process, although it is included implicitly by the assumption of low static stabilities near the surface. The most important shortcoming of the model employed is the use of a static stability which is averaged over constant pressure surfaces rather than one which is allowed to vary horizontally. On 7th December 1967 this seems to have been important since, in the region where the disturbance developed in the model, observed static stability was larger than that used in the model.

When the lapse rate near the earth's surface is close to the dry adiabatic lapse rate, as occurs when polar or

arctic air moves southwards over the N.E. Atlantic Ocean, very short wavelength disturbances are unstable. Although this study has treated each wavelength separately, neglecting interactions between waves of different scales, a spectrum of wavelengths exists in the atmosphere. The kinetic energy associated with each wave decreases towards the short wave end of the spectrum. On the synoptic scale, therefore, it is likely that the very short-wavelength, unstable disturbances are not as readily observed as the longer waves, which are also unstable, because the energy associated with the short waves is smaller. It would, however, be necessary to use a high resolution, non-linear model to investigate this.

APPENDIX

Energy Conversion Equations

If the vorticity equation, 2.6, is multiplied by ψ an equation describing the rate of change of eddy kinetic energy results:

$$\frac{1}{2}\frac{\partial}{\partial t}(\nabla\psi\cdot\nabla\psi) = \nabla\cdot\psi\nabla\frac{\partial\psi}{\partial t} + U\psi\frac{\partial^3\psi}{\partial x^3} + U\psi\frac{\partial^3\psi}{\partial x\partial y^2} - \frac{\partial^2 U}{\partial y^2}\frac{\partial\psi}{\partial x}\psi -$$

$$f\frac{\partial\psi\omega}{\partial p} + f\omega\frac{\partial\psi}{\partial p}.$$

After integrating this equation w.r.t. x it becomes

$$\int_0^{2\pi}\frac{1}{2}\frac{\partial}{\partial t}(\nabla\psi\cdot\nabla\psi)\,dx = \int_0^{2\pi}\frac{\partial}{\partial y}\left(\psi\frac{\partial}{\partial y}\frac{\partial\psi}{\partial t}\right)dx - \int_0^{2\pi} f\frac{\partial\psi\omega}{\partial p}\,dx +$$

$$\int_0^{2\pi} f\omega\frac{\partial\psi}{\partial p}\,dx - \int_0^{2\pi} U\frac{\partial}{\partial y}\left(\frac{\partial\psi}{\partial x}\frac{\partial\psi}{\partial y}\right)dx$$

where the terms are

$$\frac{\partial K_e}{\partial t} = LDK_e + VDK_e + C(A_e,K_e) + C(K_z,K_e)$$

and; LDK_e is the lateral divergence of eddy kinetic energy; VDK_e, the vertical divergence of eddy kinetic energy; $C(A_e,K_e)$, the conversion of eddy available potential to eddy kinetic energy; and $C(K_z,K_e)$, the conversion of zonal kinetic to eddy kinetic energy.

Similarly an equation for the rate of change of eddy available potential energy is obtained by multiplying the

thermodynamic equation, 2.7, by $\frac{f^2}{\sigma}\frac{\partial\psi}{\partial p}$;

$$\frac{f^2}{\sigma}\frac{\partial\psi}{\partial p}\frac{\partial}{\partial t}\frac{\partial\psi}{\partial p} + \frac{Uf^2}{\sigma}\frac{\partial\psi}{\partial p}\frac{\partial}{\partial x}\frac{\partial\psi}{\partial p} - \frac{\partial U}{\partial p}\frac{f^2}{\sigma}\frac{\partial\psi}{\partial p}\frac{\partial\psi}{\partial x} + f\omega\frac{\partial\psi}{\partial p} = 0.$$

Integration then leads to

$$\int_0^{2\pi}\frac{f^2}{2\sigma}\frac{\partial}{\partial t}\left(\frac{\partial\psi}{\partial p}\right)^2 dx = \int_0^{2\pi}\frac{\partial U}{\partial p}\frac{f^2}{\sigma}\frac{\partial\psi}{\partial p}\frac{\partial\psi}{\partial x}\,dx - \int_0^{2\pi} f\omega\frac{\partial\psi}{\partial p}\,dx$$

$$\frac{\partial A_e}{\partial t} = C(A_z,A_e) - C(A_e,K_e)$$

where $C(A_z,A_e)$ is the rate of energy conversion from zonal available potential energy to eddy available potential energy.

These terms, along with others for the eddy kinetic energy, K_e, eddy available potential energy, A_e, streamfunction amplitude and phase lag and vertical velocity amplitude and phase lag, were obtained at every grid point when the convergence criterion, ε, had been satisfied. Although, for any given solution, these results are useful some form of normalization is necessary if different solutions are to be compared. The normalization used here ensured that the total eddy kinetic energy of a wave was proportional to the total zonal kinetic energy. The constant of proportionality employed was expressed in arbitrary units which were consistent throughout the study.

Energy of the mean flow is referred to as 'zonal'; although not strictly correct this convention has been maintained since no fixed axis orientation has been imposed.

Comparison of Model and Analytical Solutions

In any numerical model difficulties arise due to truncation errors; the errors encountered because of the inadequacy of representing a continuous medium by a finite system. To investigate these errors in the model employed in this study a comparison was made between analytical (Eady) solutions and model solutions for a shallow baroclinic wave. The resolution of the model was initially Δy=200 Km, Δp=50 mb, channel width=1600 Km, but the grid lengths were halved in later experiments. Rigid lid upper and lower boundaries were imposed at 1000 mb and 700 mb. The other model parameters were $f=1.26 \times 10^{-4}\ s^{-1}$, $\sigma=0.01\ m^2\ mb^{-2}\ s^{-2}$ and vertical wind shear = $0.04\ m\ s^{-1}\ mb^{-1}$. Table A1 shows the growth rates obtained in these experiments. The phase speed obtained was always the same as the analytical phase speed, within the convergence limits of the model. It can be seen that the largest growth rate error obtained is 8% and that at short wavelengths this error is only about 3%. Improved vertical resolution increases the accuracy slightly, but improved horizontal resolution has little effect.

Table A1 Comparison of the growth rate (day^{-1}) obtained for Eady solutions and model solutions

Wavelength (Km)	Eady	Numerical Model		
		Δy=200 Km Δp= 50 mb	Δy=200 Km Δp= 25 mb	Δy=100 Km Δp= 25 mb
4000	0.448	0.42±0.01	0.45±0.01	0.45±0.01
2000	0.844	0.81±0.02	0.84±0.02	0.84±0.02
1500	1.057	1.01±0.02	1.05±0.02	1.05±0.02
1300	1.157	1.13±0.02	1.17±0.02	1.13±0.02
1200	1.208	1.18±0.02	1.18±0.02	1.22±0.02
1100	1.254	1.23±0.02	1.23±0.02	1.23±0.02
1000	1.287	1.25±0.03	1.30±0.03	1.30±0.03
900	1.285	1.27±0.03	1.27±0.03	1.27±0.03
800	1.208	1.22±0.03	1.22±0.03	1.22±0.03

LIST OF FIGURES

page

Figure

page

Figure

REFERENCES

Ames, W.F. 1969 "Numerical Methods for Partial Differential Equations", Nelson, pp 291.

Brown, J.A. 1968 "A Numerical Investigation of Hydrodynamic Instability and Energy Conversions in the Quasi-Geostrophic Atmosphere", Ph.D. Thesis, University of Colorado.

Brown, J.A. 1969 "A Numerical Investigation of Hydrodynamic Instability and Energy Conversions in the Quasi-Geostrophic Atmosphere", Parts I and II, Journal of the Atmospheric Sciences, 26, pp 352-375.

Dixon, R., Spackman, E.A., Jones, I. and Francis, A. 1972 "The Global Analysis of Meteorological Data using Orthogonal Polynomial Base Functions", Journal of the Atmospheric Sciences, 29, pp 609-622.

Eady, E.T. 1949 "Long Waves and Cyclone Waves", Tellus, 1, pp 33-52.

Haltiner, G.J. 1963 "Finite Difference Approximations for the Determination of Dynamic Instability", Tellus, 15, pp 230-240.

Haltiner, G.J. 1971 "Numerical Weather Prediction", John Wiley and Sons, pp 317.

Harley, D.G. 1960 "Frontal Contour Analysis of a "Polar" Low", Meteorological Magazine, 89, pp 146-147.

Harrold, T.W. and Browning, K.A. 1969 "The Polar Low as a Baroclinic Disturbance", Quarterly Journal of the Royal Meteorological Society, 95, pp 710-723.

H.M.S.O.	1964	"Weather in Home Fleet Waters", Volume I - Northern Seas, Part 1, pp 265.
Lyall, I.T.	1972	"The Polar Low over Britain", Weather, 27, pp 378-390.
Mansfield, D.A.	1972	"The Development of Intermediate Scale Disturbances in Cold Air Outbreaks", Ph.D. Thesis, University of London.
Miller, J.M.	1968	"Heat Transfer and Polar Lows", M.Sc. Thesis, University of London.
Phillips, N.A.	1963	"Geostrophic Motion", Reviews of Geophysics, 1, pp 123-173.
Stevenson, C.M.	1968	"The Snowfalls of Early December 1967", Weather, 23, pp 156-161.

ACKNOWLEDGEMENTS

I wish to thank Dr. D.H. McIntosh for allowing me to pursue this research in his department and for his advice. I should also like to express my gratitude to Dr. A.S. Thom, Dr. K.J. Weston, Dr. R.W. Riddaway and my fellow post-graduate students for many helpful and stimulating discussions.

I should also like to thank my wife who, not only typed this thesis, but also encouraged me throughout this research.

Part of this work was carried out with the support of a N.E.R.C. studentship for which I am grateful.